Space Science and Engineering Center
University of Wisconsin–Madison

A GOES Pathfinder Products Sampler

Version 1.0

A REPORT from the

COOPERATIVE INSTITUTE FOR METEOROLOGICAL SATELLITE STUDIES

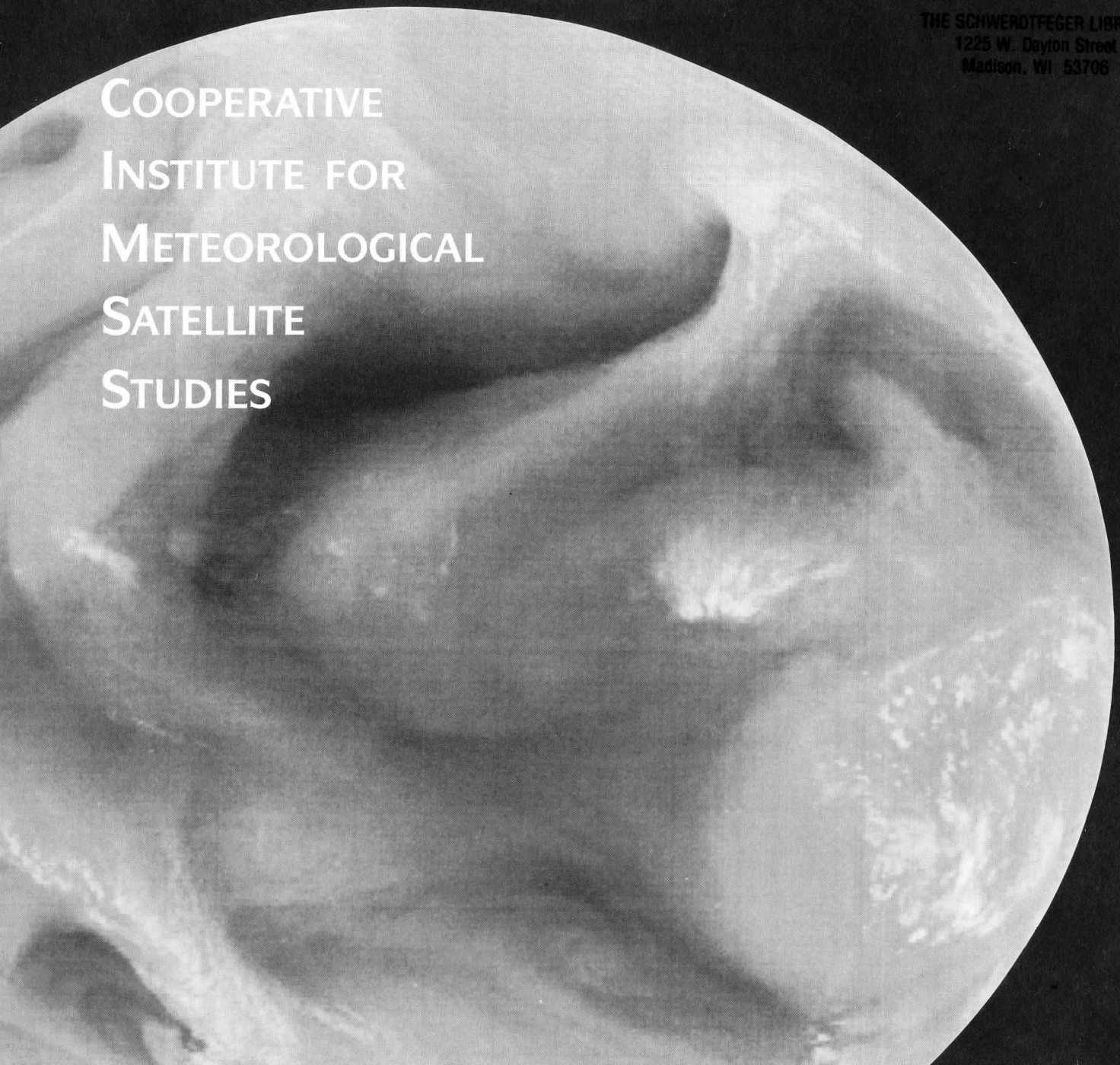

3-6-92

A GOES Pathfinder Products Sampler

Version 1.0

Contributions by:

Brian Auvine, SSEC
Francis Bretherton, SSEC
Cynthia L. Combs, CIRA
Christopher M. Hayden, NOAA/NESDIS/SDAB
Stanley Q. Kidder, U of A - Huntsville
W. Paul Menzel, NOAA/NESDIS/ASPP
Robert T. Merrill, CIMSS
Elaine M. Prins, CIMSS
Donald L. Reinke, CIRA
Anthony J. Schreiner, CIMSS
Brian Soden, SSEC
Thomas H. Vonder Haar, CSU
Gary Wade, NOAA/NESDIS/SDAB
Donald P. Wylie, SSEC

Edited by:

Timothy J. Schmit, CIMSS

March 1, 1992

CIMSS -- Cooperative Institute for Meteorological Satellite Studies
CIRA -- Cooperative Institute for Research in the Atmosphere
CSU -- Colorado State University
NOAA/NESDIS/ASPP -- NOAA/NESDIS Advanced Satellite Products Project
NOAA/NESDIS/SDAB -- NOAA/NESDIS Systems Design and Applications Branch
SSEC -- Space Science and Engineering Center
U of A - Huntsville -- University of Alabama - Huntsville

CONTENTS

This work has been funded under NOAA contract #50DDNE-1-0036.

ILLUSTRATIONS

1. Introduction -- The GOES Pathfinder: A Product Sampler

Francis Bretherton, SSEC
Brian Auvine, SSEC

Though data from the operational weather satellites have found extensive application in daily forecasting and in case studies of individual weather events, their use in analyses of climate has been much less frequent. Contributing to this imbalance have been the costs and difficulty of access to the archive. The GOES Pathfinder is funded jointly by NASA and NOAA in order to:

- Access GOES archive for climate and global change applications
- Prepare validated products
- Build science user - data center interface
- Prototype data and information management for a large data set

Purpose of the Product Sampler

This notebook has been prepared for the GOES Pathfinder Program by the Space Science and Engineering Center, University of Wisconsin - Madison (SSEC) as an open ended, working document. It is intended to describe a product sampler to introduce a broader range of scientists concerned with climate and climate change to some potential uses of data from geostationary satellites, and to stimulate discussion of the merits and shortcomings of individual approaches.

The product sampler consists of a brief description, key references and an illustration for each of a number of candidate products under consideration by the GOES Pathfinder Science Working Group to be prepared more extensively from the GOES archive. Constraints of resources and time dictate that this summary is primarily from the University of Wisconsin - Madison perspective. More potential products developed elsewhere should be included in later editions. An example already included is the cloud composite product developed at CIRA. As other products are added, it is anticipated that some of the present list may be given reduced priority. In the initial phases of the Pathfinder program, selectivity will be essential because of the high costs of accessing the entire data set, and the effort involved in processing the data to compact, reliable forms that address crucial scientific issues.

The proposed algorithms are in differing stages of readiness for large scale routine production. It is anticipated that prototype production on a limited set of these algorithms will begin in mid-1992 for the benchmark period of March 1987-November 1988, in association with preparing a summary 8 km, hourly, data set of the visible, infrared and water vapor channels. As resources permit, production will be extended thereafter both to the entire period of the archive and to a longer list of products. It must be emphasized that, even starting from the 8 km summary data, generation of even a single product through the entire period is likely to involve massive data processing. According to

present plans, facilities for that purpose will be available at SSEC but accessible over Internet. Principal Investigators will retain full responsibility for algorithms, quality control, and product validation.

GOES Data

The U.S. Geostationary Operational Environmental Satellites (GOES) have been operating continuously since 1976, and an almost complete archive exists since 1978. Throughout the day and night each satellite views a fixed sector of the Earth which is centered at the equator and may span roughly 120° longitude between 60° N and S. The primary instrument has been the Visible Infrared Spin Scan Radiometer (VISSR), which returns images with resolution at nadir of 1 km from reflected visible radiation in a band 0.5-0.8 micrometers, and with a nadir resolution of 7 km from emitted infrared radiation in the 11 micrometers window. Since 1980 the VISSR Atmospheric Sounder (VAS) has enabled addition measurements in 12 spectral bands in the infrared with approximately 14 km resolution. Over most of the period 1981 - 1989 two satellites were stationed above 75°W, and 135°W. Before and since that period, data are available from only one satellite, often at an intermediate longitude which varies with the season. Since the principal role of the satellite system has been to monitor the development of severe weather, priority was normally given to full disk half hourly visible and infrared images from VISSR, supplemented since 1981 by images from the 6.7 micrometer water vapor channel. Owing to competition for observing time, coverage of VAS soundings with the multispectral VAS was less complete, though a fairly continuous three hourly set was obtained for latitudes 30°N - 50°N since 1984.

The GOES archive is maintained at the Space Science and Engineering Center. It consists of 120 TBytes of digital data, on some 26,000 videotape cartridges, in a form closely related to the original telemetry from the satellite. Each cartridge holds approximately 8 hours of data from one satellite. Though individual scenes can readily be retrieved through McIDAS with a delay of a few hours (or days, depending on the physical location of the record), a new access system is needed to cope with the throughput required for climate studies. Simply recovering one years data involves a sustained transfer rate of 3 Mbytes/s, 24 hours a day 360 days a year. This substantially exceeds the capacity of an Ethernet, and rules out the possibility of random access to the archive. Instead, emphasis is being placed on the efficient and flexible generation of products, not to exceed 100 GBytes when applied to the entire 13 year period, which can be widely distributed or accessed from an on-line product store. Note that this operational definition focuses solely on a volume reduction of at least 1000:1. A well defined subset of the original data that meets this criterion is entirely acceptable as a product, even though no other transformation is initially applied. Proposals for such subsets for subsequent processing elsewhere are welcome. One example is the extension of the ISCCP B3 dataset back to 1978.

Following are summaries of several of the proposed products that might be generated from the archive. They currently include:

- Clouds products:
  - cirrus cloud detection using the CO_2 slicing technique
  - monitoring of diurnal cloud forcing
  - high resolution cloud composite climatology (CIRA)
- Upper level moisture
- Atmospheric motion
- Fires
- Atmospheric stability

2. Cirrus cloud detection by VAS CO_2 slicing technique

Donald P. Wylie, SSEC
W. Paul Menzel, NOAA/NESDIS

Objective

To reliably map semi-transparent cirrus, as well as other clouds, using the CO_2 slicing technique.

Introduction

GOES/VAS multispectral observations in the carbon dioxide absorption band at 15 micrometers have been used to compile cloud cover statistics over the continental United States for the four years from 1986 through 1989. The CO_2 technique calculates both cloud top pressures and effective emissivities and reliably distinguishes semi-transparent cirrus from opaque clouds. The frequency of semi-transparent cirrus clouds exhibit small seasonal variation; they are generally present 25 to 30% of the time in all seasons. Diurnal variations of semi-transparent cirrus are found only in the summer months and correspond to diurnal variations in convection in the Rocky mountains and southeastern United States; increases of 20% in cirrus are noted subsequent to the convective cloud activity. In the winter months, no diurnal change in semi-transparent cirrus is detected. Attempts to correlate cirrus with some common atmospheric features reveal that a majority of cirrus occurred where dynamic parameters indicate rising vertical motion, but that considerable cirrus were also found where dynamics were weak.

Method

See the attached reference for details about the CO_2 method as applied to VAS data.

Intercomparison with ground reports of cloud cover reveal that the satellite observations are corroborating or complementary 80% of the time; many of the disagreements come from the satellite identifying cold ground as low cloud or ground observations missing high thin clouds. Figure 2-1 shows the seasonal and geographical distribution of VAS observations of cloud cover from 1986 through 1989.

Status

Using the GOES/VAS archive, this analysis could be extended back to 1985 and forward from 1989, although only over the latitudinal coverage of the United States.

References

Menzel, W. P., D. P. Wylie, and K. I. Strabala, 1992: Seasonal and Diurnal Changes in Cirrus Clouds as seen in Four Years of Observations with the VAS. Jour. Appl. Meteor., Vol 31, No 4, 370-385.

Wylie, D. P. and W. P. Menzel, 1989: Two Years of Cloud Cover Statistics Using VAS. Jour. Clim., Vol. 2, No. 4, 380-392.

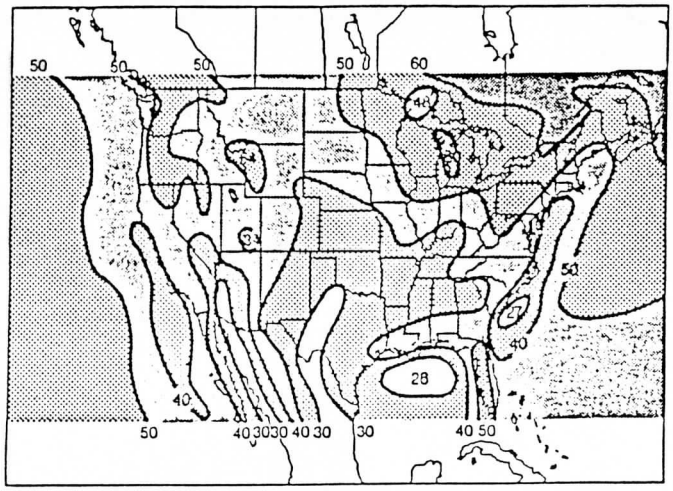

PROBABILITY OF OPAQUE CLOUD IN WINTER

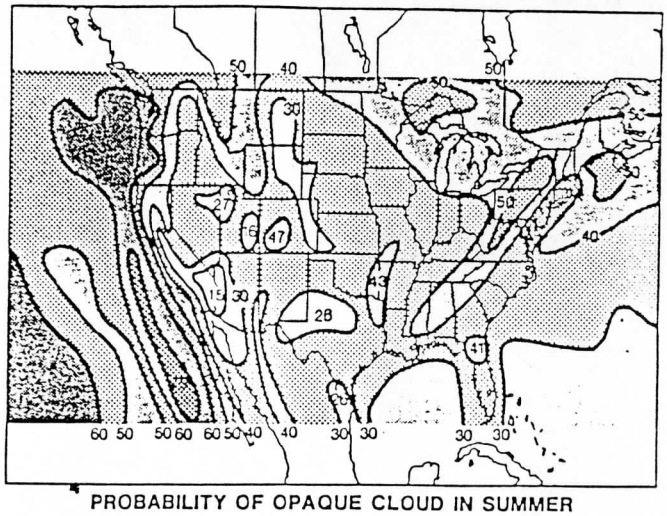

PROBABILITY OF OPAQUE CLOUD IN SUMMER

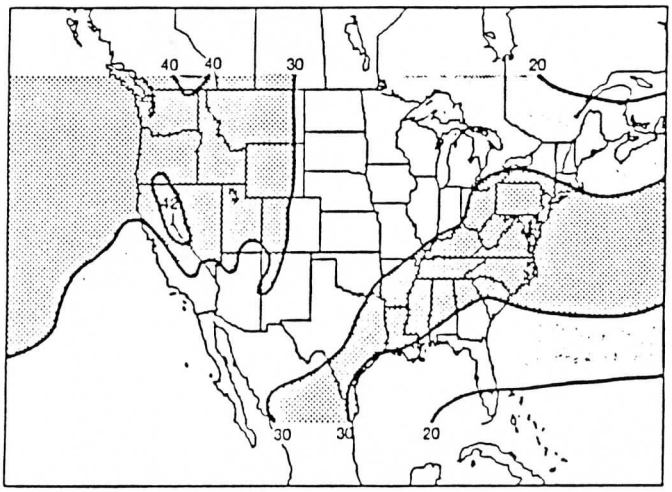

PROBABILITY OF CIRRUS IN WINTER

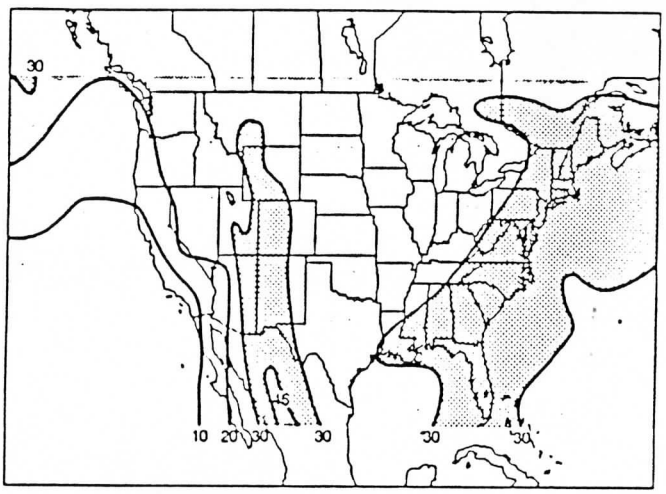

PROBABILITY OF CIRRUS IN SUMMER

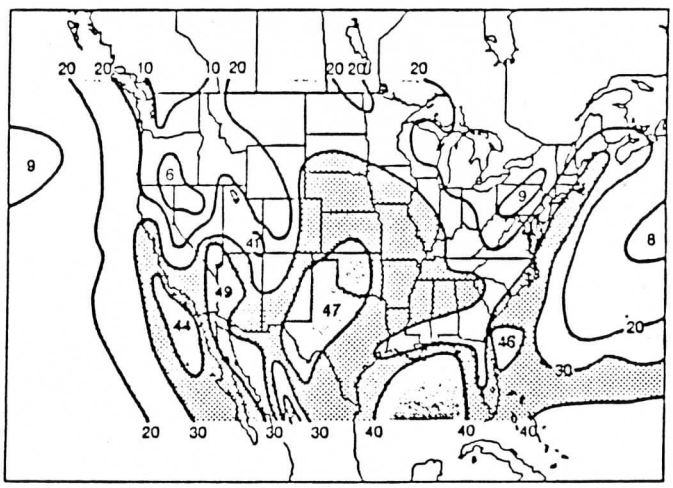

PROBABILITY OF CLEAR SKY IN WINTER

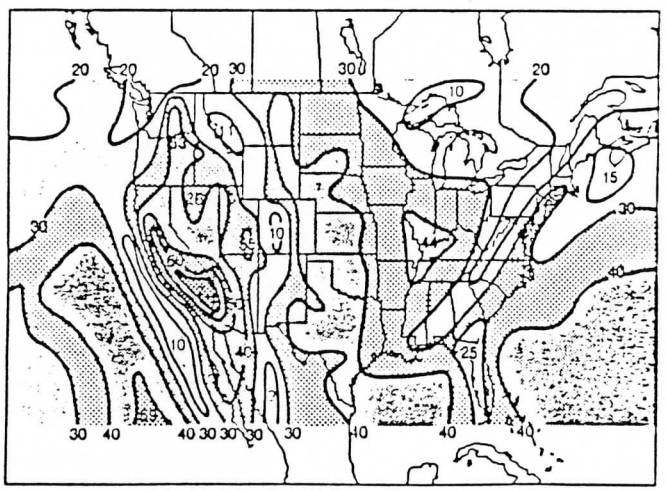

PROBABILITY OF CLEAR SKY IN SUMMER

Figure 2-1. The seasonal distribution of VAS observed cloud cover from the CO_2 slicing method from 1986 to 1989. The probability of opaque, cirrus and clear sky is shown. The panels on the left (right) show winter (summer) results.

3. Diurnal Cloud Forcing with Multispectral GOES Observations

Anthony J. Schreiner, CIMSS
Christopher M. Hayden, NOAA/NESDIS/SDAB

Objective

To investigate the relationship between observed sky conditions and outgoing radiation using the high temporal resolution VAS data.

Introduction

Relating the difference in radiance as skies change from clear to cloudy is a direct application of the VAS dwell sound information. The GOES is ideally suited to investigate the change in outgoing radiance as a function of changing sky conditions over periods ranging from several hours to days to seasons. An example is shown below in Table 1 and Figure 3-1.

Method

The clear and cloudy radiance differences are calculated from the operational cloud clearing algorithm described in Hayden (1988). Variation in cloud types and amounts during cloud formation and dissipation can be correlated with observed outgoing radiation in the VAS spectral bands. Radiances in the twelve infrared spectral bands ranging from 3.9 to 14.7 μm can be regressed to indicate the outgoing longwave flux (Herman and Smith, 1986). A long record of comparisons would reveal the relationships between cloud type and amount and outgoing infrared radiation.

Table 1. One day comparison of calculated clear, clear - observed scene (Cloud Forcing), and Observed Clouds for 27 May 1991 over Des Moines, IA. Radiances for clear and cloud forcing are in mW/ster/m^2/cm^{-1} for the 11 micrometer region.

TIME(UTC)	CLEAR	CLOUD FORCING	OBSERVED
01	105.2	0.0	Scattered at 25,000 ft.
04	100.2	0.0	Clear
07	96.9	4.7	Broken at 4,800 ft.
			Broken at 25,000 ft.
10	97.2	30.6	Scattered at 25,000 ft.
13	99.5	35.0	Scattered at 8,000 ft.
			Overcast at 25,000 ft.
16	106.2	31.8	Scattered at 10,000 ft.
			Broken at 25,000 ft.
18	116.8	0.3	Clear
21	116.6	0.0	Clear

Status

Currently, data for approximately forty surface observing stations covering the continental United States are being archived daily. Included in this data collection are the "clear" and the observed radiances for the 15 μm absorption band and the 11 μm band coincident in time and location for each observing site. The archive is almost continuous from September 1991 onward. Retrospective data back to 1981 could be processed from the archive. The VAS dwell sound radiances, an atmospheric temperature and moisture profile and surface data are needed to produce this product.

References

Hayden, C. M., 1988: GOES-VAS Temperature-Moisture Retrieval Algorithm. Jour. Appl. Meteor., **27**, 705-733.

Herman, L. D. and W. L. Smith, 1986: Intercomparison of preliminary earth radiation budget satellite (ERBS) flux estimates and geostationary satellite multispectral VAS radiance measurements. 6th Conference on Atmospheric Radiation, 13-16 May 1986, Williamsburg, VA, AMS, Boston, MA.

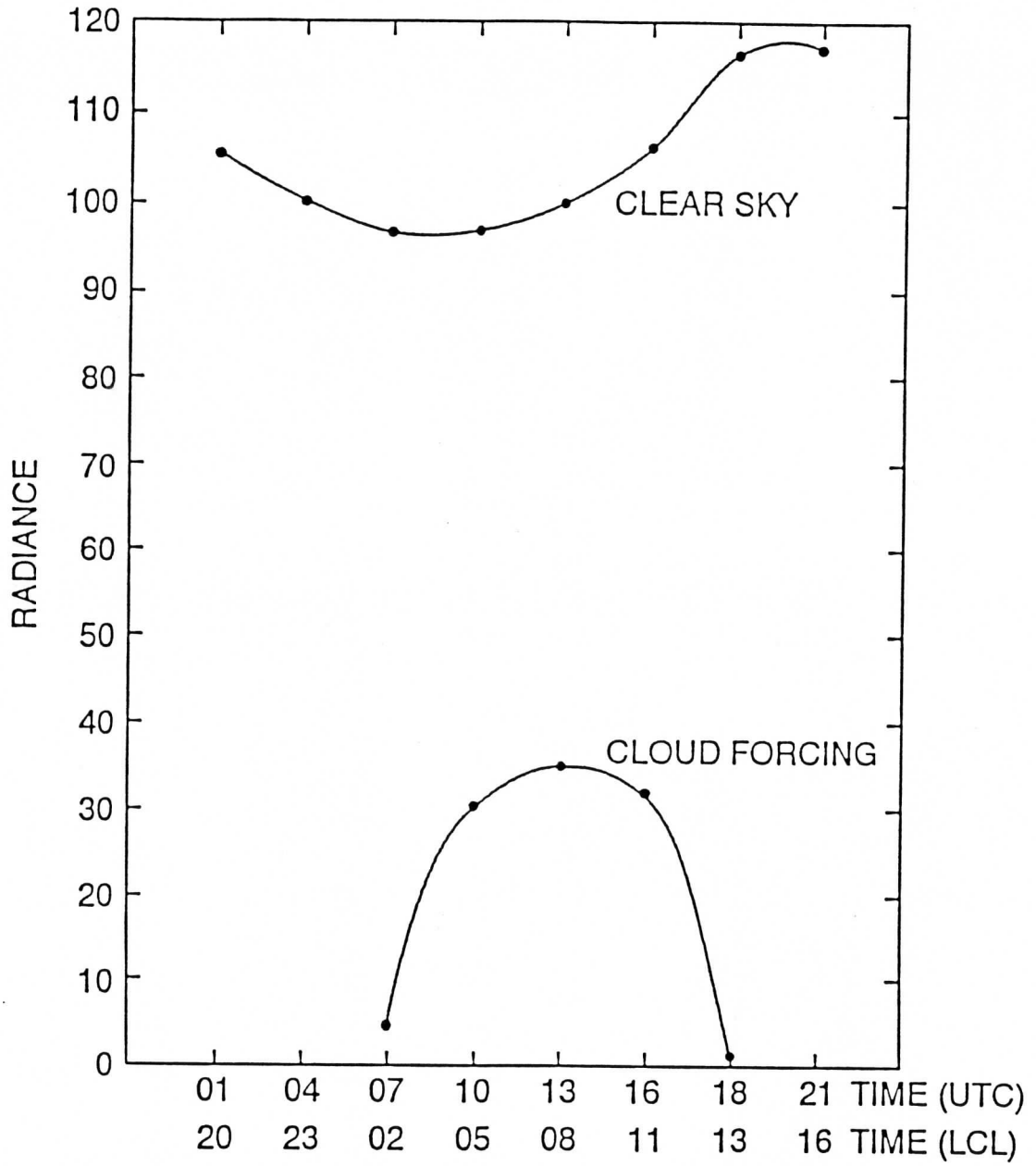

Figure 3-1. Comparison of Clear, Clear - Observed (Cloud Forcing), for 27 May 1991 over Des Moines, IA. Radiances for Clear and Cloud Forcing are in $mW/ster/m^2/cm^{-1}$ for the 11 micrometer region.

4. Satellite Cloud Composite Climatologies

Donald L. Reinke, CIRA
Cynthia L. Combs, CIRA
Stanley Q. Kidder, U of A - Huntsville
Thomas H. Vonder Haar, CSU

Objective

To produce an image of monthly cloud frequency using the processing procedure developed at Colorado State University\CIRA.

Introduction

GOES digital imagery has been collected and composited over portions of the U.S. since March, 1988. High spatial and temporal Resolution Satellite Cloud Composite Climatologies (HRSCCC's) have been produced which represent cloud frequency maps for each season. For each month studied, the cloud composite products represent the cloud occurrence frequency for each GOES pixel location and depict the overall spatial distribution of cloud cover over large portions of the United States.

The satellite composites present a new cloud climatology at a greater spatial and temporal resolution than previously available. Composites with ground resolutions of 2.5 km at hourly time intervals show patterns of cloud cover that are not detected in pre- existing cloud climatologies. The resolution of the proposed product is 8 km (figure 4-1) which can be compared to the high resolution image (2.5 km) in the referenced paper (figure 8).

Method

The starting point for the processing is acquisition of a series of GOES visible images for a given month, year, and time of day for a certain region. Then the images are remapped into a Mercator projection at the chosen resolution. The registration accuracy of these images must be manually checked and aligned, if needed.

Each pixel location in all images is compared to find the darkest pixel (should be land/water value at that location without clouds). A background image is generated for the given time range.

A composite image is generated for each pixel, by comparing each image value with the background value at that location plus additional threshold value (to account for sensor calibration errors-"banding"). An image value above background plus threshold is classified as cloud and added to the number of cloud days for that pixel. If the image value is below background plus threshold, its classified as clear.

The final HRSCCC image is the percentage of cloud for each pixel which is the number of cloud days divided by the total number of days.

Status

There are issues that need to be resolved. These include the presence of snow or shadow, parallax and alignment. Infrared data could also be processed.

Visible properties of snow are similar to cloud, which causes two possible problems. First, snow cover that stays for the entire month will appear on the background image. This may result in some missed clouds over the snow-covered area. A similar problem occurs for white sand or salt flats. Second, if the snowfall and/or melt occurs during the month, it will not appear on the background image. This will usually result in the snow being counted as cloud when it is actually clear. Yet, snow only affects a small region of each full disk image, and in most cases can be manually identified.

The shadows of clouds cast on land/water are darker, and will appear as unrepresentative values in the background image. These shadows can be dark enough for clear land in other images to be classified as cloud. There are two ways to account for the shadows. First, images with cloud shadows can be taken out of the background process, then used for the composite. Second, when shadows occur on most images (i.e. early winter mornings), sections of images with no shadows need to be manually identified, and combined into the background. Both of the above methods require human intervention.

Because of such factors as cloud height, location, and position of the satellite, the cloud can be displaced in an image from its actual location. This parallax, or cloud displacement, can be corrected via IR cloud height, however, some additional error is introduced.

Manual image alignment may be necessary at the pixel scale due to errors in navigation. The re-alignment is accomplished by "rubber-sheeting" or "warping" the image to fit a predetermined projection using special software.

Images of satellite cloud composites can also be generated from the infrared data. Some benefits include: a better identification of high thin cirrus, better identification of clouds over white sand and salt flats, classification of high, middle, and low clouds, and nighttime HRSCCC, that expands coverage to a full 24 hours. IR composites can be produced with approximately the same amount of effort as the visible.

Reference

Reinke D. L., C. L. Combs, S. Q. Kidder, T. H. Vonder Haar, 1992: Satellite Cloud Composite Climatologies: A New High-resolution Tool in Atmospheric Research and Forecasting. Accepted by Bull. Amer. Meteor. Soc.

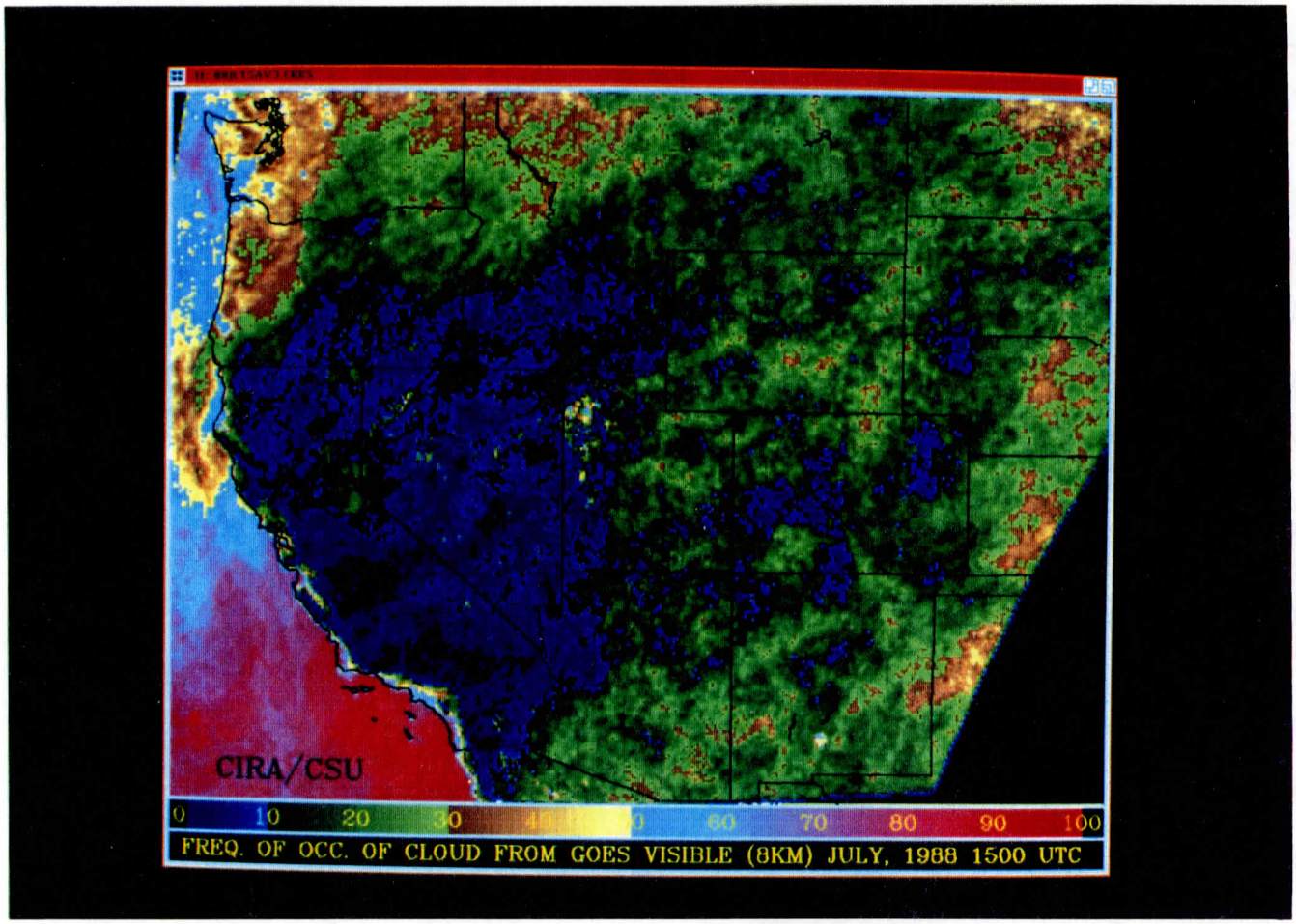

Figure 4.1 Frequency of cloud occurrence from GOES visible images (at 8 km resolution) at 15 UTC during July of 1988.

5. Upper Tropospheric Relative Humidity

Francis Bretherton, SSEC
Brian Soden, SSEC

Objective

To product a data set for evaluating GCM simulations of the distribution of water vapor in the upper troposphere.

Introduction

Water vapor is a critical variable for climate studies. It is poorly measured on a global scale, particularly over the oceans where there are few data and in the upper troposphere where radiosonde sensors are not reliable. On a synoptic basis small scale variability in relative humidity gives rise to severe sampling noise from the radiosonde network. Routinely available satellite retrievals of specific humidity are seriously impacted by uncertainties in the temperature, and systematic errors in the operational retrieval process largely negate the information for climatological purposes. The sensitivity of a global climate model (GCM) to enhanced concentrations of greenhouse gases such as carbon dioxide is very dependent upon the model treatment of water vapor. Because of the large dynamic range that must be accommodated, use of customary spectral methods to represent the quasi-horizontal transport of water vapor tends to yield negative concentrations in regions of low temperature. In addition, uncertainty in the parameterization of deep convective processes is reflected in the vertical transports; this uncertainty propagates into an error of the radiation to space, both directly and indirectly through its impact on the formation of clouds.

In spite of the existence of extensive archives, there have so far been few evaluations of GCM water vapor climatologies against information obtainable from satellite radiances. This appears to be because the data have not been easily accessible to GCM modelers. Filling this gap should be a high priority for the Pathfinder Program.

Some useful summary data sets have recently become available. Data from the microwave sensor SSM/I, currently operational on the sun synchronous satellites of the Defense Meteorological Satellite Program are being used by Wendt to provide estimates of the column integrated precipitable water over the ocean. These are being distributed by WetNet. Recently, Chesters and Neuendorffer have announced summaries of the radiance for the 6.7 μm channel on the NOAA TOVS instrument, also in sun synchronous orbit. However, there is still no readily available information on the diurnal cycle, nor has the effect of clouds on the infrared radiances been allowed for in a way that optimizes model comparisons.

Method

The present product is based solely on data from the large sensor (16 km resolution) 6.7 μm channel on the geostationary GOES satellites, with ancillary use of the 11 μm channel. Data from one or two satellites over the latitudes of the Americas are available in the archive almost every half hour since 1981. The 6.7 μm channel is sensitive primarily to the average relative humidity in a layer some 5 km deep in the upper troposphere, with a central pressure that increases with decreasing relative humidity. There are secondary dependencies on the viewing zenith angle, and on the mean temperature of the profile. Though middle and high cloud can contaminate this measurement, the high spatial resolution, multi-channel, information available in the satellite image permits the isolation of such contamination.

The processing and product format is deliberately tailored to comparisons with global climate models. Rather than attempting retrievals in the form of vertical soundings, attention is concentrated on the information actually present in the data stream, minimizing extraneous assumptions. It supposes the more complete variables available in the GCM will be used to perform the forward calculation necessary to estimate the radiance that should be seen by the satellite in the absence of cloud. Comparison with observation is then in terms of this radiance, or equivalently, brightness temperature. (See Hayden et al., 1992 for an example of high spatial resolution VAS simulations of the 6.7 μm channel over Texas). Efficient algorithms (Weinreb et al., 1981) developed from line by line calculations can be provided for doing the forward calculation, which provides the 6.7 μm channel brightness temperature as a function of vertical profiles of temperature and specific humidity, as well as of viewing zenith angle. Some simple, approximate, rules of thumb based upon sensitivity calculations with this algorithm are also provided to interpret the differences.

The observational data are summarized as cloud cleared average radiances (expressed as brightness temperatures) twice daily for all 1° squares within the full disk, with the cloud forcing (the difference between the actual and cloud cleared radiances) for each square available as a by-product. Several alternative methods for identifying significant cloud contamination and correcting for it are being carried on an experimental basis, and statistical analyses are being prepared of the differences and probable systematic and random error associated with each. These methods depend respectively on the difference between the 6.7 and 11 μm brightness temperatures, the spatial coherence in the 6.7 μm channel alone, and the spatial coherence in the 8 km resolution 11 μm channel coupled to a locally determined 6.7 - 11 μm regression. In the small fraction of squares in which no estimate can be obtained with confidence for the cloud cleared brightness temperature, a flag is set and values are interpolated from neighboring areas.

Calibrations

Sensor drift on satellites can occur in a number of ways. The most immediate is in the electronics surrounding the sensor and in the analogue to digital convertor, which are sensitive to variations in the

thermal environment within the satellite. These uncertainties are eliminated by frequently viewing both space and a blackbody of known temperature within the spacecraft, correcting the tables used to interpret the digital counts accordingly. Such operational calibrations have been applied in the present analysis. For the GOES VISSR/VAS instrument, additional corrections have to be applied if the temperature of the telescope optics and filter wheel varies. Except for a period 1985 - 1988 for GOES 6, when the servo-control on the filter wheel failed, drift associated with optics has not been detected. The effect of the filter wheel temperature excursions was relatively small for the 6.7 μm (band 10) and is correctable.

The absolute calibration of the 6.7 μm (band 10) sensor can not be precisely determined in-flight, but only the range bounded. The calibration is dependent on pre-launch measurements, the fidelity of measurements of space and the blackbody radiances, and the modelling of the radiation from the fore-optics components. Some estimate of absolute calibration is done pre-launch with data from the vacuum chamber. Menzel reports an absolute calibration of 0.38 mW/ster/m^2/cm^{-1} when viewing a 300 K target, with a relative error of 0.14 mW/ster/m^2/cm^{-1} for band 10 of VAS-D. This translates to a 0.5 K absolute and a 0.2 K relative at 300 K (or 1.5 K absolute and 0.6 K relative at 250 K). In-flight comparisons of observed radiances to the calculated values from radiosonde profiles reveal a 1.9 K difference for band 10. This method is susceptible to forward calculation errors. Comparing collocated fields of view of VAS (GOES-4) and HIRS (NOAA-6) radiances, Menzel et al. report an average absolute difference of 0.2 K for VAS band 10. Using a histogram approach for an area approximately 500 km x 500 km at the GOES sub-satellite point, Schmit and Herman note a mean difference of 0.3 K for HIRS versus VAS band 10.

Preliminary results

Figure 5-1a shows the 6.7 μm cloud cleared brightness temperature at 12 UTC from GOES 7, averaged over the month of July 1987. The warmer regions (colors yellow to orange) denote a relatively drier region in the upper troposphere. Figure 5-1b shows the corresponding value calculated from the daily weather analyses of the European Center for Medium Range Weather Forecasting (ECMWF). GOES data were not utilized in the analysis. This is not intended to be a definitive discussion of the capabilities of the ECMWF analyses, but rather an illustration of the types of comparison that can be made for any climate model.

In interpreting these images it should be remembered that a warmer brightness temperature corresponds to a drier upper troposphere, with each +5 K corresponding approximately to a reduction in the relative humidity by about one half. At a fixed water vapor concentration, increased brightness would indeed indicate a warmer atmosphere, but this effect is almost entirely compensated by using relative humidity as the measure. As is apparent around the rim, an increase in zenith angle from 0° to 60° is equivalent to a doubling of the line of sight moisture content, i.e. a reduction in the brightness temperature by about 5 K.

Each image shows clearly the major features of the Hadley cell circulation, with a moist band associated with the inter-tropical convergence zone some 10° north of the equator over central America and the eastern Pacific, and a dry band south of the equator extending all across South America and the Eastern Pacific. However, in the model generated fields the contrast between moist and dry regions seems to be insufficient.

Figure 5-2a shows the cloud forcing that was added to the original brightness temperatures to obtain the cloud cleared product in Figure 5-1a, whereas Figure 5-2b shows the difference in brightness temperature between the observations and the model. It will be noticed that, except in areas of deep convection in the ITCZ, the corrections associated with clouds are generally less than 1 K, corresponding roughly to a 15% change in relative humidity. This is substantially less than the differences between the model and observations.

Another feature apparent from Figure 5-2b is that the ECMWF model systematically overestimates the relative humidity above regions of persistent stratus. A similar problem is apparent in comparisons with the SSM/I precipitable water (not shown), which are dominated by the lower troposphere.

Product status

The cloud clearance and spatial averaging algorithms have been run on twice daily data for one month. No fundamental problems have been encountered to indicate that they should not be applied routinely on the Pathfinder 8 km data set for the benchmark period. However, further development is necessary to devise monitoring procedures and quality control information for operational implementation. A high priority science objective is to use available half hourly data to evaluate the diurnal cycle and hence the random error in individual data points for 1° squares, as well as an appropriate temporal sampling for large volume processing.

References

Chesters D. and A. Neuendorffer, 1991: The climatology of Upper Tropospheric water vapor observed in the 1980's using the TOVS 6.5 micron bands. Fifth Conference on Climate Variations, October 14-18, Denver Colorado, Amer. Meteor. Soc., 299-302.

Hayden C. M., T. J. Schmit, 1992: Quantitative Applications of the 6 Micrometer Water Vapor Band Measurements from Satellites. Sixth Conference on Satellite Meteorology and Oceanography, Atlanta, GA, Jan. 5-10, 188-192.

Menzel W. P., and W.L. Smith and L. D. Herman, 1981: Visible infrared spin-scan radiometer atmospheric sounder radiometric calibration: an inflight evaluation from intercomparisons with HIRS and radiosonde measurements. Applied Optics, Vol. 20, No. 20, 3641-3644.

Menzel W. P., 1980: Prelaunch Study Report of VAS-D Performance: a SSEC report to NASA under contract NAS5-21965. Available upon request.

Schmit T. J. and L. D. Herman, 1992: Comparison of Multi-spectral data: GOES-7 (VAS) to NOAA-11 (HIRS). Sixth Conference on Satellite Meteorology and Oceanography, Atlanta, GA, Amer. Meteor. Soc., 258-259.

Weinreb M. P., H. E. Fleming, L. M. McMillin and A. C. Neuendorffer, 1981: NOAA Tech Report NESS 85, National Oceanic and Atmospheric Administration, U.S. Department of Commerce, Washington D.C. 35pp.

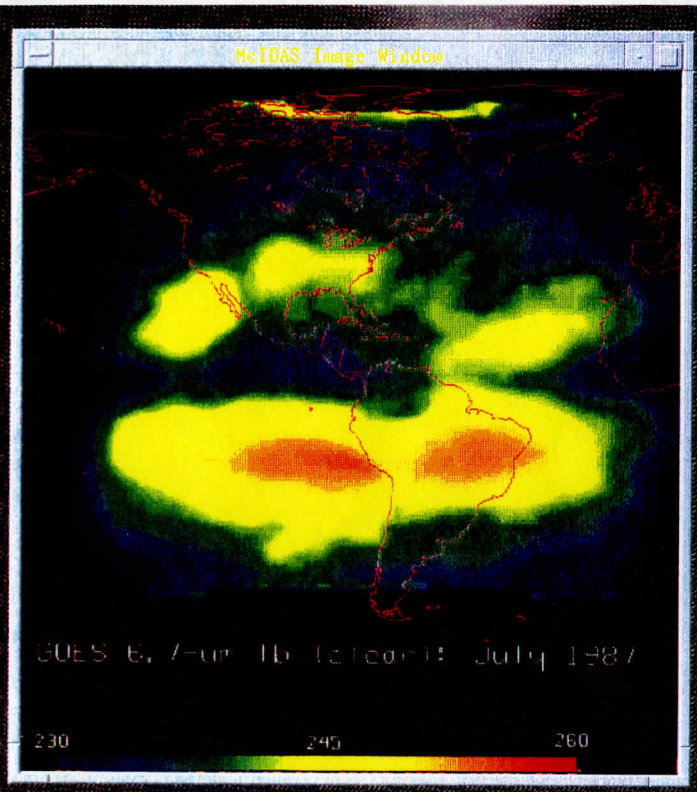

Fig.5-1a.

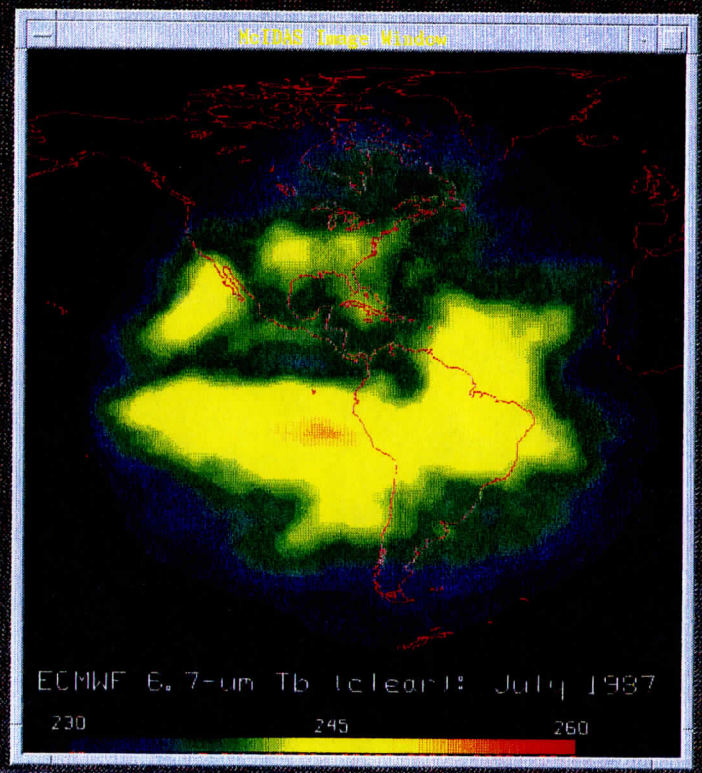

Fig.5-1b.

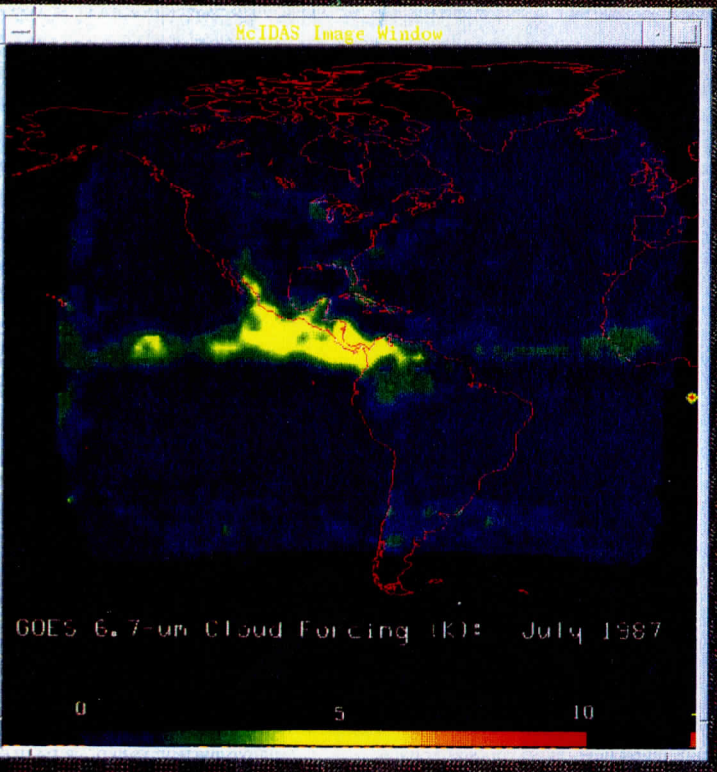

Fig.5-2a.

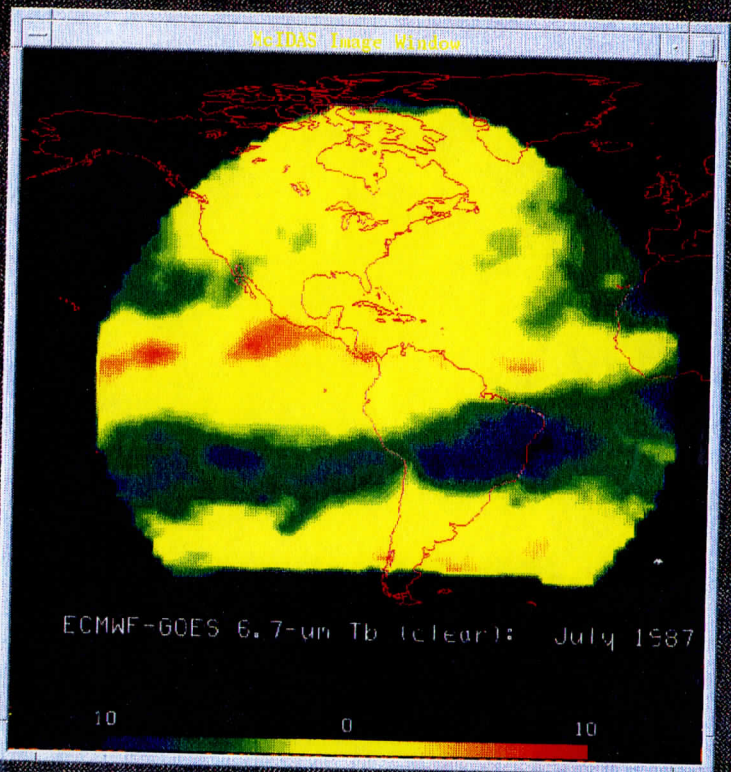

Fig.5-2b.

6. GOES Satellite Cloud Motion Vectors

W. Paul Menzel, NOAA/NESDIS/ASPP
Robert T. Merrill, CIMSS

Objective

To detect and track atmospheric motions at several levels with a sequence of satellite images.

Introduction

Geostationary satellite imagery has been used as a source of wind observations since the launch of the first spin scan camera aboard the Applications Technology Satellite in December 1966. It was recognized immediately that features tracked in a time sequence of images could provide estimates of atmospheric motion. Historically, wind vectors have been produced from images of visible (for low level vectors) and infrared longwave window radiation (for upper and low level vectors and some mid level vectors). More recently, in order to improve the coverage at mid levels and over cloud free areas, wind tracking has been applied to water vapor imagery (at 6.7 and 7.2 microns).

Method

The basic concept behind the cloud drift winds is that some clouds are passive tracers of the atmosphere's motion in the vicinity of the cloud. The elements of wind vector production have not changed since their inception. These are (a) selecting a feature to track or a candidate target, (b) tracking the target in a time sequence of images to obtain a relative motion, (c) assigning a pressure height (altitude) to the vector, and (d) assessing the quality of the vector.

Currently, the main problem of cloud motion vector (CMV) production is assigning cloud tracked motions to the correct heights. Thin clouds which are most likely to be passive tracers of the flow at a single level are the best tracers, but unfortunately their height assignments are especially difficult. Since the emissivity of the cloud is less than unity by an unknown and variable amount, its brightness temperature (T_b) in the infrared window is an overestimate of its actual temperature. Thus, heights for thin clouds inferred directly from the observed T_b and an available temperature profile are systematically low.

Height assignment errors carry a heavy penalty because of vertical wind shear, which is greatest near regions of active weather. For this reason, recent winds research at the Cooperative Institute for Meteorological Satellite Studies (CIMSS) has emphasized improved height assignments, and a two-channel method using the "CO_2 slicing" approach (Menzel et al., 1983) has been incorporated into the CIMSS winds algorithm (Merrill et al., 1991), and passed on to NESDIS operations as of February 12, 1992.

Figure 6-1 shows an example of a wind set produced from three half hourly infrared window images using the CO_2 height assignment; vectors at all levels are shown. Note that the CMV coverage is limited by cloud free regions which are rather extensive at times. The polar jet off the west coast of the US is captured quite well, largely due to proper height assignment. Figure 6-2 shows the water vapor winds produced from three hourly 6.7 micron images. The water vapor winds have much better horizontal coverage and complement the infrared to winds to broaden the polar jet and to extend it further east.

Status

The winds software is currently run automatically four times per day. Editing is accomplished automatically and with manual inspection. Other than the radiance data, atmospheric temperature and moisture profiles and surface data are used.

References

Merrill, R. T., W. P. Menzel, W. Baker, J. Lynch, E. Legg, 1991: A Report on the Recent Demonstration of NOAA's Upgraded Capability to Derive Satellite Cloud Motion Winds. Bull. Amer. Meteor. Soc., **72**, 372-376.

Menzel, W. P., W. L. Smith, and T. R. Stewart, 1983: Improved Cloud Motion Wind Vector and Altitude Assignment Using VAS. J. Appl. Met., **22**, No. 3, 377-384.

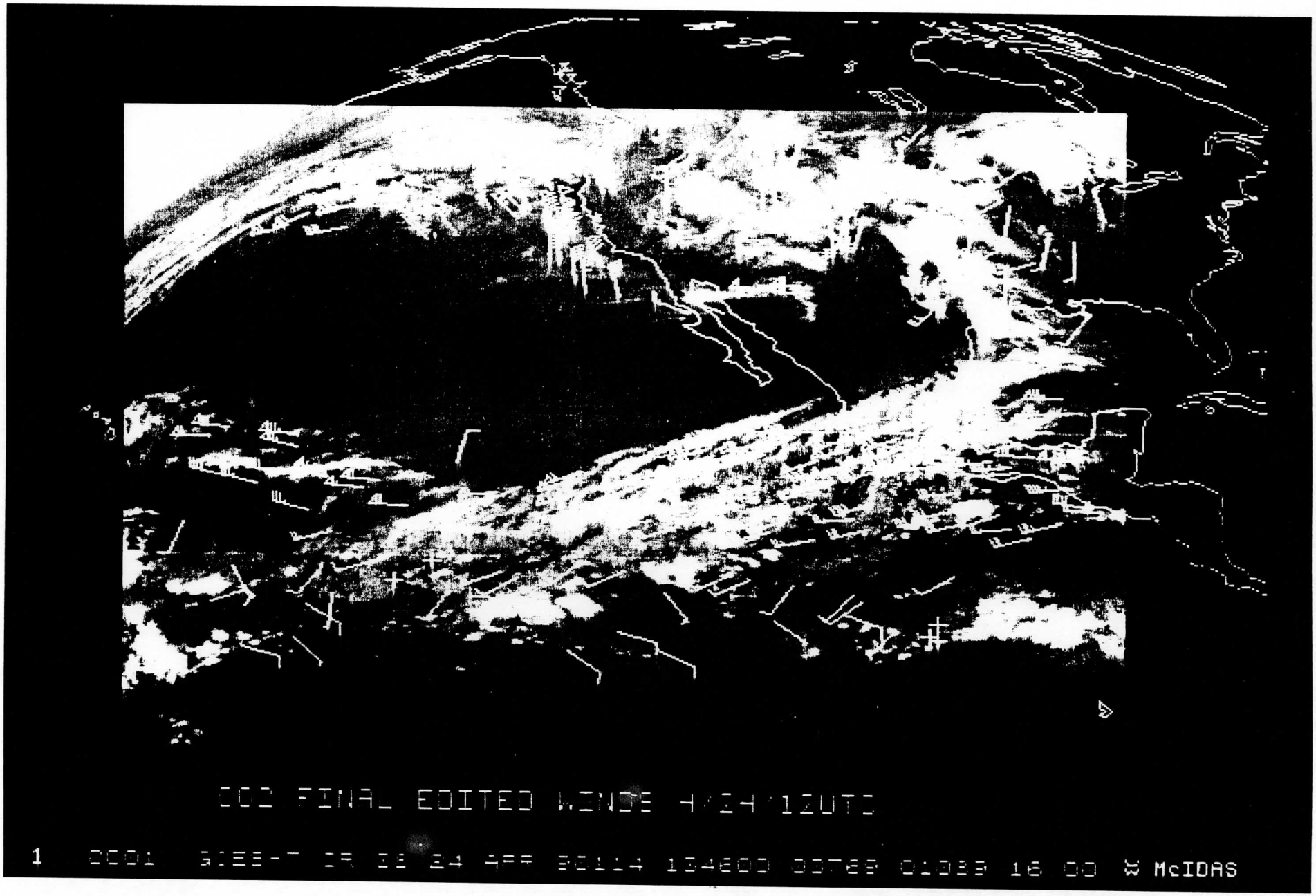

Figure 6-1. CMV set produced from three half hourly infrared window images using the CO_2 height assignment; vectors at all levels are shown. The winds are valid at 12 UTC on April 24, 1990.

Figure 6-2. Water vapor winds produced from three hourly 6.7 micron images for the same time at shown in Figure 6-1.

7. Geostationary Satellite Detection of Biomass Burning

Elaine M. Prins, CIMSS
W. Paul Menzel, NOAA/NESDIS/ASPP

Objective

To monitor the amount of biomass burning in South America using both the shortwave and longwave IR windows.

Introduction

CIMSS has demonstrated the capability of utilizing Geostationary Operational Environmental Satellite (GOES) Visible Infrared Spin Scan Radiometer Atmospheric Sounder (VAS) data to monitor biomass burning associated with deforestation and grassland management in South America. The GOES VAS infrared window (3.9 and 11.2 micron) data offer the opportunity to monitor biomass burning at selected times every day.

Method

The different brightness temperature responses in the two infrared window channels can be used to estimate the temperature of a target fire as well as the subpixel area it covers utilizing a technique developed by Matson and Dozier (1981) for NOAA polar orbiting Advanced Very High Resolution Radiometer (AVHRR) data.

Considerable efforts using the NOAA polar orbiting data have realized some success. Unfortunately the AVHRR provides limited opportunity to monitor fires during peak burning times (around 15:30 UTC or 12:30 local time), and many fire observations saturate the sensor. Although VAS data do not offer the spatial resolution available with AVHRR data (14 km versus 1 km, respectively), this decreased resolution does not seem to hinder the ability of the VAS instrument to detect fires. Sequences of VAS visible data are helpful in verifying that the hot spots sensed in the infrared are actually related to fires. Furthermore, the smoke of the fires can be tracked in time to determine their motion and trajectory. The GOES satellite offers the unique ability to monitor diurnal variations in fire activity and transport of aerosols (Prins and Menzel, 1992).

Typically the difference in brightness temperatures between the two infrared windows at 3.9 and 11.2 microns is 2-4 K due to reflected solar radiation, surface emissivity differences, and water vapor attenuation. Larger differences occur when one part of a pixel is substantially warmer than the rest of the pixel. The hotter portion of the pixel will contribute more radiance in the shorter wavelengths than in the longer wavelengths. This can be seen in figure 7-1 which shows a 3.9 and a 11.2 micron image at 15:31 UTC on 14 August 1983 in South America. The location of 10 fires have been indicated on the images. Notice that

those pixels containing fires are darker, ie hotter, in the 3.9 micron image than in the 11.2 micron image.

Status

The algorithm to determine fire extent and temperature is currently too cumbersome and time consuming to be used operationally. It is strongly dependent on image interpretation and very sensitive to corrections for cloud and haze. To avoid the uncertainty associated with the smoke correction, CIMSS is investigating the possibility of assigning an average fire target temperature to any given fire and solving for a relative fire area (Prins and Menzel, 1992). Currently an operator can utilize McIDAS in an interactive mode to determine the relative extent of a fire assuming a target temperature of 450 K. Work must be done to identify appropriate techniques to use for cloud and haze corrections as well as reasonable fire temperatures. Data from the Biomass burning Airborne and Spaceborne Experiments (BASE-A and B) conducted in the Amazon region in 1989 and 1990 are being used to develop and refine the algorithm. Once the algorithm has been made more objective in terms of fire identification and smoke correction, the technique could be automated to determine the trends of biomass burning in the Amazon during the past decade using the GOES archive.

References

Matson, M., and J. Dozier, 1981: Identification of subresolution high temperature sources using a thermal IR sensor. Photogrammetric Engineering and Remote Sensing, 47, 1311-1318.

Prins, E.M., and W.P. Menzel, 1992: Geostationary satellite detection of biomass burning in South America, accepted for publication by International Journal of Remote Sensing.

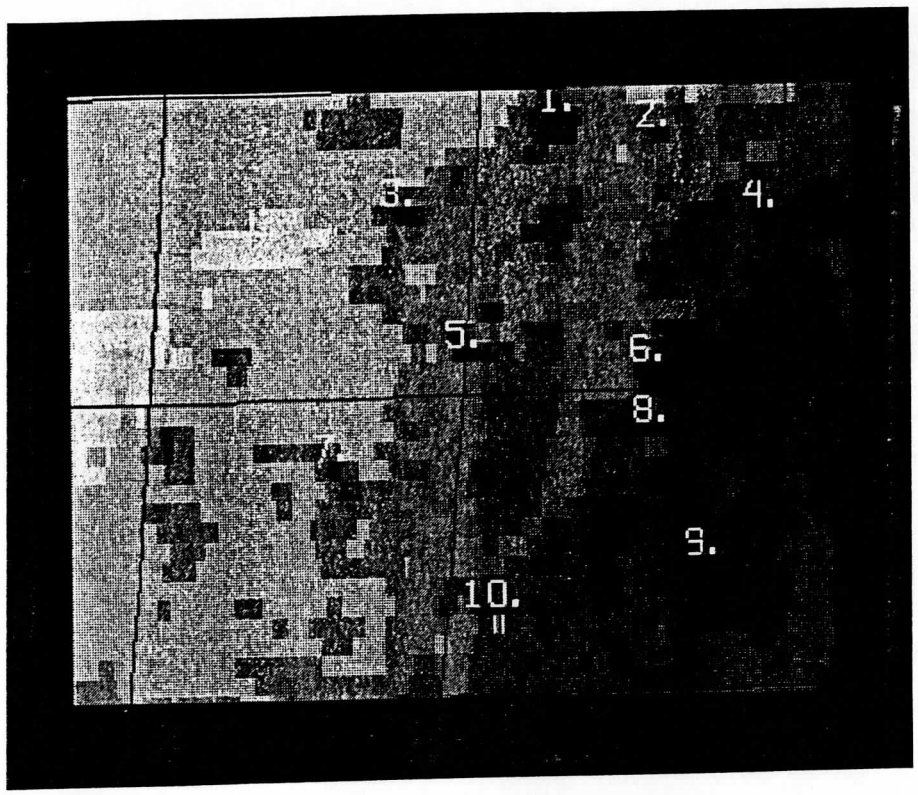

(a).

(b).

Figure 7-1. (a) VAS 3.9 micron image and (b) 11.2 micron image centered at 8° South and 50° West in Brazil (latitude and longitude lines are spaced every 2 degrees). The image is valid 15:30 UTC on August 14, 1983.

8. An Example of Continental Atmospheric Stability

Gary Wade, NOAA/NESDIS/SDAB
Christopher M. Hayden, NOAA/NESDIS/SDAB

Objective

To monitor the diurnal trends of atmospheric stability using the GOES archive.

Introduction

Atmospheric stability is best determined from an in situ temperature and moisture profile retrieval. To achieve good horizontal coverage it is necessary to rely on the GOES. The GOES does have sufficient radiance information to adjust a guess profile to better reflect the current local atmospheric state.

Method

Through measurements in several narrow and carefully selected spectral intervals, the temperature of the atmosphere or the concentration of the attenuating gas, as a function of atmospheric pressure level, is inferred by inverting the process of radiative transfer. Temperature profiles are derived using the emission from CO_2 in the atmosphere, and concentrations of moisture are then inferred with emissions from H_2O in the atmosphere. Surface temperatures are inferred from observations in the spectral regions where the atmosphere is most transparent. The GOES has spectral channels sensitive to CO_2 and H_2O.

The computation of profiles from a selected set of radiance observations involves several steps: (1) construction of first guess temperature and moisture profiles from a numerical forecast with analyzed surface data, (2) forward calculation in a radiative transfer formulation of probable observed radiances for the relevant spectral channels, and (3) simultaneous solution in a least squares formulation of the radiative transfer equation in perturbation form to determine the adjustment in the guess temperature and moisture profiles necessary to better match the observed radiances (Hayden, 1988). Once the profiles are in place, atmospheric stability can be calculated.

One measure of the thermodynamic stability of the atmosphere is the lifted index (LI), which is the difference between the measured 500 mb temperature and that calculated from lifting a parcel of air from ground level dry adiabatically to the local condensation level and then moist adiabatically to 500 mb. The more negative the value, the less stable the atmosphere; satellite derived values less than -6 indicate very unstable atmospheric conditions in which severe thunderstorms are likely. Figure 8-1 shows the lifted indices over North America derived from VAS soundings; in clear or partly cloudy conditions, the LI has been displayed in varying colors to indicate magnitudes, while in cloudy conditions where infrared sounding was not possible, the cloud image is presented. These derived product images have been described in the literature (Smith et al., 1985).

Figure 8-2 shows a time sequence of average values of the lifted index over central US and the Gulf of Mexico for 9 September 1991 (day 252 into day 253). In the left panels we see that the morning atmospheric stability is followed by the afternoon destabilization over land which contrasts with the constant unstable average seen over the Gulf. The right panels show of number of clear samples as the day progresses.

Status

The GOES offers the opportunity to monitor diurnal changes in atmospheric stability over certain regions and to correlate this with cloud developments.

Lifted indices over Continental United States are determined hourly using the algorithms described in the referenced literature.

References

Hayden, C. M., 1988: GOES-VAS Temperature-Moisture Retrieval Algorithm. Jour. Appl. Meteor., **27**, 705-733.

Smith, W. L., G. S. Wade, and H. M. Woolf, 1985: Combined Atmospheric Sounding/Cloud Imagery - A New Forecasting Tool. Bull. Amer. Meteor. Soc., **66**, 138-141.

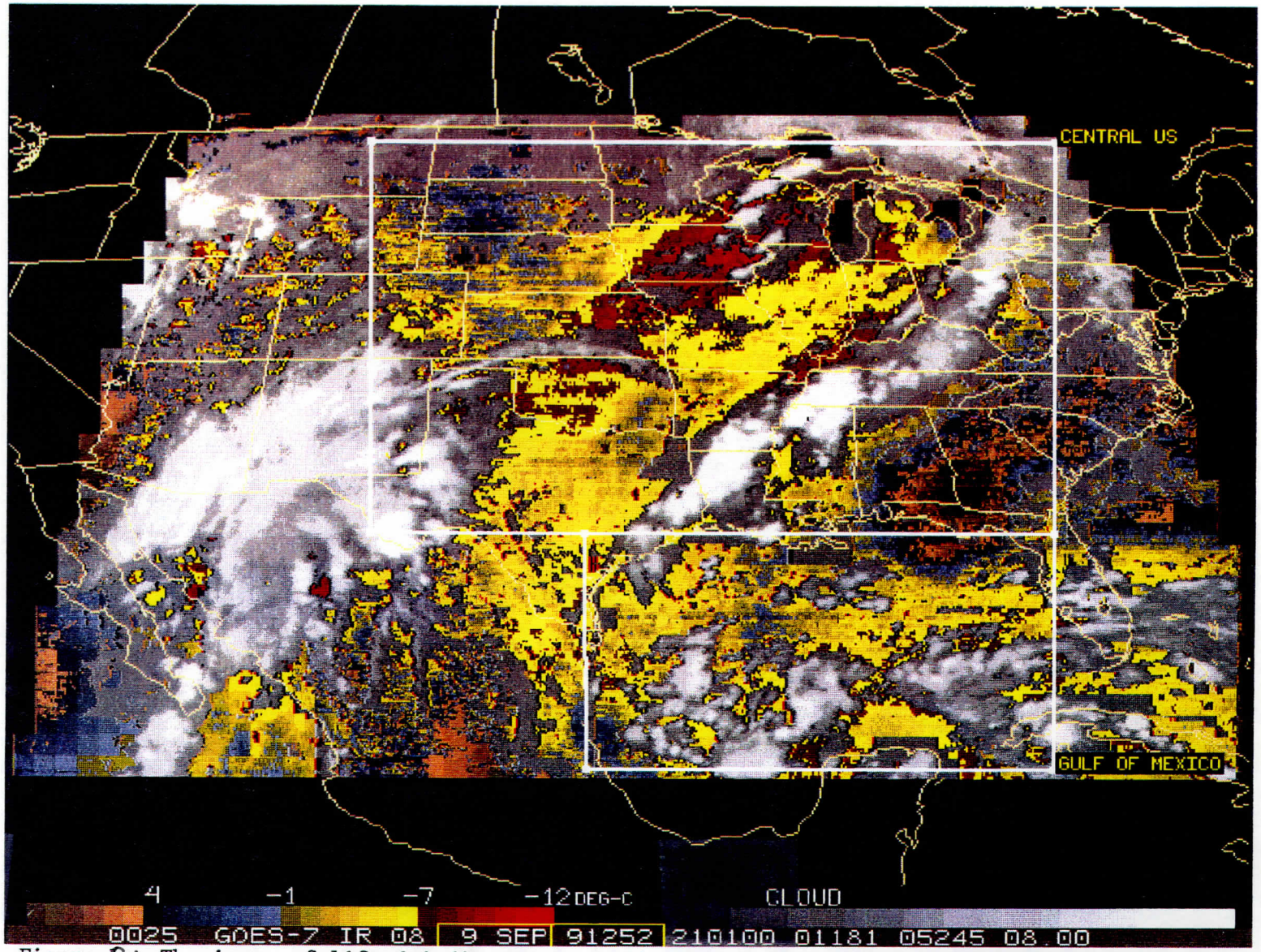

Figure 8.1 The image of lifted indices over North America derived from VAS soundings; in clear or partly cloudy conditions, the LI has been displayed in varying colors to indicate magnitudes, while in cloudy conditions where infrared sounding was not possible, the cloud image is presented. The data is from September 9, 1991.

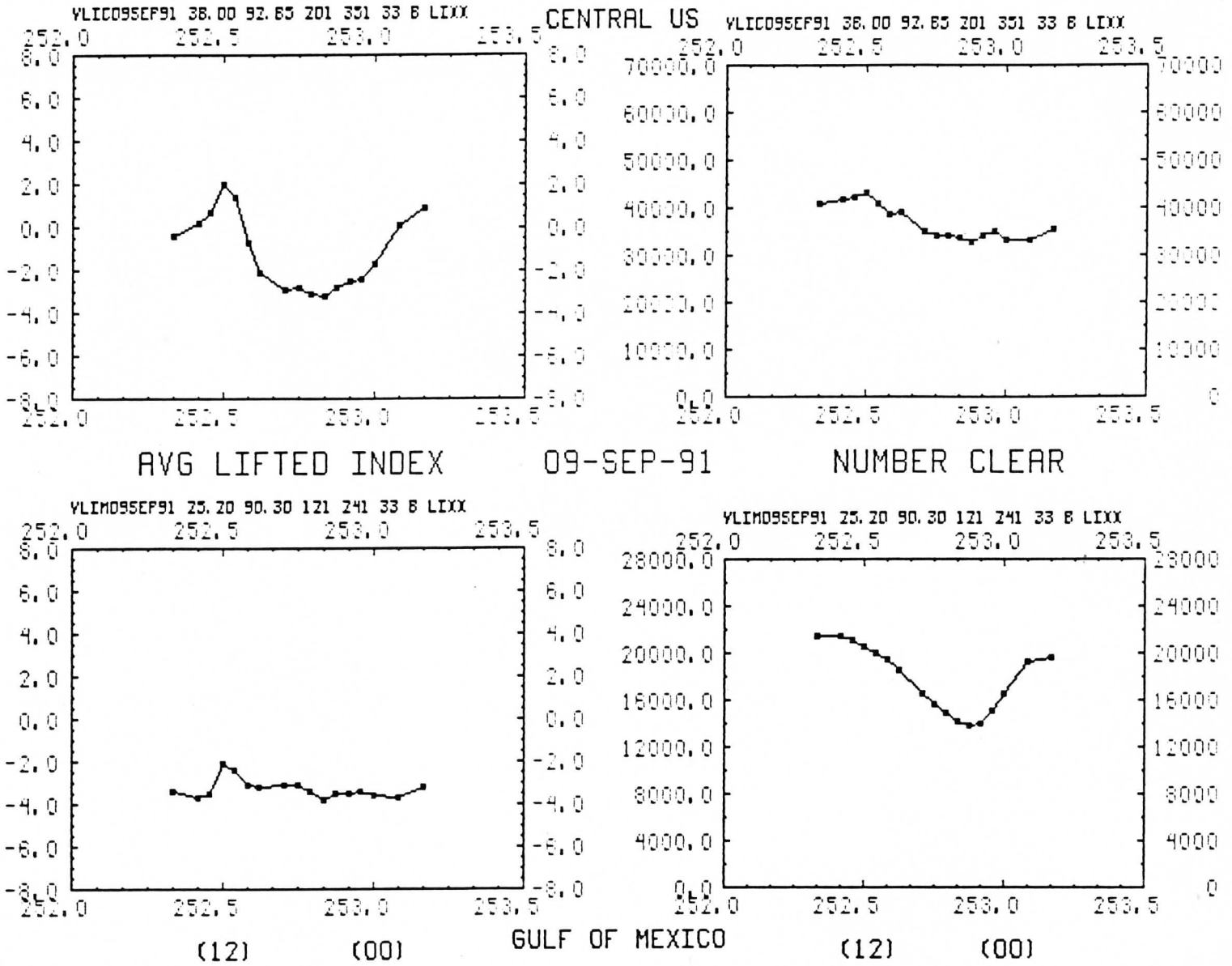

Figure 8-2. Time sequence of average values of the lifted index over central US and the Gulf of Mexico for 9 September 1991 (day 252 into day 253). Left panels show the atmospheric stability. The right panels show of number of clear samples.

9. Complete reference list: The GOES Pathfinder Sampler

Chesters D. and A. Neuendorffer, 1991: The climatology of Upper Tropospheric water vapor observed in the 1980's using the TOVS 6.5 micron bands. Fifth Conference on Climate Variations, October 14-18, Denver Colorado, Amer. Meteor. Soc., 299-302.

Hayden, C. M., 1988: GOES-VAS Temperature-Moisture Retrieval Algorithm. Jour. Appl. Meteor., **27**, 705-733.

Hayden C. M., T. J. Schmit, 1992: Quantitative Applications of the 6 Micrometer Water Vapor Band Measurements from Satellites. Sixth Conference on Satellite Meteorology and Oceanography, Atlanta, GA, Jan. 5-10, 188-192.

Herman, L. D. and W. L. Smith, 1986: Intercomparison of preliminary earth radiation budget satellite (ERBS) flux estimates and geostationary satellite multispectral VAS radiance measurements. 6th Conference on Atmospheric Radiation, 13-16 May 1986, Williamsburg, VA, AMS, Boston, MA.

Matson, M., and J. Dozier, 1981: Identification of subresolution high temperature sources using a thermal IR sensor. Photogrammetric Engineering and Remote Sensing, **47**, 1311-1318.

Menzel W. P., 1980: Prelaunch Study Report of VAS-D Performance: a SSEC report to NASA under contract NAS5-21965. Available upon request.

Menzel W. P., and W.L. Smith and L. D. Herman, 1981: Visible infrared spin-scan radiometer atmospheric sounder radiometric calibration: an inflight evaluation from intercomparisons with HIRS and radiosonde measurements. Applied Optics, Vol. 20, No. 20, 3641-3644.

Menzel, W. P., W. L. Smith, and T. R. Stewart, 1983: Improved Cloud Motion Wind Vector and Altitude Assignment Using VAS. J. Appl. Met., **22**, No. 3, 377-384.

Menzel, W. P., D. P. Wylie, and K. I. Strabala, 1991: Seasonal and Diurnal Changes in Cirrus Clouds as seen in Four Years of Observations with the VAS. accepted by J. Appl. Met.

Merrill, R. T., W. P. Menzel, W. Baker, J. Lynch, E. Legg, 1991: A Report on the Recent Demonstration of NOAA's Upgraded Capability to Derive Satellite Cloud Motion Winds. Bull. Amer. Meteor. Soc., **72**, 372-376.

Prins, E.M., and W.P. Menzel, 1992: Geostationary satellite detection of biomass burning in South America, accepted for publication by International Journal of Remote Sensing.

Reinke D. L., C. L. Combs, S. Q. Kidder, T. H. Vonder Haar, 1992: Satellite Cloud Composite Climatologies: A New High-resolution Tool in Atmospheric Research and Forecasting. Accepted by Bull. Amer. Meteor. Soc.

Schmit T. J. and L. D. Herman, 1992: Comparison of Multi-spectral data: GOES-7 (VAS) to NOAA-11 (HIRS). Sixth Conference on Satellite Meteorology and Oceanography, Atlanta, GA, Amer. Meteor. Soc., 258-259.

Smith, W. L., G. S. Wade, and H. M. Woolf, 1985: Combined Atmospheric Sounding/Cloud Imagery - A New Forecasting Tool. Bull. Amer. Meteor. Soc., **66**, 138-141.

Weinreb M. P., H. E. Fleming, L. M. McMillin and A. C. Neuendorffer, 1981: NOAA Tech Report NESS 85, National Oceanic and Atmospheric Administration, U.S. Department of Commerce, Washington D.C. 35pp.

Wylie, D. P. and W. P. Menzel, 1989: Two Years of Cloud Cover Statistics Using VAS. Jour. Clim., Vol. 2, No. 4, 380-392.

Weinreb M. P., H. E. Fleming, L. M. McMillin and A. C. Neuendorffer, 1981: NOAA Tech Report NESS 85, National Oceanic and Atmospheric Administration, U.S. Department of Commerce, Washington D.C. 35pp.

10. Select GOES Pathfinder Sampler references

Wylie, D. P. and W. P. Menzel, 1989: Two Years of Cloud Cover Statistics Using VAS. Jour. Clim., Vol. 2, No. 4, 380-392.

Hayden, C. M., 1988: GOES-VAS Temperature-Moisture Retrieval Algorithm. Jour. Appl. Meteor., **27**, 705-733.

Reinke D. L., C. L. Combs, S. Q. Kidder, T. H. Vonder Haar, 1992: Satellite Cloud Composite Climatologies: A New High-resolution Tool in Atmospheric Research and Forecasting. Accepted by Bull. Amer. Meteor. Soc.

Merrill, R. T., W. P. Menzel, W. Baker, J. Lynch, E. Legg, 1991: A Report on the Recent Demonstration of NOAA's Upgraded Capability to Derive Satellite Cloud Motion Winds. Bull. Amer. Meteor. Soc., **72**, 372-376.

Prins, E.M., and W.P. Menzel, 1992: Geostationary satellite detection of biomass burning in South America, accepted for publication by International Journal of Remote Sensing.

Reprinted from JOURNAL OF CLIMATE, Vol. 2, No. 4, April 1989
American Meteorological Society

Two Years of Cloud Cover Statistics Using VAS

D. P. WYLIE

W. P. MENZEL

Two Years of Cloud Cover Statistics Using VAS

D. P. WYLIE

Space Science and Engineering Center, University of Wisconsin–Madison

W. P. MENZEL

NOAA/NESDIS, Advanced Satellite Products Project, Madison, Wisconsin

(Manuscript received 24 June 1988, in final form 1 November 1988)

ABSTRACT

Statistics of cloud characteristics over North America have been accumulated for the past 2 yr. The frequency of cloud cover with the associated heights and infrared attenuation were charted using the CO_2 channel radiometric data from the VISSR Atmospheric Sounder (VAS). Cloud top pressures were determined from the ratio of VAS CO_2 channel radiances in a radiative transfer equation formulation. Cloud emissivities were then calculated from infrared window channel observations. The VAS CO_2 derived cloud top height and emissivity assignments have been found to be reliable in most cloud types, including thin cirrus clouds where other techniques have been inconsistent. Observations since 1985 reveal that 20%–30% of the United States was covered with thin semitransparent clouds (radiative attenuation was less than 95%), 45% was covered with thick opaque clouds, and 25%–35% had clear sky conditions. It is likely that 5% of the opaque cloud should have been identified as semitransparent cirrus. The geographical distribution of cloud cover shows a latitudinal dependence mainly over the Pacific Ocean. Moderate seasonal and diurnal changes were also found which agree with other published cloud studies.

1. Introduction

The frequency of cirrus clouds usually has been underestimated in cloud population studies. Satellite methods of analyzing cloud cover often mistake cirrus clouds for lower-level clouds or completely miss them. Most infrared window techniques do not correct for the transparency of the cirrus clouds and underestimate their altitude because their infrared brightness temperatures are warmer than the temperature associated with their true altitudes (Szejwach 1982). Thin cirrus are especially hard to identify on visible satellite images because they reflect little solar radiation and appear as dark or broken cloud fields. With the multispectral infrared sensor on the GOES VAS satellite, reliable identification of most cirrus is now possible.

The CO_2 technique for deriving cloud top pressures (Chahine 1974; Smith et al. 1974) was first applied to data from the VISSR Atmospheric Sounder (VAS) infrared sensor by Menzel et al. (1983). The technique takes advantage of the differing partial CO_2 absorption in several of the infrared channels, making each channel sensitive to a different level in the atmosphere. Clouds appear in the CO_2 channel images according to their level in the atmosphere. Low clouds will not appear at all in the high-level channels, while high clouds appear in all channels. By modeling the upwelling infrared radiation from the earth-atmosphere system in several of the VAS CO_2 channels simultaneously, it is possible to infer the cloud top pressure independent of the radiative transmissivity of the cloud. This gives the CO_2 technique the ability to distinguish thin cirrus clouds that would normally be missed by other techniques due to the transmission of terrestrial radiation through the cirrus.

The CO_2 technique has been installed on the Man-computer Interactive Data Access System (McIDAS) at the University of Wisconsin–Madison. It has been run operationally with the GOES VAS imagery since October 1985. Statistics on cloud cover, especially cirrus cloud cover, have been gathered for the continental United States and its bordering oceans. This paper describes the technique and presents some of the results of this program.

2. Technique description

The VAS radiometer detects infrared radiation in 12 spectral bands that lie between 3.9 and 15 μm at 7 or 14 km resolution in addition to visible reflections at 1 km resolution. The 15 μm CO_2 band channels provide good sensitivity to the temperature of relatively cold regions of the atmosphere. A demonstration of

Corresponding author address: Dr. D. P. Wylie, University of Wisconsin–Madison, 1225 West Dayton Street, Madison, Wisconsin 53706.

the vertical resolution of the three relevant CO_2 channels is given by the temperature profile weighting functions shown in Fig. 1. Each curve in the figure shows the sensitivity to local variations in atmospheric temperature of the radiance observed in the spectral interval of the indicated channel. Only clouds above the 350 mb level contribute significantly to the radiance to space observed by the 14.2 μm band (VAS channel 3), while the 14.0 μm band (VAS channel 4) senses down to 700 mb and the 13.3 μm band (VAS channel 5) senses down near the surface of the earth.

To assign a cloud top pressure to a given cloud element, the CO_2 technique is employed. As shown by Smith and Platt (1978), the ratio of the deviations in cloud-produced radiances, $I(\nu)$, and the corresponding clear air radiances, $I_{cl}(\nu)$, for two spectral channels of frequency ν_1 and ν_2 viewing the same field-of-view can be written as

$$\frac{I(\nu_1) - I_{cl}(\nu_1)}{I(\nu_2) - I_{cl}(\nu_2)} = \frac{\epsilon_1 \int_{P_s}^{P_c} \tau(\nu_1, p) \dfrac{dB[\nu_1, T(p)]}{dp}\, dp}{\epsilon_2 \int_{P_s}^{P_c} \tau(\nu_2, p) \dfrac{dB[\nu_2, T(p)]}{dp}\, dp}. \quad (1)$$

In this equation, ϵ is the cloud emissivity, P_s the surface pressure, P_c the cloud pressure, $\tau(\nu, p)$ the fractional transmittance of radiation of frequency ν emitted from the atmospheric pressure level (p) arriving at the top of the atmosphere ($p = 0$), and $B[\nu, T(p)]$ is the Planck radiance of frequency ν for temperature $T(p)$. If the frequencies are close enough together, then ϵ_1 approximates ϵ_2, and one has an expression by which the pressure of the cloud within the field-of-view (FOV) can be specified. The left side of Eq. 1 is determined from the VAS observed radiances in a given FOV and the clear air radiances inferred from spatial analyses of VAS clear radiance observations in neighboring FOVs. The right side of Eq. 1 is calculated from a temperature profile and the profiles of atmospheric transmittance for the spectral channels as a function of P_c, the cloud top pressure (1000 to 100 mb is spanned by discrete values at 50 mb intervals). In this study, global analyses of temperature and moisture fields from the National Meteorological Center (NMC) are used. The optimum cloud top pressure is determined with Eq. (1) when the absolute difference of left (ν_1, ν_2) minus right (ν_1, ν_2, P_c) is a minimum.

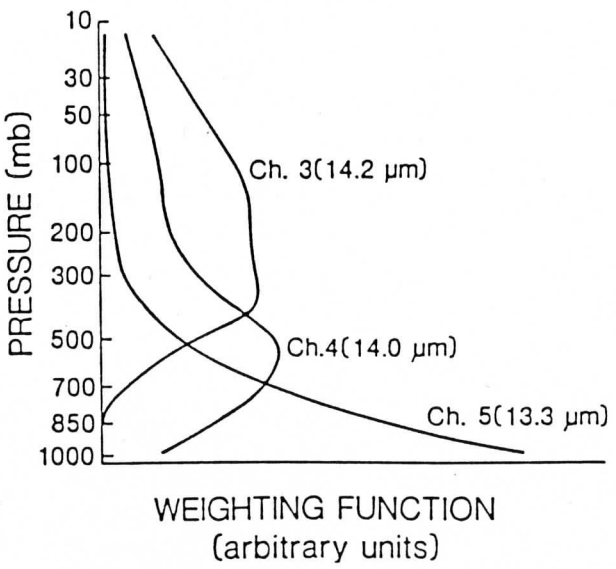

FIG. 1. The temperature profile weighting function of radiance to space as a function of emitting level for the VAS CO_2 spectral bands centered at 14.2, 14.0 and 13.3 μ.

Once a cloud height has been determined, an effective cloud amount (also referred to as effective emissivity in this paper) can be evaluated from the infrared window channel data using the relation

$$N\epsilon = \frac{I(w) - I_{cl}(w)}{B[w, T(P_c)] - I_{cl}(w)}. \quad (2)$$

Here N is the fractional cloud cover within the FOV, $N\epsilon$ is the effective cloud amount, w represents the window channel frequency, and $B[w, T(P_c)]$ is the opaque cloud radiance.

Using the ratios of radiances of the three CO_2 spectral channels, three separate cloud top pressures can be determined (14.2/14.0, 14.0/13.3, and 14.2/13.3). If ($I - I_{cl}$) is within the noise response of the instrument (roughly 1 mW/m^2/st/cm^{-1}), the resulting P_c is rejected. Using the infrared window and the three cloud top pressures, three effective cloud amount determinations are made. As described by Menzel et al. (1983), the most representative cloud height and amount are those that best satisfy the radiative transfer equation for the three CO_2 channels.

If no ratio of radiances can be reliably calculated because $I - I_{cl}$ is within the instrument noise level, then a cloud top pressure is calculated directly from the VAS observed 11.2 μm infrared-window channel brightness temperature comparison with the temperature profile, and the effective emissivity is assumed to be unity. This occurs for most low clouds below 700 mb; here, the CO_2 technique cannot find a pair of weighting functions where both have adequate sensitivity. In this way, all clouds are assigned a cloud top pressure either by the CO_2 ratios or the infrared window calculations.

Fields of view are determined to be clear or cloudy through inspection of the 11.2 μm brightness temperature with a split window correction for moisture absorption. If the moisture-corrected 11.2 μm brightness temperature is within 2 K of the known surface temperature (taken from the 1000 mb NMC model analysis adjusted with service A hourly observations), then the FOV is assumed to be clear and no cloud parameters are calculated.

The VAS CO_2 technique is independent of the fractional cloud cover; heights and effective cloud emis-

sivities can be determined for partially cloudy FOVs. However, there are a few caveats. The effective cloud emissivity is assumed to be independent of wavelength. The cloud is assumed to be of infinitesimal thickness; Smith and Platt (1978) have indicated that this introduces errors approaching one-half (one-quarter) the thickness of the cloud for optically thin (thick) clouds where the integrated emittance is less than (greater than) 0.6. The VAS CO_2 technique assumes the presence of only one cloud layer; when multiple layers are sensed, it derives a cloud altitude in-between the altitudes of the two separate layers. Because the VAS FOV resolution is coarse (7 km), very small element clouds are difficult to detect. Also, because the weighting functions for the VAS channels are broad, the vertical resolution is limited: cloud top pressure determinations are made within 50 mb intervals. Nonetheless, reliable cloud statistics can be calculated with appropriate application of the technique (Wielicki and Coakley 1981; Eyre and Menzel 1988).

The CO_2 technique is also applicable to data from the polar orbiting High-Resolution Infrared Radiometer Sounder (HIRS). Menzel et al. (1986) found comparable results from VAS and HIRS over the same cloud field. A similar approach has also been developed by Susskind et al. (1987) to process global cloud characteristics with HIRS and MSU (Microwave Sounding Unit) data.

Since October 1985, the CO_2 technique has been applied to GOES-East VAS sounding data over the United States at least twice daily (near 1200 and 0000 UTC) and as often as four times daily (near 0600, 1200, 1800, and 0000 UTC). In this study, radiances for three FOVs were averaged for cloud height and amount determinations (representing an area of 7 by 21 km at the satellite subpoint) at roughly 100 km spacing. Surface observations were used to adjust the global forecast temperature and moisture fields. No adjustments for topography were made. Transmittances were determined from line-by-line calculations with the spectral response functions for the appropriate VAS channels.

3. Technique accuracy

To assess the accuracy of this method, we compared the VAS CO_2 derived cloud heights to three other independent sources of cloud height information: 1) radiosonde moisture profiles, 2) lidar scans of clouds, and 3) satellite stereo parallax measurements. The limits of cirrus detection with the CO_2 technique were also investigated.

a. Comparisons to radiosonde moisture profiles

The VAS CO_2 cloud heights were compared to cloud tops defined by radiosonde moisture profiles. Radiosonde moisture profiles sometimes show a dramatic change from a saturated or nearly saturated layer to a dry layer as the sonde emerges from the cloud top. The dewpoint will drop from near saturation to 20 K depression. More often the moisture sensor does not show the cloud top, as it stops providing data somewhere inside the cloud. However, a sufficient number of CO_2 and radiosonde comparisons were accomplished from data for February and March 1986. All the moisture profiles where this signature was apparent were screened and were then compared to the VAS CO_2 cloud top heights colocated in space and time within 100 km and one hour of the sounding. The results for 24 comparisons are shown in Fig. 2.

Most of the cloud reports in the radiosonde comparisons were from opaque or nearly opaque clouds. The radiosonde sensor has little sensitivity at cold temperatures and high altitudes where light cirrus clouds are found. Thus, all cloud heights below 600 mb in Fig. 2 are comparisons from opaque clouds. However, some of the higher reports from 300 to 400 mb are semitransparent cirrus.

The VAS cloud heights are close to the radiosonde determined cloud heights. The average deviation is 40 mb for all comparisons.

b. Lidar comparisons

Lidars were used for scanning cirrus clouds during FIRE (First International Satellite Cloud Climatology Project Regional Experiment) over Wisconsin in October and November 1986 (see Cox et al. 1987 and Starr 1987). Lidars were operated from four sites in Wisconsin and from one aircraft. Data from the lidars at Madison and Wausau, Wisconsin, and from NASA's

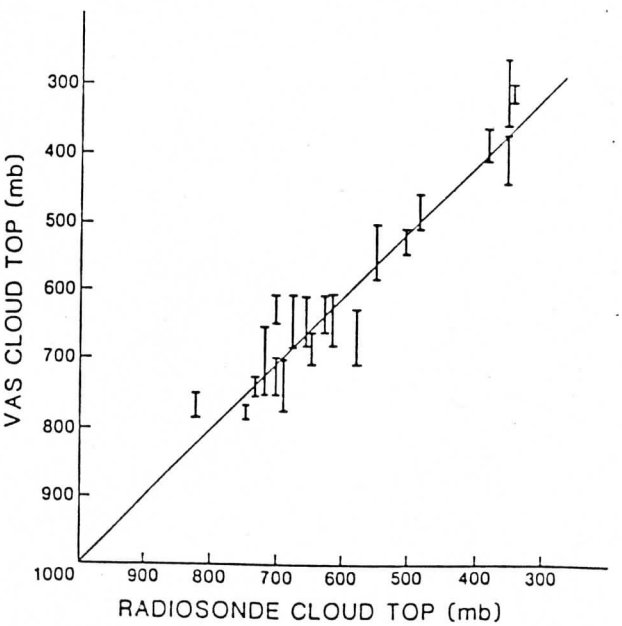

FIG. 2. The VAS CO_2 cloud heights compared to cloud heights determined from radiosonde moisture profiles during February and March 1986. Bars show the range of VAS cloud heights within 100 km of the radiosonde station.

ER2 aircraft were incorporated into the McIDAS data base for these comparisons.

The lidar observations from both sides of the cirrus clouds indicated that cirrus do not have sharp boundaries at their tops, which were found to vary over 1 to 2 km. There were often thin cirrus layers overlaying thicker cirrus and other cloud layers. The thin cirrus layers also had large spatial variances in density. These two characteristics gave the cirrus a variable cloud top height.

Comparisons of lidar-measured cloud top heights to VAS CO_2 height determinations were difficult. The size of the breaks in cirrus clouds (10–12 km) were approximately the same size as the resolution of the VAS sensor at 45° lat (10 km). Also, the VAS CO_2 channel observations were made in a "venetian blind" manner; the sensor was turned on for four swaths (roughly 40 km) in the north–south direction and then turned off for four swaths. The alternating pattern prevented the VAS CO_2 data from directly covering the lidar ground sites. It usually scanned within 20 km north or south of the sites, but seldom directly over them. Temporal collocation problems were encountered with the lidar ER2 flights. These problems made simultaneous single FOV comparisons difficult. Instead, comparisons were made over time and space scales of 50 km and 30 minutes, necessitating an assumption of uniform cloud top heights.

For comparison between the VAS and lidars, the highest cloud top reported by the lidars was compared to the height calculated by the VAS technique. Situations where lower clouds obscured higher cirrus in the lidar observations were avoided. Figure 3 shows a plot of the mean and standard deviations of all the VAS cloud top pressures found in the vicinity of the lidar observations. Each open circle in Fig. 3 indicates the mean of all VAS determinations and the bar shows the spread of one standard deviation (only the VAS CO_2 variability is shown; the lidar variability was of the order of 50 mb). The number of VAS observations is written next to the circle; over 100 comparisons were made. On the average, the VAS cloud top heights were 70 mb lower than the highest cloud tops reported by the lidars. Some of the VAS cloud top heights were higher than the lidar cloud tops, as the large spread of the one standard deviation bar indicates, but the majority were 50 to 100 mb lower. The largest discrepancy between the VAS and lidar cloud top observations occurred for cloud heights between 180 and 250 mb. A possible explanation lies in the fact that the VAS CO_2 cloud top pressure is based on a thin layer calculation and therefore can be off by as much as one-half the cloud thickness. Since cirrus clouds appear to have diffuse radiative properties over 1 to 3 km, it is reasonable that the CO_2 cloud height reports would be somewhere in this layer but not at the top. The CO_2 cloud top pressure (P_c in Eq. 1) indicates the level of denser cirrus or strongest radiative attenuation rather than the true cloud top height. Further studies of vertical extinction profiles are being made with lidar data to understand the radiative properties of cirrus clouds.

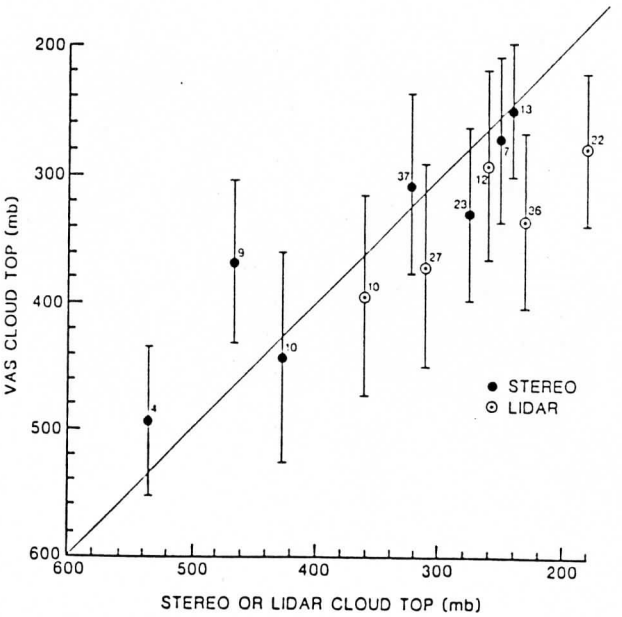

FIG. 3. The mean and standard deviations of all VAS cloud top pressure data compared to lidar and satellite stereo cloud top pressures. The error bars indicate one standard deviation from the mean for the VAS derived pressures. The number of VAS cloud reports in each comparison are indicated. No error bars are shown for the lidar and stereo data.

c. *GOES stereo comparisons*

Another independent measurement of cloud top heights was made from the stereo parallax observed with the two GOES satellites. From 23–29 February 1988, the scan times of the two GOES satellites were synchronized for three times each day. This produced image pairs from which stereo parallax measurements of cloud heights were made. The method for calculating cloud top height from stereo parallax was described by Bryson (1978) and Hasler (1981).

Stereo parallax measurements were made by remapping the GOES-West image into the projection of GOES-East (see Fig. 4). The image registration was corrected so that landmarks and coastlines were aligned. Clouds then appeared to be displaced on one image with respect to their position on the other image. The parallax shift occurs in the east–west direction and the magnitude of the shift is nearly equal to the altitude of the cloud top. Thus, a 10 km high cloud has approximately a 10 km parallax shift. The accuracy of measuring parallax shift was limited by the resolution of the visible sensor (approximately 1 km).

Stereo parallax measurements were made for clouds from 90° to 130°W longitude. The best stereo viewing occurred along the 105°W meridian which is equidistant from either satellite. Measurements were made

FIG. 4. The GOES-East and GOES-West visible images of Texas at 1701 UTC 23 February 1988. The west image has been remapped into the projection of the east. The CO_2 derived cloud top pressures (mb 10^{-1}) are indicated as dark numbers. The cloud top pressures derived from the window channel are indicated as white numbers.

only below 40° latitude. Parallax measurements were restricted to cirrus clouds without underlying cloud layers. The lower cloud layers sometimes confuse the parallax measurements because they are visible through the cirrus clouds. The parallax measurements were made west of the thick demarcation line on Fig. 4. There appeared to be lower cumulus below the cirrus east of the line. Most of the southwestern United States and Mexico had light cirrus without underlying clouds during the parallax measurements (see Fig. 5).

Parallax measurements were difficult to make on some cirrus clouds because their appearance was milky with poorly defined shapes and edges. The brightness of the cirrus also varied between the two satellites (as seen in Fig. 4); the cirrus west of the demarcation line appear brighter on the GOES-West image than the GOES-East image. The sun was positioned nearly directly over the GOES-East satellite at 75°W long during that time. The east satellite was looking at nearly direct backscatter while the west was looking at sunlight scattered approximately 90 deg.

Lines of cirrus were readily identified in both satellite images. Several parallax measurements were possible on each line; however, the altitude determinations exhibited some spread because unique features were difficult to identify. The diffuse character of the cirrus clouds made identification of targets for parallax measurements impossible within a single VAS FOV. Therefore, the average altitude for all cloud features inside a 100 km × 100 km area, where parallax measurements were made, was recorded as the "true" height. This averaging may not truly reflect the cloud top structure, but provides a means of comparison. The VAS CO_2 data were taken approximately 15 min after the visible stereo. The comparison of over one hundred VAS CO_2 to stereo parallax measurements is shown by the filled circles in Fig. 3. The variability of the VAS CO_2 heights is shown; the variability of the stereo heights is not shown but was found to be around 100 mb. The VAS generally underestimated cloud top height for high clouds above 400 mb; below 400 mb the VAS overestimated the cloud top heights. The average bias of VAS minus stereo observations was 25 mb.

d. Cirrus detection limits

Cirrus clouds are often very thin and difficult to detect with satellite or ground based sensors. Some cirrus are nearly invisible. Thinner cirrus have little effect on outgoing infrared radiation and thus are often difficult to distinguish from clear areas in the satellite infrared window imagery.

To determine the VAS CO_2 capability to detect thin cirrus, the cirrus clouds in the GOES imagery from 23 February 1988 were examined. The western United States had few clouds on this day, and most of those were upper-level cirrus (Fig. 4) with lower-level cloud forms nearly absent over land.

The VAS CO_2 technique demands that at least two CO_2 channels detect a cloud. It can err when the effect of the cloud on the radiance measured by the satellite is small. Since the CO_2 technique uses the ratio of the deviations of cloudy and clear radiances for two spectral channels, a very thin cloud can cause the ratio to be ill defined. In thin cirrus, the cloudy FOV radiance is nearly the same as the clear FOV radiance and therefore within the noise level of the sensor. As explained earlier, when this produces an unrealistic ratio, the window channel height is assigned.

In areas where low clouds cannot be seen on Figs. 4 and 5, all cloud reports from the VAS CO_2 technique should have been cirrus. This includes the land areas of Mexico and the southwestern United States. The black numbers in Figs. 4 and 5 are cirrus heights correctly determined by the VAS CO_2 technique. The white numbers (over land) indicate where high clouds were mistaken for low clouds, because the CO_2 ratio was indeterminate and the window channel height was

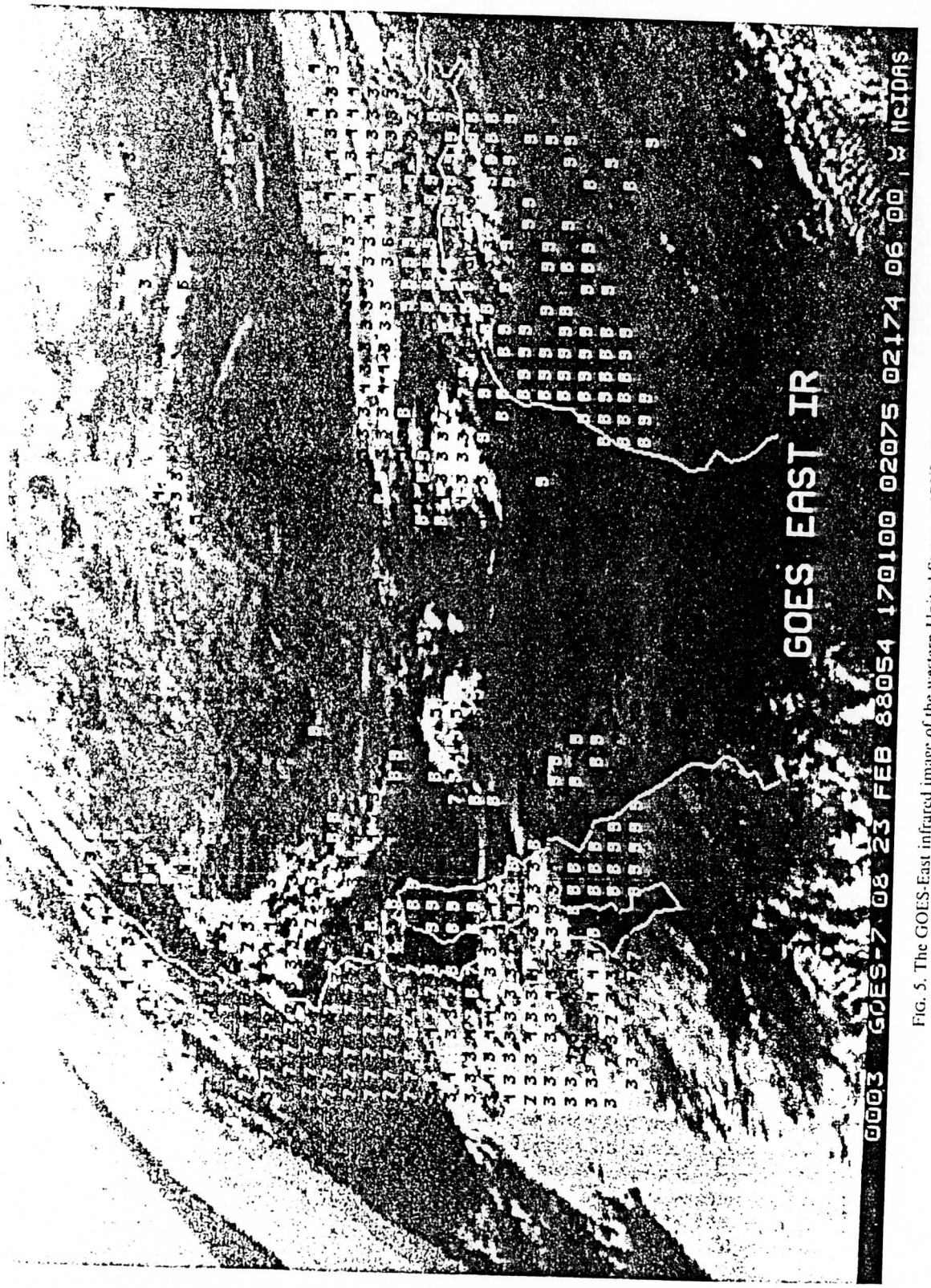

FIG. 5. The GOES-East infrared image of the western United States at 1701 UTC 23 February 1988. Cloud top pressures (mb 100^{-1}) derived from the VAS CO_2 technique are indicated.

used. A count of these reports reveals the failure rate of finding transmissive cirrus.

West of the demarcation line in Texas, 41 cirrus reports and 9 incorrect low opaque cloud reports were found. There were an additional 57 clear sky reports. This implies that the CO_2 technique missed 18% of the cirrus in this area; the cirrus coverage determined to be 38% of all reports should have been 47%. Across the western United States, a similar error rate was found; however, the total cirrus coverage percentage was less affected because more clear sky reports were averaged into the statistics. Cirrus clouds, west from 90°W longitude to the Pacific coast and north from 24°N to 40°N latitude, were reported 20% of the time by the VAS CO_2 technique. The actual percentage of cirrus cover, after corrections, was 25% of the total area. This implies that the cirrus may be underestimated by about 5% in our statistics. We will discuss this further in section 4.

Estimates were also made of the emissivity of the cirrus clouds that were missed. Assuming that the cirrus missed in Texas were of the same altitude as most of the neighboring cirrus at 300 mb, the 300 mb temperature at the location of each cloud report was used in Eq. 2 to calculate an effective emissivity for each of the missed cirrus. The result was an average effective emissivity of 10% for the nine cirrus cloud mistakes in Texas. There were nine other correct cirrus reports in Texas that also had effective emissivities of 7 to 12%. Thus, approximately half of the cirrus with effective emissivities around the 10% level were correctly detected.

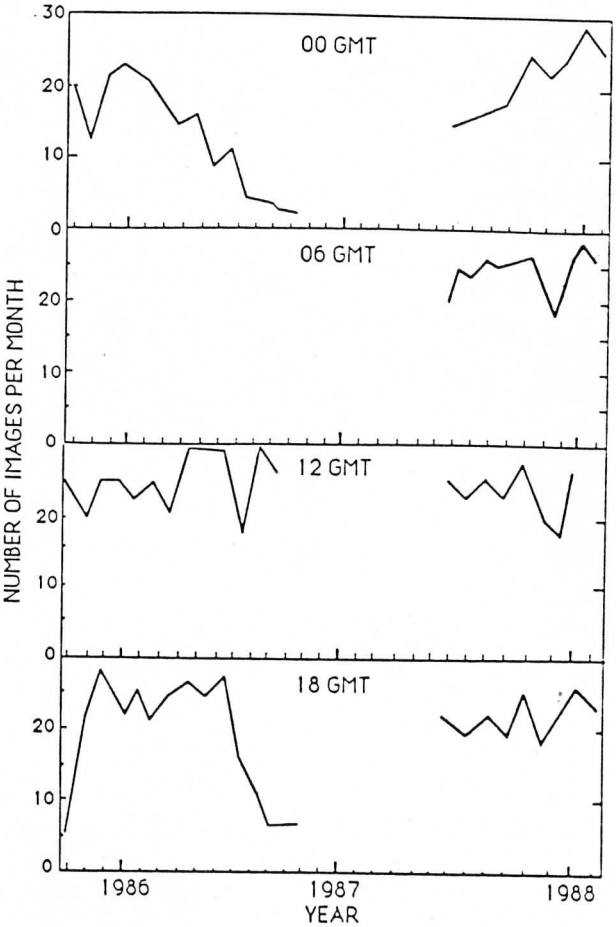

FIG. 6. The number of VAS images processed for each 6 h time period centered on 0000, 0600, 1200, and 1800 UTC between October 1985 and February 1988.

4. Mean statistics

The number of images processed during each quarter of the day is shown in Fig. 6. The VAS data were initially available from 0800 until 0100 UTC. Starting in October 1985, data were processed twice per day at 1000 and 2000 UTC. In December 1985, coverage was increased to three times per day; 0000, 1200, and 1800 UTC. The VAS sensor was not operated during the night so the 0600 UTC calculations could not be made. The VAS operation was reduced from 0800 to 1700 UTC in September 1986 to accommodate testing of a new ground processing system. A few special observations were made after 1700 UTC during FIRE. The VAS sounding data became unavailable in November 1986 when the new ground processing system was incorporated. The processing of cloud information restarted in June 1987 when VAS coverage became continuous 24 h day^{-1} (thus making 0600 UTC data available also).

A statistical summary of all the cloud observations made from October 1985 through February 1988 is shown in Table 1. This covers the area from 27° to 51°N lat and 60° to 140°W long. Over 6.6 million observations were processed. The cloud top pressure determinations were subdivided into ten vertical levels from 100 to 1000 mb in each row of Table 1. High clouds above 400 mb comprised 24% of the observations. Twenty-nine percent of the observations were of clouds between 400 and 800 mb. Low clouds below 800 mb were found 17% of the time. Clear sky conditions, labeled as 1000 mb, were found 30% of the time. This is summarized in Fig. 7.

The effective cloud emissivities were subdivided into five intervals shown in each column of Table 1. The right column contains the opaque or near-opaque cloud observations. Effective emissivity observations greater than 0.95 are considered to be opaque clouds, since the cloud top height derived from Eq. 1 is very close to the height derived from the window channel by itself. The other four columns separate the cloud height reports by effective emissivities ranging from the thin low emissivity clouds on the left to the thick high emissivity clouds on the right. Most cloud heights below 700 mb were determined from the infrared window channel, and thus were assumed to have an effective

TABLE 1. Cloud statistics (%) for the United States 27° to 51°N and 60° to 140°W for October 1985–February 1988.

Level (mb)	Effective emissivity				
	0.0–0.2	0.2–0.4	0.4–0.6	0.6–0.95	0.95–1.0
100–199	0	0	0	0	0
200–299	2	3	2	2	2
300–399	1	3	3	3	3
400–499	0	1	2	2	2
500–599	0	0	1	1	2
600–699	0	0	0	0	6
700–799	0	0	0	0	12
800–899	0	0	0	0	12
900–999	0	0	0	0	5
1000 (clear)	30	0	0	0	0
Total	33	7	8	8	44
	30% clear		26% cirrus		44% cloudy

emissivity of 1. This prevents the misinterpretation of low broken cloud as cirrus.

Cirrus clouds were defined as observations with effective emissivities less than 0.95. Twenty-six percent of our observations fell into this category. They were found from 200 to 600 mb. Clouds opaque to infrared radiation with effective emissivities greater than 0.95 (right column) were found 44% of the time. The remaining observations—clear sky noted at 1000 mb—were found 30% of the time. Thus, 70% of our satellite observations over North America for the past 2 yr recorded clouds.

These VAS statistics have been compared to a previous cloud climatology of Warren et al. (1986), which is an 11-yr compilation of cloud cover statistics from the manual land-based weather observations reported in the WMO synoptic code and archived by the Fleet Numerical Oceanography Center in Monterey, California. The Warren study reported a global mean total cloud cover of 52%, with 82% of the observations containing some cloud coverage and 18% being completely clear sky, free of any clouds. The differences between this VAS satellite study and the Warren ground observed climatology probably came from three causes. 1) The Warren study is global; this VAS study is only over North America. 2) The Warren study factors in the fractional coverage of clouds in the manual reports; our VAS study does not estimate the fractional coverage of the clouds inside each satellite FOV. 3) Ground observations usually see more clouds; FOVs with small partial coverage or very thin clouds are missed and not identified as clouds in our satellite analysis. Thus, the ground based reports show more total observations of cloud (82%) than the VAS (70%), but when correction for fractional sky coverage are made, the Warren study derives a smaller average cloud coverage (52%).

The semitransparent cirrus were observed mostly between 200 and 350 mb, just below the tropopause. The emissivities of the semitransparent cirrus were distributed over a wide range; three of the emissivity columns in Table 1 have nearly the same percentage of observations. Seven percent were found with emissivities from 0.2 to 0.4, 8% from 0.4 to 0.6, and 8% from 0.6 to 0.95 emissivity. The low emissivity column (0.0–0.2) contains 3% of the cloud observations. The 1000 mb observations were identified as transparent clear sky. In section 3, we noted that up to 5% of the opaque cloud reports were possibly cirrus that had been incorrectly classified. These misclassifications occurred around 0.10 emissivity. Therefore, the low emissivity column (0.0–0.2) should be corrected to have about 8% of the cloud observations based on this error study (the extra 5% coming from the opaque cloud column on the right). After this adjustment, we conclude that the cirrus are nearly uniformly distributed across all levels of emissivity.

5. Geographical coverage and seasonal changes

The seasonal and geographical distribution of VAS observations for 2 yr covering 27° to 51°N lat and 60° to 140°W long is summarized in Fig. 8. Cloud cover was divided into two types: 1) clouds opaque to terrestrial radiation with effective emissivities greater than 0.95, and 2) semitransparent cirrus with effective emis-

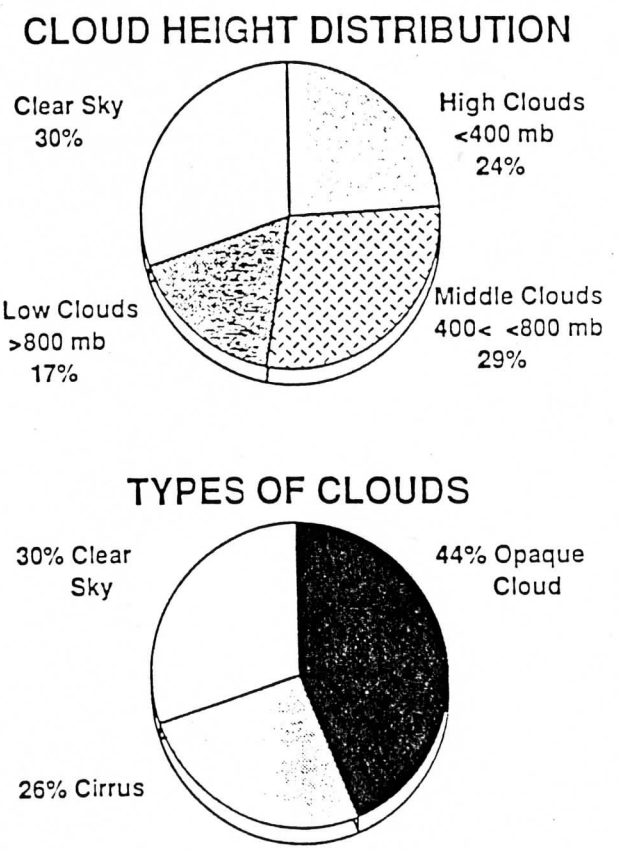

FIG. 7. Distribution of all GOES/VAS observations by cloud height and type of cloud or clear sky from October 1985 through February 1988.

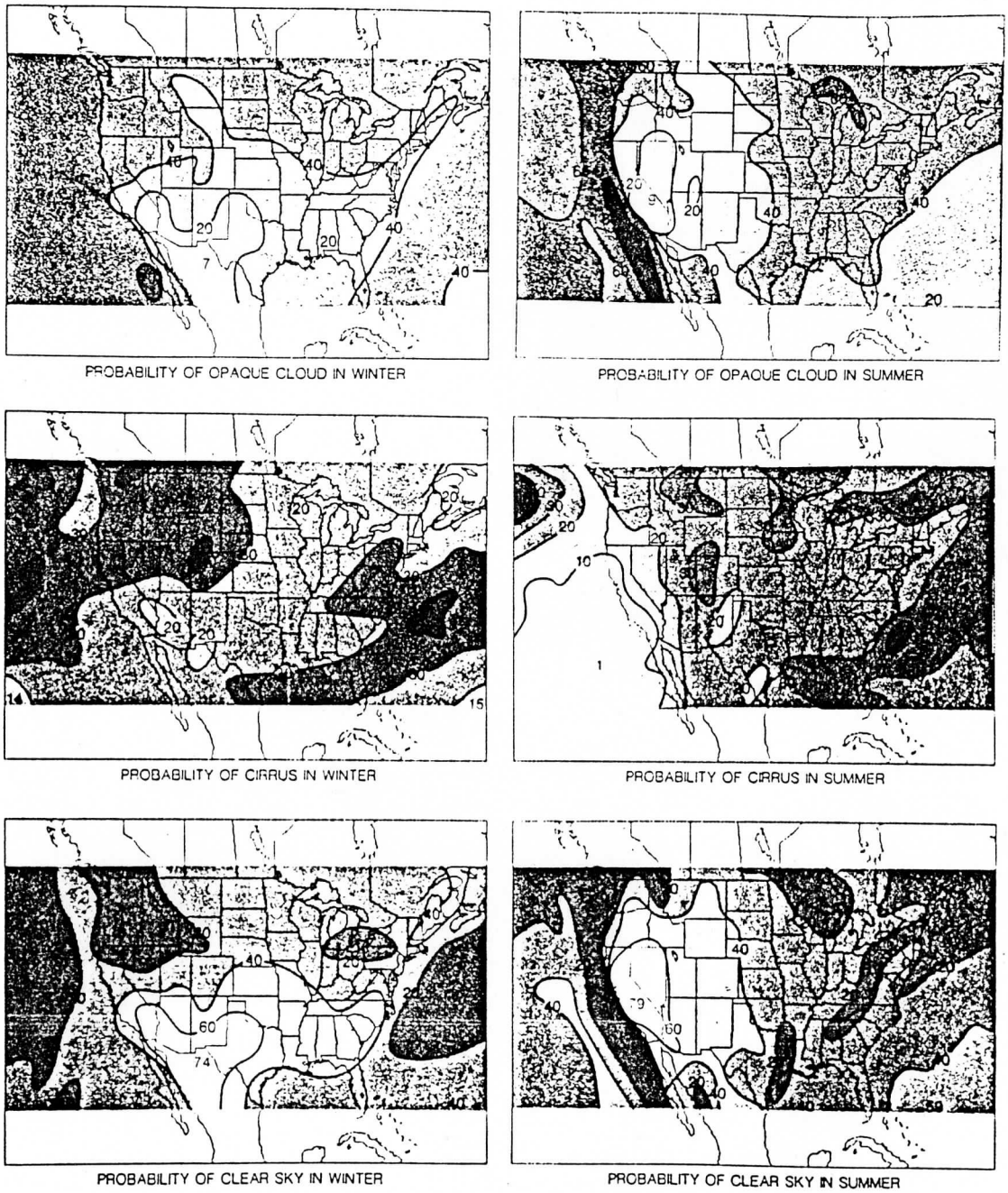

FIG. 8. The probability of VAS cloud observations being opaque cloud, semitransparent cirrus, or clear sky in summer (June–August) or winter (December–February) based on 2 yr of data.

sivities less than 0.95. All VAS observations were classified as opaque cloud, cirrus, or clear sky.

There were two winter and two summer seasons included in these data. The winters were December 1985–January 1986, and December 1987–January 1988. The VAS data were not available during the mild winter of December 1986–January 1987 because of the reconfiguration of the VAS ground processing system. The two summers were June–August 1986 and June–August 1987.

The geographical distribution of opaque cloud cover varied greatly across the United States and into the Pacific Ocean. The probability of opaque cloud cover was 20% to 40% over most of the country. The sunbelt of the desert southwest had far lower probabilities for clouds. The sunbelt moved from southwestern United States and Mexico in the winter, to Nevada and California in the summer. This seasonal shift reflects the growth of cloud cover over the desert southwest from cumulus convection clouds during the summer. A very

similar seasonal change was found by Warren et al. (1986).

Over the oceans, large seasonal changes in cloud cover also were found. The cloud cover increased along the California coast in the summer due to the presence of low-level marine stratus clouds. This study may be overestimating their probability because the coarse resolution of the VAS sensor (7 km) washed out small clear areas. Also, since the marine stratus often have nearly the same cloud top temperature as the underlying ocean surface, some of the clear areas are probably misclassified as being cloudy. However, the surface temperatures used in the VAS study do reflect seasonal changes, so the seasonal changes in probability of marine stratus are realistic even though the numbers shown for each season may be too high. Hahn et al. (1982), in their analysis of ship reports, also found some increase in cloud cover during the summer, but their seasonal change was small compared to these data.

In the western Atlantic, a decrease in opaque cloud occurrence in the summer was found. This decrease probably came from the northward movement of the subtropical high pressure system in the summer. Hahn et al. (1982) found a decrease in stratus clouds in the summer in this area, but they also noted an increase in cumulus clouds.

The clear sky observations show nearly the same geographical distribution and seasonal changes as the opaque cloud observations. The seasonal change in the sunbelt is similar to the opaque cloud change and in agreement with the climatology of Warren et al. (1986). The lower probability of clear sky along the California coast in summer also indicates the increase in marine stratus cloud cover. The probability of clear sky in the summer from VAS agrees quite well with the HIRS/MSU cloud summary over North America for June 1979 found in Susskind et al. (1987).

The semitransparent cirrus also had seasonal changes. However, their changes were smaller than the opaque cloud category (note that the contour interval in the cirrus panel is 10% whereas it is 20% in the clear and opaque panels). Most of the continental United States had 20%–35% occurrence of cirrus in both winter and summer. More frequent cirrus observations were found in the Atlantic and northern Pacific oceans. Seasonal changes in cirrus were small over the continent. The largest seasonal change was found in the eastern Pacific, where cirrus cloud occurrence decreased from 30% in the winter to less than 10% in the summer. The frequency of cirrus observations decreased in the area where opaque marine stratus observations increased. A similar but smaller decrease in cirrus was found in the ship data studies by Hahn et al. (1982).

The frequency of both opaque clouds and cirrus over the whole area decreased by roughly five percentage points in the summer (see Table 2). Cirrus dropped from a 30% frequency in the winter to 25% in the summer, and opaque cloud dropped from 46% in the winter to 40% in the summer. Clear sky observations correspondingly increased from 24% in the winter to 35% in the summer. Warren et al. (1986) also found a very similar seasonal change over North America, reporting a decrease of 9% in average total cloud from winter to summer.

TABLE 2. Winter to summer seasonal changes in mean cloud cover for 27°–51°N, 60°–140°W.

Type	Winter (%)	Summer (%)
Cirrus clouds	30	25
Opaque clouds	46	40
Clear skies	24	35

The mean height of semitransparent cirrus observations also changed between the winter and summer seasons. All cirrus observations with effective emissivities less than 0.95 had an average height of 350 mb in the winter which rose to 325 mb in the summer. This change most likely represents the lifting of the troposphere and the addition of cumulonimbus convection in the summer.

Figure 9 shows a comparison for the month of October 1987 of the VAS geographical cloud analysis with the outgoing longwave radiation (OLR) analysis made by NOAA/NESDIS from the polar orbiting NOAA satellite (World Climate Data Programme 1987). The OLR depicts the average upwelling flux of infrared radiation, which is largest where predominantly clear skies occurred and decreases in the cloudier areas. A minimum in OLR was found in the Great Lakes area also, where a minimum in the frequency of clear sky conditions was found in the VAS data. The OLR increased in the southern states, with a maximum along the Gulf of Mexico coast from Texas to Florida. Similar changes with latitude were found in the VAS data, but the maximum extended to the Panhandle region of Texas. Other agreement can be seen along the east coast from North Carolina to Maine where a local maximum in clear skies found by VAS corresponded to a local ridge in the OLR field. However, the OLR does not show a minimum along the California coast, where the VAS data show more cloudiness, because the marine stratus clouds are warm and nearly the same temperature as the ocean.

7. Diurnal changes

Moderate diurnal changes were found in the past 2 yr. Semitransparent cirrus had smaller changes on the average. The effects of convection along the Gulf Coast in the summer produced a noticeable diurnal pattern (Fig. 10). Opaque cloud occurrences were lowest at 0000 UTC (1800 LST) and highest at 1800 UTC (local

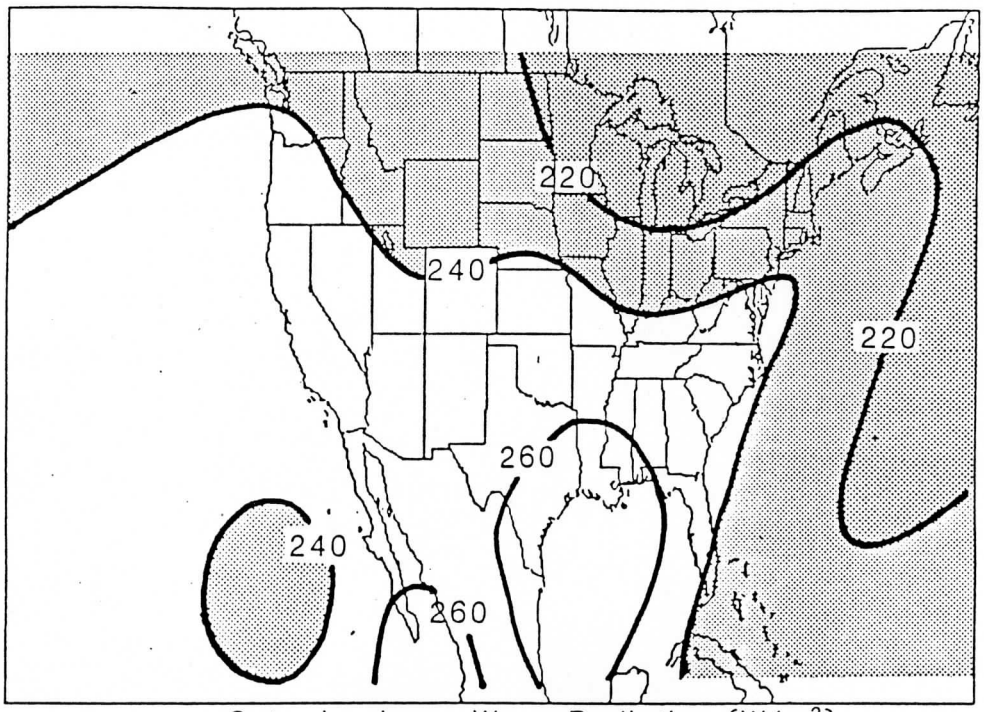

Outgoing Long Wave Radiation (W/m²)

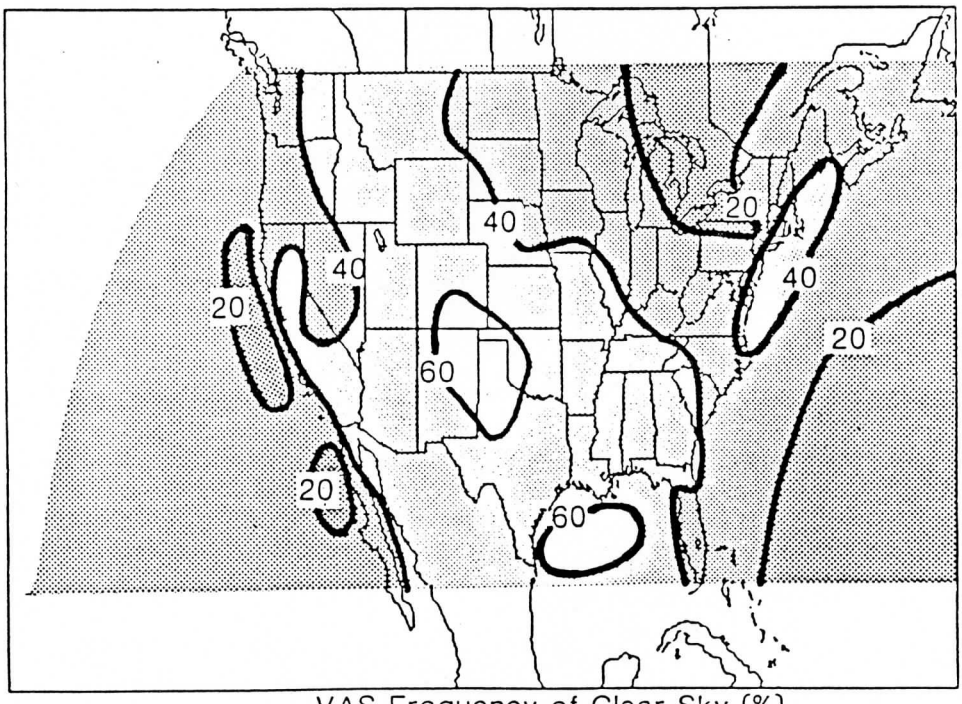

VAS Frequency of Clear Sky (%)

FIG. 9. The average outgoing longwave radiation (OLR) for October 1987 measured by the NOAA polar orbiter in W m^{-2} (upper panel). The frequency of clear sky measured by GOES/VAS for the same months is shown in the lower panel.

noon). Cirrus occurrences were lowest in the morning [1200 UTC; (0600 LST)] and increased to a maximum at the end of the day [0000 UTC (1800 LST)]. This shows a pattern of cumulus clouds developing during the day leaving cirrus behind when they finish their life cycles at the end of the day.

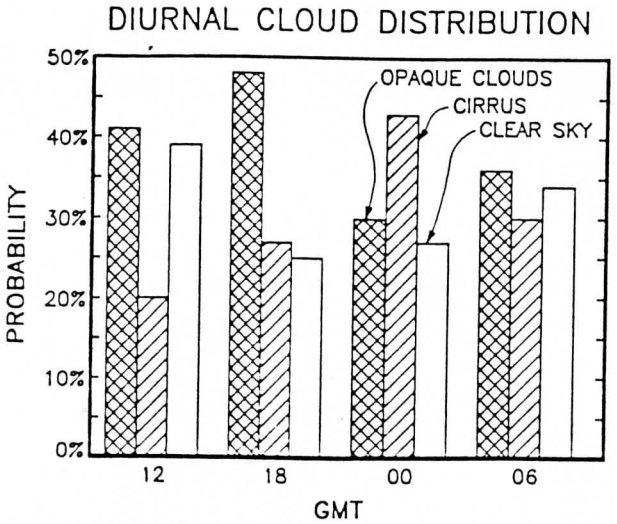

FIG. 10. The diurnal change in opaque and cirrus cloud observations in southern Mississippi during the summer months (June, July, and August) in 1986 and 1987.

8. Discussion and conclusions

This is a report of an ongoing study of cloud cover. Earlier results have been reported by the authors (Wylie and Menzel 1987, 1988). Through intercomparisons with radiosonde, lidar, and stereo parallax measurements, the VAS CO_2-derived cloud top height and emissivity assignments have been found to be reliable within 50 mb and 20% respectively for most cloud types; however, broken clouds and stratocumulus at low levels remain elusive. The VAS cloud cover statistics for 2 yr have been presented. We have found reasonably good agreement with the manual weather observations analyzed by Warren et al. (1986) and the satellite analysis of 1 month made by Susskind et al. (1987). There are differences in the amount of cloud cover, but the geographical patterns and seasonal changes are similar. There are also similarities in the VAS cloud analysis for October 1987 and the OLR derived from polar orbiter data. However, we did not agree as well with the ship observations in the eastern Pacific, analyzed by Hahn et al. (1982) in the amount and seasonal changes of opaque cloud cover. Definitive conclusions on these cloud cover statistics must wait until more years of data and more analyses are compiled. However, some interesting trends are emerging from the data:

- The principal finding is the high incidence of transmissive cirrus clouds (20% to 30% probability of occurrence over North America). Cirrus clouds have been given little attention in the past because they do not yield precipitation or damaging weather, but they have a large impact on atmospheric radiation. It is the intent of the International Satellite Cloud Climatology Project (ISCCP) to determine the effect of cirrus and opaque clouds on the earth's radiation budget; to date, their estimates of cirrus are restricted to visible and infrared window data (Schiffer and Rossow 1983). This work suggests that multispectral techniques would be beneficial.
- The VAS cloud statistics indicate that transmissive cirrus clouds have smaller geographical and seasonal variances than opaque clouds over the continental United States. A large seasonal change of cirrus was found over the eastern Pacific Ocean. But in other areas, the cirrus occurrences changed far less between seasons than the opaque clouds; i.e., a considerable percentage of cirrus is present all the time.
- The emissivities of transparent cirrus clouds were found to be uniformly distributed between 0.00 and 0.95. Fewer cirrus were initially found below 0.20 emissivity, but an error analysis indicated that one-half of these very thin cirrus clouds had been misidentified. After correcting for this error, nearly as many cirrus with emissivities less than 0.20 were found as in the other emissivity ranges.

These cloud statistics are continuously being compiled. In the future, we will report more extensively on diurnal changes in cloud data. Studies of what atmospheric dynamical features are associated with cirrus are also underway.

Acknowledgments. The authors gratefully acknowledge the efforts of William Smith, Jr. and Peter Grimm who performed some of the data processing. This work was supported by Grants N00014-85-K-0581 and N00014-87-K-0436 of the Office of Naval Research and NAG1-553 from the National Aeronautics and Space Administration.

REFERENCES

Bryson, W. R., 1978: Cloud height determinations from geosynchronous satellite images. Ph.D. thesis, University of Wisconsin–Madison, Univ. Microfilms Inter. 7817097, 91 pp.

Chahine, M. T., 1974: Remote sounding of cloudy atmospheres. I: The single cloud layer. *J. Atmos. Sci.*, **31**, 233–243.

Cox, S. K., D. S. McDougal, D. A. Randall and R. A. Schiffer, 1987: FIRE—The first ISCCP Regional Experiment. *Bull. Amer. Meteor. Soc.*, **68**, 114–118.

Eyre, J. R., and W. P. Menzel, 1988: Retrieval of cloud parameters from satellite sounder data: A simulation study. Accepted by *J. Appl. Meteor.*

Hahn, C. J., S. G. Warren, J. London, R. M. Chervin and R. Jenne, 1982: Atlas of simultaneous occurrence of different cloud types over the ocean. NCAR Tech. Note NCAR/TN-201+STR, [Available from National Center for Atmospheric Research, Boulder, CO 80302, NTIS PB83-152074.] 212 pp.

Hasler, A. F., 1981: Stereographic observations from geosynchronous satellites: An important new tool for the atmospheric sciences. *Bull. Amer. Meteor. Soc.*, **62**, 194–212.

Menzel, W. P., W. L. Smith and T. R. Stewart, 1983: Improved cloud motion wind vector and altitude assignment using VAS. *J. Climate Appl. Meteor.*, **22**, 377–384.

——, D. P. Wylie and A. H.-L. Huang, 1986: Cloud top pressures and amounts using HIRS CO_2 channel radiances. *Tech. Proc., Third Int. TOVS Study Conf.*, Madison, 173–185.

Schiffer, R. A., and W. B. Rossow, 1983: The International Cloud

Climatology Project (ISCCP): The first project of the World Climate Research Programme. *Bull. Amer. Meteor. Soc.*, **64**, 779–784.

Smith, W. L., and C. M. R. Platt, 1978: Intercomparison of radiosonde, ground based laser, and satellite deduced cloud heights. *J. Appl. Meteor.*, **17**, 1796–1802.

——, H. M. Woolf, P. G. Abel, C. M. Hayden, M. Chalfant and N. Grody, 1974: Nimbus 5 sounder data processing system Part I: Measurement characteristics and data reduction procedures. NOAA Tech. Memo., NESS 57, 99 pp.

Starr, D. O., 1987: A cirrus cloud experiment: Intensive field observations planned for FIRE. *Bull. Amer. Meteor. Soc.*, **68**, 119–124.

Susskind, J., D. Reuter and M. T. Chahine, 1987: Cloud fields retrieved from analysis of HIRS/MSU sounding data. *J. Geophys. Res.*, **92**, 4035–4050.

Szejwach, G., 1982: Determination of semitransparent cirrus cloud temperatures from infrared radiances: Application to Meteosat. *J. Appl. Meteor.*, **21**, 384–393.

Warren, S. G., C. J. Hahn, J. London, R. M. Chervin and R. L. Jenne, 1986: Global distribution of total cloud cover and cloud type amounts over land. NCAR Tech. Note NCAR/TN-273+STR. [Available from National Center for Atmospheric Research, Boulder, CO 80307, NTIS DE87006903/XAB.] 228 pp.

Wielicki, B. A., and J. A. Coakley, 1981: Cloud Retrieval using infrared sounder data: Error analysis. *J. Appl. Meteor.*, **20**, 157–169.

World Climate Data Programme, 1987: Climate system monitoring (CSM). Monthly bull. 1987-11, WMO Secretariat, Geneva 20, Switzerland, 33 pp.

Wylie, D. P., and W. P. Menzel, 1987: Cloud statistics using VAS. *Adv. Space Res.*, **7**, 147–154.

——, and ——, 1988: Cloud cover statistics using VAS. *SPIE*, **874**, 253–259.

Reprinted from JOURNAL OF APPLIED METEOROLOGY, Vol. 27, No. 6, June 1988
American Meteorological Society

GOES-VAS Simultaneous Temperature–Moisture Retrieval Algorithm

CHRISTOPHER M. HAYDEN

NOAA/NESDIS Systems Design and Applications Branch, Madison, Wisconsin

(Manuscript received 10 January 1987, in final form 20 November 1987)

ABSTRACT

Vertical soundings of temperature and moisture derived from the GOES VISSR Atmospheric Sounder (VAS) measurements have been produced operationally since summer 1987 at the VAS Data Utilization Center (VDUC). The algorithm which was developed for the VDUC is described here in detail. Tunable features are identified, and their sensitivities are shown. The algorithm is used to process a case study for 6 March 1982 to examine its capability in a rapidly evolving weather pattern. Weaknesses are exposed, in particular the bias errors in the retrievals and the dependence on first guesses, but strengths are also evident, namely, the capacity to refine gradients and patterns in a manner which improves the first guesses.

1. Introduction

The VISSR Atmospheric Sounder (VAS) has been carried on the Geostationary Operational Environmental Satellites (GOES) since September 1980. The instrument has been operated in a research and assessment mode prior to operational implementation which began in Spring 1987. The VAS was designed to provide frequent observations of the temperature and moisture structure of the atmosphere on the subsynoptic scale, and has been evaluated in a semioperational schedule since 1984 in support of three National Weather Service (NWS) Centers: the National Severe Storm Forecast Center (NSSL) at Kansas City, the National Hurricane Center (NHC) at Miami, and the National Meteorological Center (NMC) at Washington. Operational VAS processing capability is part of the National Center upgrade beginning with the establishment of the VAS Data Utilization Center (VDUC) at the World Weather Building during the Summer of 1986. The VDUC will provide multispectral imagery from the VAS as image loops as well as produce VAS temperature–moisture retrievals, derived product imagery (Smith et al. 1985a), and wind estimates from satellite-observed atmospheric motion. The World Weather Building VDUC will be responsible for operational VAS processing support for all three centers prior to VDUC installation at Kansas City and Miami.

The main purpose of this article is to describe the VDUC retrieval algorithm in considerable detail, emphasizing aspects which are "tunable" or situation dependent. The retrievals are examined both as individual profiles and in terms of a three-dimensional representation of the atmosphere. A second purpose is to give a case study example of VAS retrievals used in 3-h updating. Those readers not concerned with technical details might read only the sections dealing with the case study. At either level, the intention is to familiarize the reader with the generic capability of the system to guide his interpretation of VAS data.

Section 2 describes the physics and procedures used in producing VAS temperature and moisture profiles. Section 3 describes the dataset used in the following sections. The following two sections examine the two basic problems involved in a physical retrieval algorithm: section 4 deals with the "forward problem" of calculating brightness temperature given profiles of temperature and moisture and surface boundary conditions; and section 5 deals with the "inverse problem" of calculating temperature and moisture corrections to a first guess, based on the difference between observed and calculated brightness temperatures. Section 6 describes the result of the algorithm applied as a case study. Finally, section 7 attempts to summarize the findings and to interpret the utility of the VAS as a source of temperature and moisture profiles.

2. VAS simultaneous retrieval algorithm

a. Temperature, moisture, and skin temperature retrieval

The simultaneous retrieval algorithm used for the VAS is basically that described in Smith et al. (1985b). The radiative transfer equation is linearized to give

$$\delta T^* = \int_0^{P_s} \delta U \left(\frac{\partial T}{\partial p}\right)\left(\frac{\partial \tau}{\partial U}\right)\frac{(\partial B/\partial T)}{\partial B/\partial T^*)}\,dp - \int_0^{P_s} \delta T \frac{\partial \tau}{\partial p} \times \frac{(\partial B/\partial T)}{(\partial B/\partial T^*)}\,dp + \delta T_s \frac{(\partial B_s/\partial T_s)}{(\partial B/\partial T^*)}\,\epsilon\tau_s, \quad (1)$$

Corresponding author address: Dr. Christopher M. Hayden, NOAA/NESDIS, 1225 West Dayton St., Madison, WI 53706.

where T^* is the brightness temperature; U precipitable water; T temperature; τ transmittance; P pressure; B the Planck radiance; and subscript s refers to the lower radiating surface with emissivity ϵ. The delta indicates an incremental difference between the true value and a first estimate. The incremental brightness temperature (observation minus calculated) is determined by three contributions: the integrated contribution from the incremental variable atmospheric constituent (water vapor); the integrated contribution from the incremental atmospheric temperature; and the contribution from the incremental skin temperature. The reflected atmospheric contribution associated with an emissivity less than unity is not explicitly treated since it is small and can be approximated by overestimating the true surface emissivity. A discussion of this term is included in Susskind et al. (1984). Note that additional angle and frequency dependence are not shown in the notation used for (1), as these have been eliminated for simplicity. There are as many Eqs. (1) as there are VAS channels (frequencies) for a given field-of-view (zenith angle), and it is this system (augmented by additional relationships to be described below) which is solved to yield a temperature and moisture profile at the given location.

To solve the set of equations given by (1) the perturbation profiles are represented in terms of $M + 1$ pressure-dependent basis functions, $\phi(p)$:

$$\delta T_s = \alpha_0 \phi_0 \tag{2}$$

$$\delta U(P) = \sum_{i=1}^{N} \alpha_i \int_0^P q(p)\phi_i(p)dp \tag{3}$$

$$\delta T(p) = -\sum_{i=N+1}^{M} \alpha_i \phi_i(p) \tag{4}$$

where (3) is derived from the definition

$$\delta q(p) = g \sum_{i=1}^{N} \alpha_i q(p)\phi_i(p); \quad \delta U(p) = \frac{1}{g}\int_0^p \delta q(p)dp. \tag{5}$$

The water vapor mixing ratio is given by $q(p)$, and g is the acceleration of gravity. The pressure-dependent basis functions ϕ which are used with VAS are profiles of the vertical derivative of the transmittance ($d\tau/d\ln p$) for several of the channels. (Examples are given in section 5.) This choice of functions is just one of many reasonable options; for example, empirical orthogonal function might be used to include statistical information, and this approach was investigated before selecting the current set (Smith et al. 1985b). The latter choice has the intuitively attractive features of representing the instrument characteristics and also local variations in the scene (through the transmittance profiles which are computed from the first estimate). The size of M is arbitrary, but no larger than the total number of measurements. In VDUC processing, for (3), the water vapor sensitive channels 7, 9, and 10 are used (i.e., $N = 3$); and for (4), channels 2, 3, 4, 5 and 7 are used. The total number of functions is limited to reflect the limited independence of the measurements and to increase computational efficiency.

Substituting (2–4) into (1) yields for each spectral radiance observation, δT_j^*, for a set of K channels:

$$\delta T_j^* = \sum_{i=0}^{M} \alpha_i \Phi_{ij}, \quad j = 1, 2, \cdots, K \tag{6}$$

where

$$\left.\begin{aligned} \Phi_{0,j} &= \frac{\partial B_j/\partial T_s}{\partial B_j/\partial T_j^*}\,\epsilon\tau_{s,j} \\ \Phi_{i,j} &= \int_0^{P_s}\left[\int_0^P q(p)\phi_i dp\right]\left[\frac{\partial T}{\partial p}\frac{\partial \tau_j}{\partial U}\frac{\partial B_j/\partial T}{\partial B_j/\partial T_j^*}\right]dp, \\ &\qquad\qquad 1 \leqq i \leqq N \\ \Phi_{i,j} &= \int_0^{P_s}\phi_i\left[\frac{\partial \tau_j}{\partial p}\frac{\partial B_j/\partial T}{\partial B_j/\partial T_j^*}\right]dp, \quad N < i \leqq M \end{aligned}\right\}. \tag{7}$$

The three sets given in (7) correspond to surface, water vapor, and temperature contributions, respectively. The atmospheric quantities which are needed to define the Φ matrix are calculated from first guesses of surface temperature and the atmospheric temperature and moisture profiles. Details are given below in the subsection 2d on Ancillary Data. The values of $q(p)$ in (7) are scaled by 10^{-3} in order to have all elements of the matrix $\mathbf{\Phi}$, approximately the same order of magnitude. Transmittances are determined using the techniques described by Weinreb et al. (1981). The analytic derivative of the Planck function with respect to temperature is used to evaluate terms involving this derivative. An estimate of $\partial\tau/\partial U$ is derived by creating 1) a second profile of precipitable water where the mixing ratio at each level is replaced by half of its first-guess value; 2) calculating a second transmittance profile; and 3) forming the derivative from the two estimates at each level. This may not be an optimum choice but is an economically viable approach to what can be a computationally expensive problem.

A first estimate of the surface skin temperature is obtained using a linear regression model of the "split window" (McMillin and Crosby 1984) operating with either the first two or all of the 11.2, 12.7, and 3.9 μ window channels. Use of the last channel is suppressed only if the cloud filtering (see below) suggests cloud contamination. The regression coefficients were empirically derived using measurements from GOES-4 collocated with ship observations of the sea surface temperature. Since the dependent sample consisted of only ocean temperatures, skin temperature estimates over either hot or cold land surfaces must be suspect. An error on the warm side is more damaging to the

ultimate estimate of temperature and moisture profiles because the change in radiance with temperature is more sensitive. For this reason, the skin temperature estimates provided by the model are trapped to be no greater than the 3.9 μ brightness temperature if they are greater than 300 K and also greater than the surface air temperature. Fortunately, an error in the initial estimate of the skin temperature is not catastrophic because the estimate is modified as part of the retrieval.

The surface emissivity is given a fixed value of 1.0 over water surfaces and 0.96 over land. The land/water discrimination is obtained from a topography file with latitude/longitude resolution of 10 min.

The set (2–4) with the radiative transfer contribution functions (1) include only the direct VAS measurements. There is, however, no reason to be restricted to satellite measurements alone. In the VAS processing done on VDUC, surface air estimates of temperature and mixing ratio are included as

$$q_0 - q(p_s) = g \sum_{i=1}^{N} \alpha_i q(p_s)\phi_i(p_s) \tag{8}$$

and

$$T_0 - T(p_s) = - \sum_{i=N+1}^{M} \alpha_i \phi_i(p_s).$$

Finally, in matrix form, (6) is written

$$t^* = \Phi\alpha \tag{9}$$

where t^* is a row vector of 12 elements (ten brightness temperature observation and two surface observation increments); α is a row vector of nine coefficients (one surface, three moisture and five temperature); and Φ is a matrix of dimension 12×9 given by (7). A least-squares solution of (9) gives

$$\alpha = (\Phi^T\Phi)^{-1}\Phi^T t^* \approx (\Phi^T\Phi + \gamma I)^{-1}\Phi^T t^*. \tag{10}$$

The γI term is included to stabilize the solution. Gamma (γ) is a conditioning constant and I is a diagonal unit matrix. There is one further modification to (9) (and therefore Eq. 10) which "weights" the influence of the observations according to their quality. These weights are determined from instrument noise characteristics and the number of observations averaged to form the "clear column" brightness temperature estimate:

$$E = \sigma_j/[(\partial B_j/\partial T)(SN)^{1/2}] \tag{11}$$

where σ_j is the single sample noise (Table 1). Here, S is the number of spins for the particular channel measurement, and N the number of spatial samples which are averaged prior to retrieval (these quantities are described further in subsection 2b). Both sides of (9), the elements of the vector $\mathbf{t}^*$ and each row element of Φ, are weighted by $1/E_j$. In the VDUC algorithm, the weights are trapped to be no smaller than 0.25 (0.50 for the window channels). Note that a very large weight is equivalent to insisting that the channel have no effect on changing the initial estimates of temperature and moisture. This has, in fact, been routinely done for channel 8—the 11.2 micrometer window—since the accuracy of the transmittance function for this channel is questionable.

The VDUC version of the algorithm contains an option of making two passes. Under this option, the α from the first pass are used to modify the initial estimates of temperature and moisture according to (2)–(4) and the updated versions are used to recompute the $\mathbf{\Phi}$ matrix (7) for a second pass. (The ϕ basis functions are not recomputed.) The solution (10) is sensitized by reducing the value of γ from 1.0 to 0.1 on the second pass. The philosophy behind the multiple pass is to improve the transmittance calculations contained in (7), which are dependent on the temperature and moisture profile estimates, with the results from the first pass. This improvement allows the measured radiances to be more precisely matched by reducing γ on the second pass. The necessity for a second pass depends on the quality of the first guess. Given an accurate first guess, the smaller γ can be used on the first pass and the second pass eliminated.

b. The VAS data

A VAS is composed of 12 channels as shown in Table 1. Measurements are taken across the earth's disk from west to east as the spacecraft spins. North to south coverage is obtained by stepping the instrument after one or a number of spins. For images (i.e., the familiar visible and infrared pictures obtained from GOES), only a single spin is required for each step. In the "sounding" mode, however, several spins may be used for a given channel in order to improve signal-to-noise in the composite measurement. An example of a "spin budget" is given in Table 1. In this example, 54 spins are proposed to obtain measurements from all of the 12 channels. It should be emphasized that this is an example. The number of spins must be weighed against the amount of time available for sounding (at 100 rpm) and the north–south coverage desired. For GOES, sounding is limited to approximately 10 min each half hour, and the coverage requested by the NWS has caused the spin budgets to be reduced considerably from that shown in Table 1. Signal-to-noise is recovered by horizontal averaging. To further save time, channel 11 is not used in the VDUC processing.

The VAS was designed to be operated at different spatial resolutions according to the choice of detector arrays. The horizontal resolutions of the large and small detectors are nominally 14 and 7 km, respectively, at nadir. In early processing, the 14 km data was used exclusively. After tests showed that the small detector offered significant cloud clearing advantages (Menzel et al. 1984), subsequent to August 1984 the 7 km resolution has been used for some of the cloud sensitive

TABLE 1. VAS instrument characteristics.

Spectral channel	Central wavelength (μm)	Central wavenumber (cm^{-1})	Weighting function peak (mb)	Absorbing constituent	Inflight single sample noise (mW m^{-2} sr^{-1} cm)	Typical spin budget*	Typical sounding radiance noise† (mW m^{-2} sr^{-1} cm)
1	14.71	679.95	40	CO_2	4.125	2	0.583
2	14.45	691.90	70	CO_2	2.525	4	0.253
3	14.23	702.89	150	CO_2	1.763	7	0.133
4	13.99	714.85	450	CO_2	1.488	7	0.112
5	13.31	751.37	950	CO_2	1.131	4	0.113
6	4.52	2214.35	850	CO_2	0.028	7	0.002
7	12.66	789.89	surface	H_2O	1.069	3	0.123
8	11.24	889.52	surface	window	0.119	1	0.024
9	7.25	1379.69	600	H_2O	1.225	9	0.082
10	6.73	1486.33	400	H_2O	0.306	2	0.043
11	4.44	2254.28	500	CO_2	0.026	7	0.002
12	3.94	2538.07	surface	window	0.007	1	0.001

* Number of spins sensed by the same detector with filter and mirror positions fixed.
† After averaging 25 samples in one sounding area.

channels. Unfortunately, since the same time versus coverage constraints apply regardless of the detector used, half of the sounding lines are not sampled in the small detector mode. Nevertheless, since 11 × 11 (small detector) fields-of-view are used to derive a sounding, an adequate sample is still achieved.

c. *The cloud problem*

Since channels 1 and 2 are not affected by cloud, their radiance estimates for a retrieval are simple averages of the contributing fields-of-view. Samples for the other channels are independently filtered to reduce cloud noise. The filters are accept/reject decisions intended to yield uniform samples. It should be understood that this processing is not intended to *eliminate* cloud effect but only to ensure uniform cloud conditions.

The presence of clouds may be detected either during the filtering or during the retrieval itself, and retrievals are processed for overcast (up to three quadrature pressure levels above the surface) as well as clear conditions. A preliminary clear versus cloudy decision is made based on an intercomparison of the warmest 11.2, 12.7, and 3.9 μ window values, and the surface air temperature estimated from an objective analysis of the surface reporting network. Cloud is assumed if any of the following three conditions are met: 1) the 3.9 measurement is significantly warmer (reflected sunlight or broken cloud) than the 11.2; 2) the 3.9 measurement is significantly colder than the 11.2 (nighttime stratus); or 3) the 11.2 measurement, adjusted for moisture attenuation by adding the difference between it and the 12.7 measurement, is significantly colder than the surface air temperature. "Significant" in the VDUC algorithm varies from 3 to 5 K. It should be added that measurements in the visible are not used in the VDUC processing because of the complexity involved in obtaining coincident measurements.

When the filtering indicates cloud, the pressure of the assumed overcast condition is determined by comparing an estimated skin temperature (see below) to the first guess temperature profile. The cloud level is assigned at the first level below the pressure level at which the temperature profile is colder. In some cases, this will result in a cloud level which is at the surface. In this event the sounding is reclassified as cloud-free, but the retrieval is still constrained to follow the "cloudy path" in the algorithm.

A preliminary estimate of clear conditions from the preset cloud filter can be overruled if the initial pass of the retrieval cools the first estimate of the skin temperature by more than a present amount (6 K in the VDUC software). Under this circumstance, the retrieval is reinitiated as an overcast sounding.

When a retrieval is processed as overcast, a number of changes are made to the "clear path". The basis functions are set to zero below the cloud level, and the forward calculation of brightness temperature (section 5) is integrated only down to the level of the cloud rather than to the surface. In essence, the retrieval is made above the cloud. To accommodate this in (8), the surface temperature and mixing ratio observations are replaced by values taken from the first-guess profiles at the cloud level. Also, the value of gamma is not reduced on the second pass. After the retrieval, the final estimates of temperature and mixing ratio below the cloud are formed by linearly interpolating between the cloud level values and the surface observations, retaining the shape of the first guesses.

The cloud processing described above is imperfect. Perhaps the greatest deficiency is that the cloudy soundings must necessarily be processed differently from the clear soundings. It will become apparent in section 5 that the information in VAS measurements for improving the first-guess profiles is marginal, and the vertical structure of the retrievals is quite sensitive to variations in the algorithm. Different paths for dif-

ferent cloud situations gives rise to fictitious horizontal gradients in the temperature or moisture at a given pressure level which may detract from the usefulness of the data. In the form of retrieved profiles, most of the cloudy soundings are suppressed by the automated quality control in the VDUC processing. However, another product of the VDUC is "images" of the lifted index and precipitable water, and for these the results from the cloud path are included to improve horizontal coverage. In these images (Smith et al. 1985a), inconsistencies are smoothed in both the horizontal and vertical (and in the more flagrant cases are obvious to the eye). As input to numerical models, however, the mix of retrieval types may be detrimental, and the overcast retrievals which survive the quality control should probably be eliminated.

d. Ancillary data

Since the VDUC algorithm is formulated in terms of residuals, it is necessary to provide first-guess information to calculate the first guess radiance (see section 4) and to define many of the terms in (7). As indicated by the limits of integration, information is needed from the surface to the top of the atmosphere. Surface temperature and moisture are obtained from objective analyses of the most recent data collected from the FAA surface network, the buoy network, and the 6-h ship data. In order to take advantage of known topography, the surface temperature data are extrapolated to and analyzed at mean sea level (MSL). A fixed lapse rate from the reported station elevation is used. For application in a retrieval, the MSL value is interpolated to the retrieval location and converted to a surface value using the same fixed lapse rate and an elevation obtained from the high resolution topography file. Surface moisture is obtained from an analysis of surface dewpoint depression. The objective analysis model is a recursive filter, successive approximation algorithm (Hayden and Purser 1986) operating on a pseudomercator projection with equal increments (1.2 deg) of latitude and longitude. The model uses a first guess derived from the source providing the first-guess profiles of temperature and moisture.

It will become clear from the case study described in section 6 that the VDUC retrievals are highly dependent on the first guess. The processing begins with the best guess available in order to maximize the accuracy of the final product. The most commonly used source is the regional (NGM) model forecast. (For Miami support, the global aviation model forecast (GAM) is used because of its greater horizontal coverage.) First-guess profiles are interpolated in time between the 12 and 24 h forecasts.

The first-guess forecasts are interpolated to the 40 pressure levels required in the retrieval quadrature (Table 2). Since the forecast models provide data only to 100 mb, NWS analyses of the stratosphere are used to provide information to 10 mb. Above this, temperatures are assigned using regression equations which operate on the stratospheric temperatures. Regression equations are available for an uppermost reported level of 10, 30 or 50 mb, and for three latitude zones (no seasonal separation). The coefficients are quadratically interpolated to exact latitudes when extending a profile. The VDUC algorithm will still operate when all the stratospheric analyses are missing. In this event, a temperature of 213 K is assigned at 50 mb, and a value at 70 mb is interpolated from the values at 100 and 50 mb.

Quadrature levels below 10 mb which do not correspond to analysis/forecast levels are interpolated, linear in the logarithm of pressure, from the adjacent levels. Mixing ratio is defined to 300 mb, above which it is decreased exponentially.

When the global model output is used to provide the first guess, surface temperature is linearly blended into the profile up to 850 mb; however, the blending is not done if a surface inversion is suspected, either because the surface air temperature is colder than the first guess at the next higher level or because the 3.9 μ window is colder than the 11.2 μ channel (and the sounding is believed to be cloud free). Experience indicates that this blending is beneficial, though marginally in the case of the NGM first guess.

3. The dataset and "best estimate"

The VAS data used for this study were obtained for 6 March 1982. This day was among those chosen for the NASA Atmospheric Variability Experiment (AVE)–VAS assessment program (Hill and Turner 1983; Dodge et al. 1985) when 3-h VAS coverage was coordinated with radiosonde releases from a special, high density network. There are several reasons for choosing this dataset. Most compellingly 6 March is attractive because of the dynamic nature of the weather which occurred over the special network region. A description of the synoptic situation can be found in Jedlovec (1985), and several of the temperature and moisture fields are shown in Figs. 1–4. Also, this case has already been subjected to considerable study. Jedlovec has investigated the results of three retrieval algorithms with respect to the statistical compatibility of VAS and radiosonde temperature, dewpoint and geopotential height. Fuelberg and Meyer (1986) have investigated two of these algorithms with respect to the horizontal structure functions implied by objective analysis of the VAS or radiosonde data. Both studies confirm deficiencies previously observed with vertical soundings from polar orbiting satellites (e.g., Schlatter 1981). The soundings generally exhibit biases, especially when derived with a physical iterative algorithm; they depict sharp vertical discontinuities only if they are present in the first-guess estimate, and they appear to underestimate the horizontal gradients, especially in the

TABLE 2. Pressure levels used for (a) temperature retrieval; and (b) levels available from NGM and stratospheric analyses; asterisked levels are not available from global. Values are millibars.

Type	Pressure level (mb)										
a	1000	950	920		850		780		700	670	620
b	1000	950*		900*	850	800*		750*	700		
a	570	500	475		430		400		350	300	250
b		500					400			300	250
a	200	150	135		115		100		85	70	60
b	200	150					100			70	
a	50	30	25		20		15		10	7	5
b	50	30							10		
a	4	3	2		1.5		1.0		0.5	0.2	0.1

moisture field. In this study, we shall see if the simultaneous algorithm displays these deficiencies to the same extent.

Another attractive aspect of using the 6 March data is that this case has been tested with the subsynoptic forecast model (SSM) which is part of the data assimilation system under development at the CIMSS (Diak 1986). This offers a source of high horizontal (67 km) resolution, contemporary information from which to prepare first guess profiles, and allows testing of first-guess dependence.

A reason against the choice of this case is that the VAS data are not entirely representative of routine operational data. Calibration problems are more numerous than is typically the case. Also, the data were collected using only the large detector array, since, at the time, the advantages of the small detectors were unknown. On the other hand, the spin budget is more generous than those used operationally, and on balance, the results obtained with these measurements seem fairly representative of our routine operation. It should also be noted that for those parts of this report which deal with simulated measurements, the quality of the actual observations is irrelevant.

The ground truth ("best estimate") used in this study is not the special network reports themselves, but rather objective analyses based on these data. These were accomplished using the same recursive filter objective analysis technique which is used to provide boundary estimates of temperature and dewpoint for the retrieval. Input to the analysis system consisted of the special network radiosondes and a forecast first guess provided

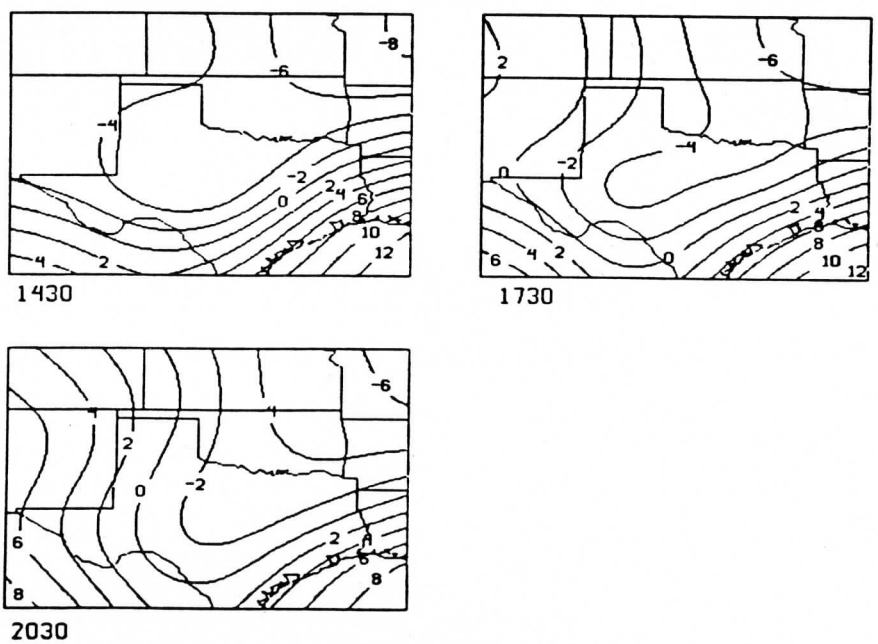

FIG. 1. 850 mb best estimate temperature fields (degrees Celsius) for 1430, 1730, and 2030 UTC 6 March 1983.

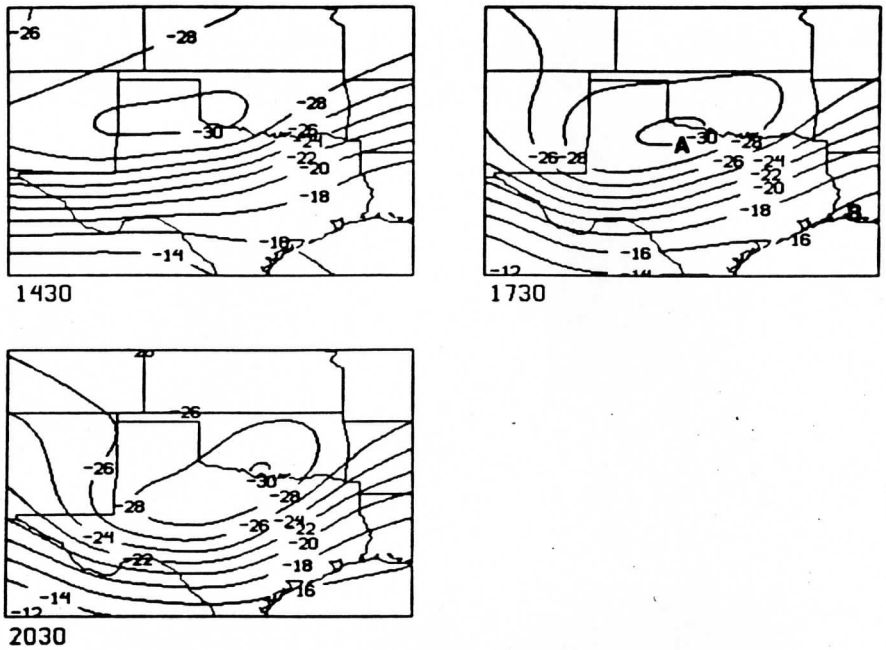

FIG. 2. 500 mb best estimate temperature fields. Points A and B represent locations of "cold" and "warm" soundings used for demonstration.

by the SSM. Because of the density of the radiosondes, the latter had little effect on the analyses except over the Gulf. Analyses were done for the 1430, 1730, and 2030 UTC datasets using the 3, 6, and 9 h forecast fields. A latitude/longitude grid was used with a horizontal resolution of 0.5 deg in each direction, a spacing which is approximately compatible with the normal processing resolution of the VAS. Examples of the analyses for 850, 700, and 300 mb temperature and for 700 mb dewpoint are shown in Figs. 1–4.

4. The forward problem

a. Background

The driving mechanism for making retrievals, as shown in (1), is the difference between the measured

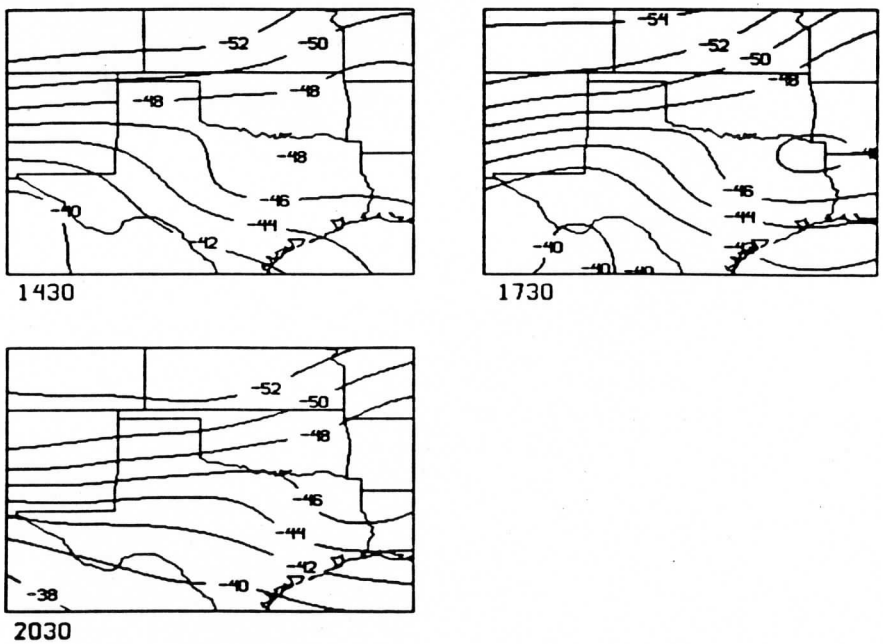

FIG. 3. 300 mb best estimate temperature fields.

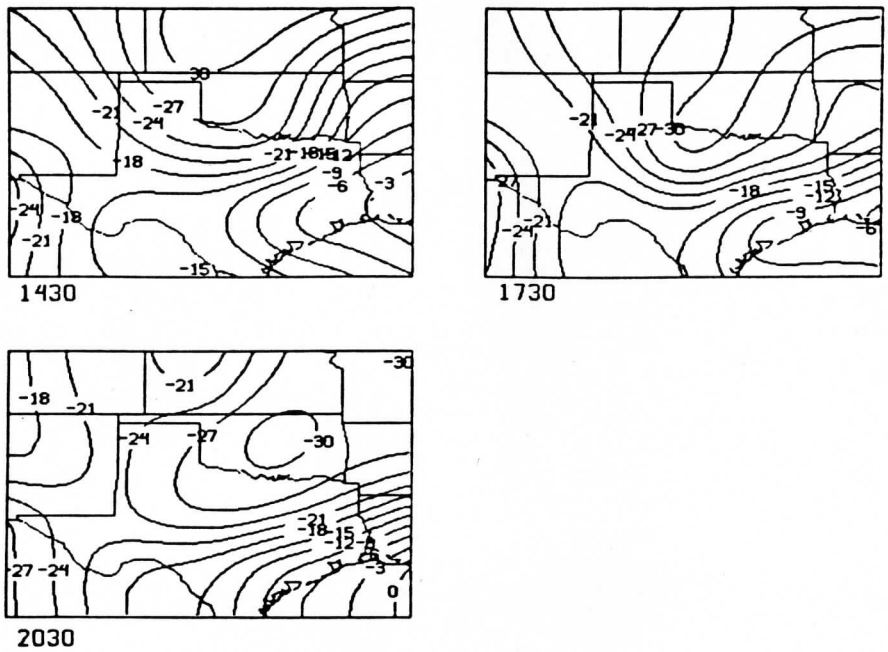

FIG. 4. 700 mb best estimate dewpoint fields.

radiance (converted to a brightness temperature) and one calculated from the first-guess profiles of temperature and moisture. This "forward" calculation is represented by

$$R = \epsilon B_s \tau_s - \int_0^{P_s} B \partial\tau / \partial \ln p \, d \ln p \qquad (12)$$

where R is the radiance and the two terms on the right-hand side represent the surface and atmospheric contributions, respectively. (A third term involving the reflected atmospheric contribution is again ignored.) This section examines the accuracy of the calculation which is critical to the retrieval since inaccuracies in this step will lead ultimately to errors in the retrieved profiles.

Uncertainties associated with emissivity and skin temperature needed to evaluate (12) have been treated earlier. Additional uncertainty arises from inaccuracy in the transmittance model and changing instrumental biases. Both of these deficiencies exist with the VAS. The transmittance model is fixed, but a correction factor in the form of an exponent to the transmittance can be introduced to modify the profile. An example is shown in Fig. 5 for the 4.5 μ shortwave channel. In VDUC processing, this channel is given an exponential factor of 1.1 which makes it slightly more opaque than the theoretical model. The effect on the channel's transmittance profile is mainly to raise the profile slightly as shown in the figure. For the atmosphere shown, this cools the simulated brightness temperature by 1.7 K.

Another method of empirically correcting for observed discrepancies is to define a "bias" vector which can be added to the calculated brightness temperatures if the forward calculations are shown to produce systematic differences from the observed. The exponential and bias corrections are not equivalent since the former has the property of changing the shape of the weighting function, but they produce very similar effects, and the latter is more routinely used (Fleming and Crosby

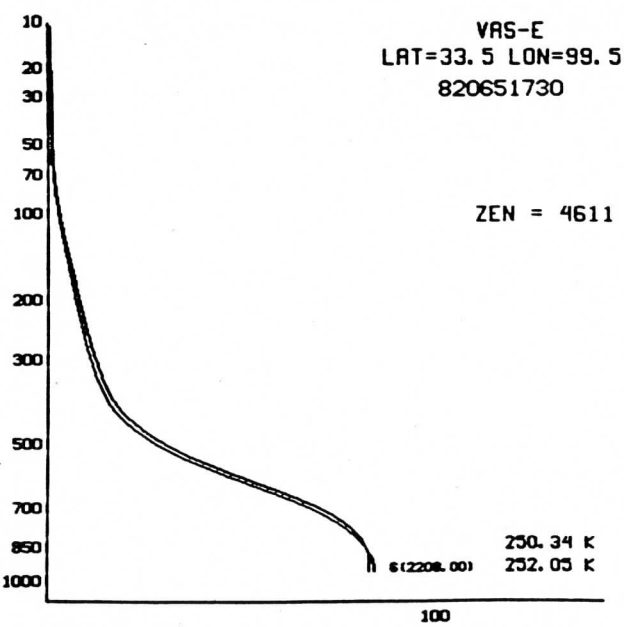

FIG. 5. Transmittance function for VAS channel 6 with exponent factor of 1.1 (top curve), and 1.0 (bottom curve). Function is computed for latitude, longitude, local zenith angle, and date/time shown. Brightness temperatures calculated using two functions are indicated beside curves.

1986). In the VAS processing, channels 6 and 10 have historically had exponential factors, but these have not been changed in many years. Bias corrections, on the other hand, are routinely calculated for all channels and, during the VAS assessment, support to the NWS Centers intermittently changed to reflect both seasonal and diurnal influences. For the case study presented here, an appropriate GOES-4 bias vector was used. For VDUC processing, the bias vector will be frequently updated.

Finally, there is the question of quadrature error in the forward calculation. For computational economy, the calculation in VAS processing is done at 40 pressure levels distributed from 1000 mb to the top of the atmosphere (Table 2). This algorithm has been tested by comparing results obtained using 200 levels between 100 and 1000 mb. The comparison shows that differences up to 0.5 K are not uncommon, suggesting that the 40 level quadrature is acceptable, though only marginally.

b. Results

The efficacy of the forward calculation is evaluated here by comparing brightness temperatures observed for each channel with those calculated from the "best estimate" analyses. The analyses used for the atmospheric contribution have been described previously (e.g., Figs. 1–4). The analyses reach only to 100 mb, and the profiles were extended above this level using the procedures described earlier. A best estimate skin temperature was obtained by combining retrieved skin temperatures (from the observed radiances and the best estimate first-guess profiles) with conventional surface temperature observations. An example of surface air and surface skin temperature for the 1730 UTC dataset is shown in Fig. 6. Note the extreme variability of the skin temperature. The gradient over the Texas Panhandle is caused by a band of melting snow within an otherwise "hot ground" region. Note also that the surface air temperature is not a good estimate of the skin temperature. Obviously, the skin temperature must be defined by the satellite measurements which is why mutliple window channels are included in the instrument. The accuracy of the skin temperatures cannot be directly verified, but they appear qualitatively reasonable, and they are, by design, radiometrically consistent with the "best estimate" temperature and moisture profiles and the VAS observations.

Simulated brightness temperatures were calculated for the three time periods for the ten channels used in the retrieval of temperature and moisture. Some measure of the success of the simulation is shown in Fig. 7 which displays scatter diagrams for these channels. Each point is a comparison of the simulated brightness temperature versus that observed by the VAS. There are a number of interesting features:

- Clearly, the extrapolation of the temperature profiles into the stratosphere is in error. Observed and calculated values for channel 1 are uncorrelated, and channel 2 is only poorly correlated. The influences of the stratosphere diminishes with channel 3.
- Channels 4, 5 and 6, which are the principal measurements for defining the tropospheric temperature, are all successfully simulated with correlations in excess of 0.99. The standard deviations of the comparisons are in the neighborhood of 0.4 K which is greater than the 0.25 K value nominally assigned as random error in solving the inverse problem. However, the 0.4 K estimate incorporates both the measurement error and the error of the forward calculation.
- The correspondence between observed and calculated brightness temperatures for the atmospheric water vapor channels 9 and 10 is not good even though the weighting functions for these channels are below the top-most 100 mb analyses of the "best estimate." These channels are extremely sensitive to rather small changes in water vapor content, and apparently the "best estimate" simply is not good enough. Figure 8 shows the scatter for the brightness temperatures calculated from retrieval profiles. This figure is representative of what should be obtained from a "best estimate."
- The calculations shown in Fig. 7 were made with an emissivity value of 0.96. This value shows a significant improvement over results obtained with a value of unity. An example of the latter is shown in Fig. 9 for channel 7. This may be compared with the results for that channel given in Fig. 7. The mean discrepancy

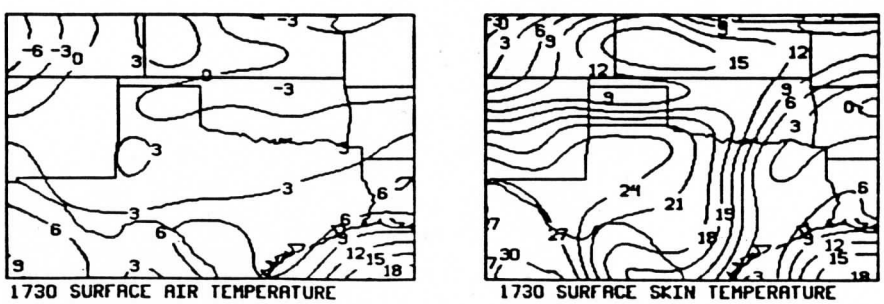

FIG. 6. Surface air and skin temperature for 1730 UTC.

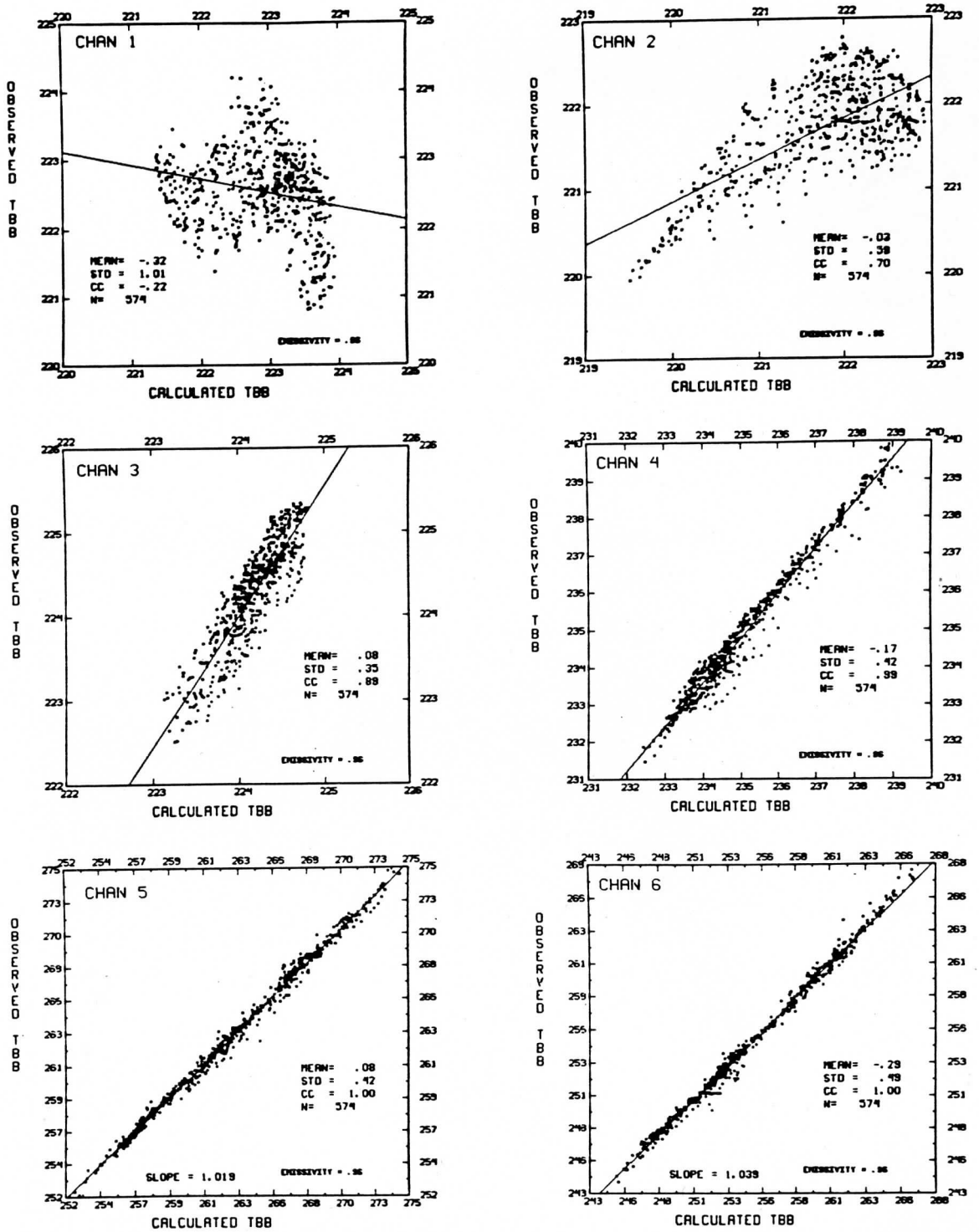

FIG. 7. Scatter diagrams of observed brightness temperature versus value calculated from best estimate for ten VAS channels. Mean difference, standard deviation and correlation coefficients are indicated.

between observed and calculated brightness temperature has been substantially reduced from −3.22 to −0.81 K; the standard deviation of the discrepancy has been somewhat reduced from 0.76 to 0.65 K; and the slope of the regression line slightly improved from 0.95 to 0.97. An equivalent improvement is seen with channel 8 (not shown). Channels 5 and 6 are improved in terms of mean discrepancy with the reduced emissivity,

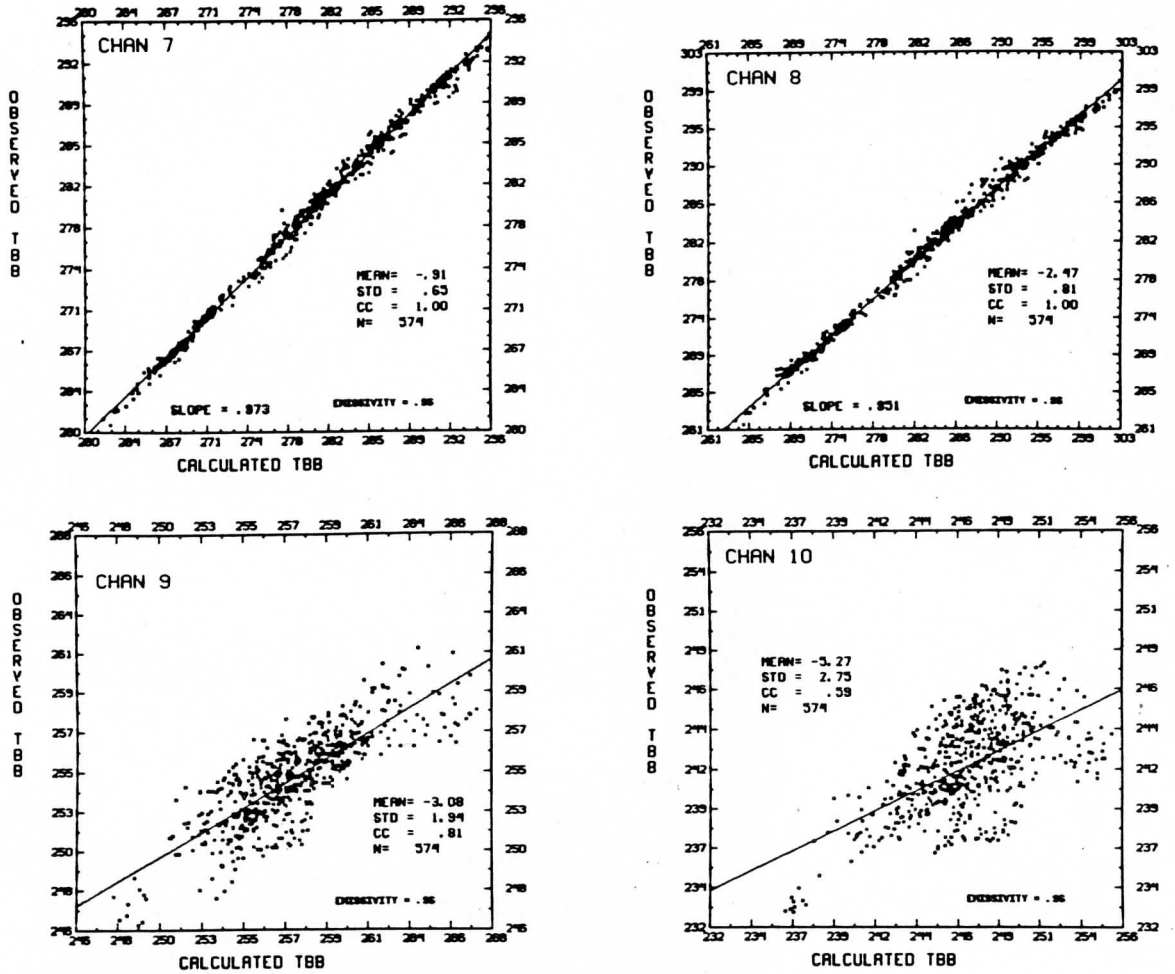

FIG. 7. (*Continued*)

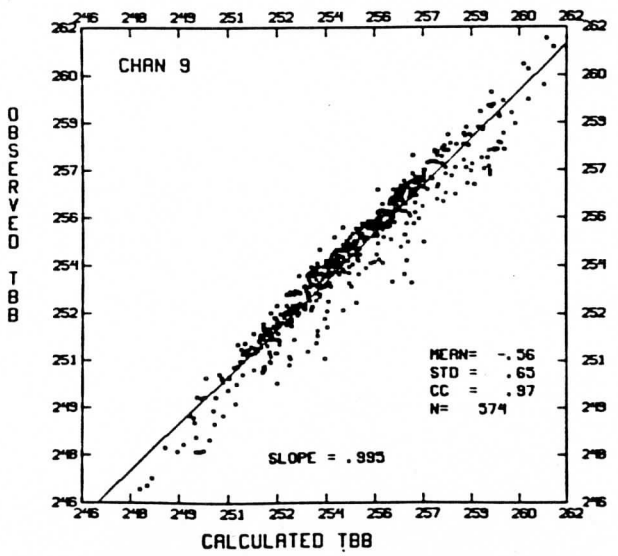

FIG. 8. Scatter diagram of observed brightness temperature versus values calculated from retrievals based on observed brightness temperatures and best estimates.

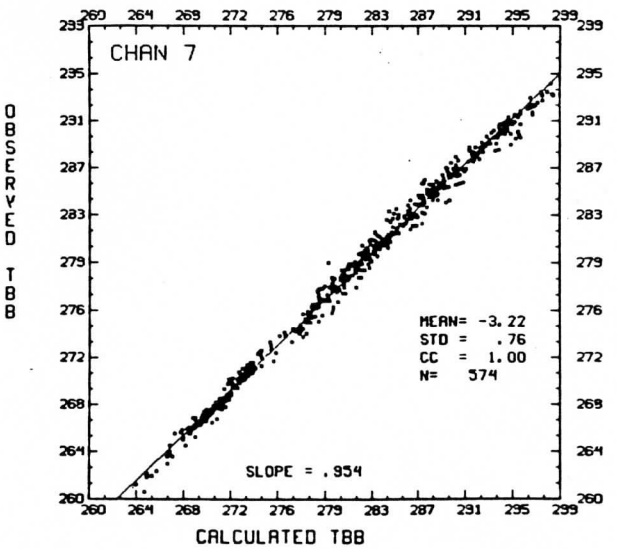

FIG. 9. Scatter diagram obtained for channel 7 under conditions shown in Fig. 7, except emissivity = 1.

but the standard deviations are essentially unchanged. The value of 0.96 (over land) was introduced to the VAS processing in June 1986 based on subjective evaluation of retrievals produced for the National Severe Storms Forecast Center. This case study is a quantitative demonstration of its beneficial effect.

- The slopes of the best-fit lines for channels 7 and 8, and especially for 9 and 10 are less than 1. Calculated brightness temperatures are slightly too warm at the cold extreme and significantly too warm at the warm end. Both effects are likely caused by underestimating the moisture in the "best estimate."

The important conclusion is that, with two exceptions, the observed brightness temperatures are compatible with the "best estimate" temperature and moisture profiles. Therefore, the question of "bad measurements" does not apply to the discussion of the inverse problem below. The exceptions are that 1) the stratospheric channels are not verifiable, and therefore a stratospheric evaluation will not be attempted; and 2) there is some difficulty in matching the moisture channel measurements which must be recognized in evaluating the moisture retrievals.

5. The inverse problem

a. Background

In this section, the sensitivity of the retrieval algorithm is examined at two locations taken from the 1730 UTC period for the 6 March situation. Figure 10 shows temperature and moisture profiles at the two locations (see Fig. 2). The profile on the left is located in the closed contour of the 500 mb temperature and in the dry tongue at 700 mb (see Figs. 2 and 4). The profile on the right is ahead of the front in the warm, moist air. Both are close to radiosonde locations. The heavy lines represent values taken from the "best estimate" analyses while the lighter lines are from the first guess, in this case, linearly time-interpolated from the LFM analysis at 1200 UTC and the 12 h forecast from that time. Errors are apparent in both the first guesses. In the case of the cold sounding, the guess has failed to define the low tropopause, and has missed the drying at 700 mb. For the warm sounding, the guess is too cold from the surface to 300 mb, and the moisture is underestimated at low levels.

Figures 11 and 12 show the "weighting" functions for temperature (left) and moisture (right) for the two soundings shown in Fig. 10. The weighting functions consist of the terms multiplying dU and dT in the first two integrals of (1) for moisture and temperature, respectively. In some sense these weighting functions determine the vertical sensitivity of the retrieval, since they represent the vertical smearing of the signal received at the satellite. From this standpoint, several features can be noted:

- The weighting functions vary markedly with changes in air mass; the VAS instrument may be quite adequate for a sounding in some situations, whereas it may be rather inadequate for others. For example, in the cold, dry sounding (Fig. 11) there is very little sensitivity to the atmosphere between 200 and 600 mb. This does not correct the error of the first guess shown in Fig. 10. The situation is greatly improved for the warmer sounding (Fig. 12).
- The moisture sensing channels (9 and 10) have a large "weight" for both temperature and moisture and, therefore, play a large role in the correction of both quantities. The temperature-sensing channels (1–6) have no such role in the moisture correction although

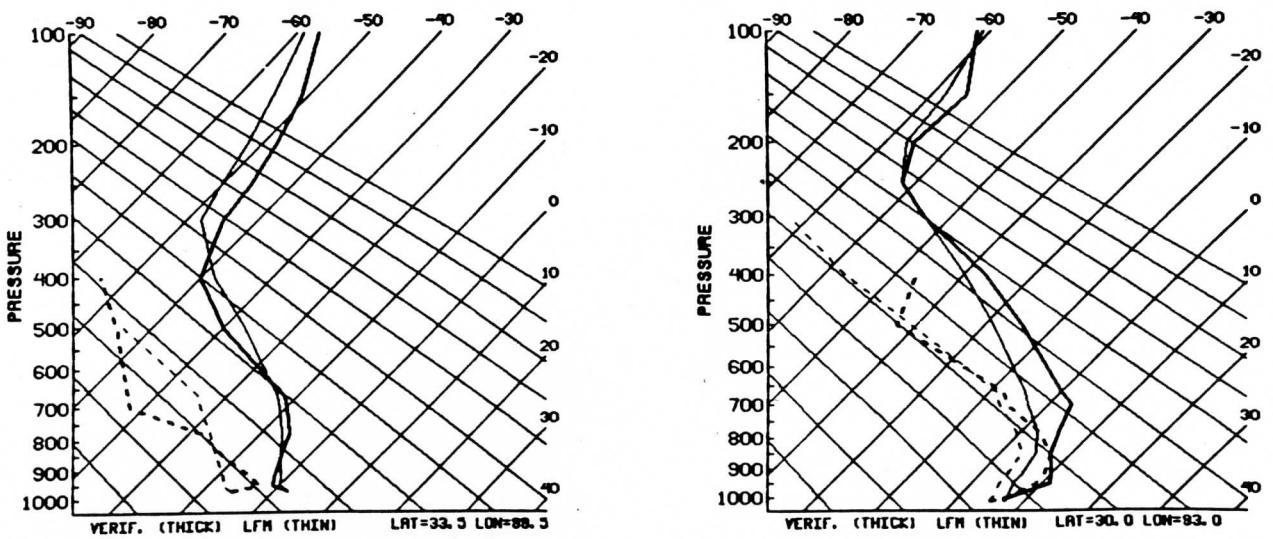

FIG. 10. Skew-T temperature/moisture profiles behind (left) and ahead (right) of cold front for 1730 UTC 6 March 1982. Thick lines are from best estimate; thin lines are from interpolated LFM analysis/forecast.

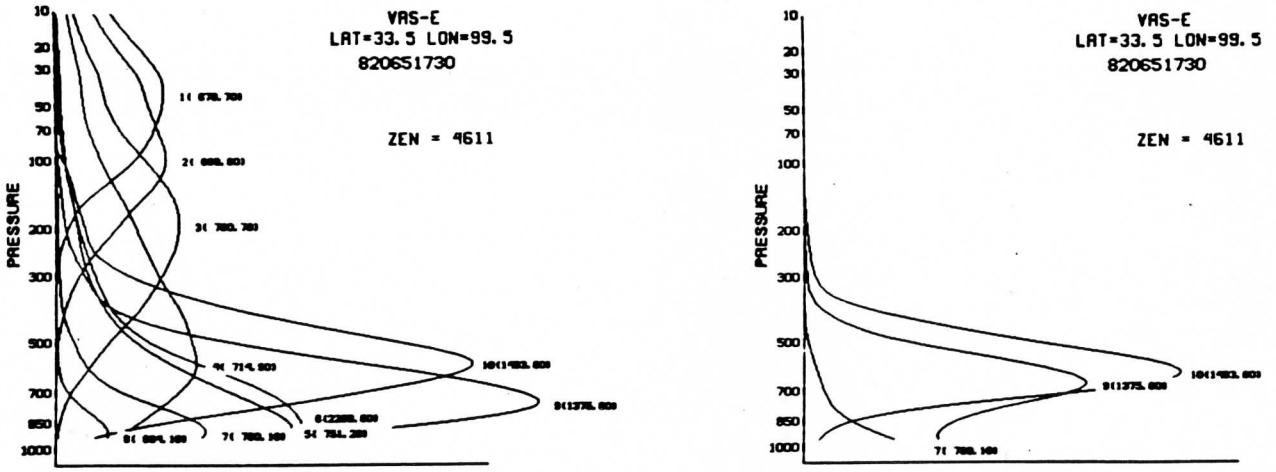

FIG. 11. Temperature (left) and moisture (right) weighting functions for cold best estimate profile shown in Fig. 10 (left).

they do have very small contributions below 700 mb. Their weights are not shown in the righthand figures because they are so close to the ordinate.

- Above 300 mb the VAS weighting functions are broad and not very discriminating.

Figure 13 is similar to Fig. 10, except that the VDUC retrieval replaces the first guess. For the cold sounding, there is some improvement at high levels, but the tropopause error remains and the retrieval is dry at low levels. For the warm sounding there is a large improvement in the temperature, but the moisture at midlevels is questionable. These results are quite typical. Where there is a temperature bias error over a deep layer, as in the warm sounding, the retrieval does very well. However, when there is a compensating error over a layer, as in the cold sounding, the lack of vertical resolution in the measurement (and the algorithm) seems to preclude a correction. In the case of moisture, sharp discontinuities such as that shown in the cold sounding are often observed which suggest that the algorithm is marginally stable for moisture, largely because the moisture sensitive channels are few in number and not uniformly spaced in the vertical. These results depend to some degree on the choice of tuning factors as is demonstrated in the following tests.

b. 1-Pass

It was explained earlier that the VDUC algorithm includes two passes of the retrieval with a tightening of γ in (10) on the second pass after the transmittances and therefore the weighting functions have been improved by the first pass. Intuitively, the need for multiple passes must depend on the accuracy of the first guess of temperature and moisture; poorer guesses require the iterative approach. Experience using the LFM for the first guess suggests that the second pass is not

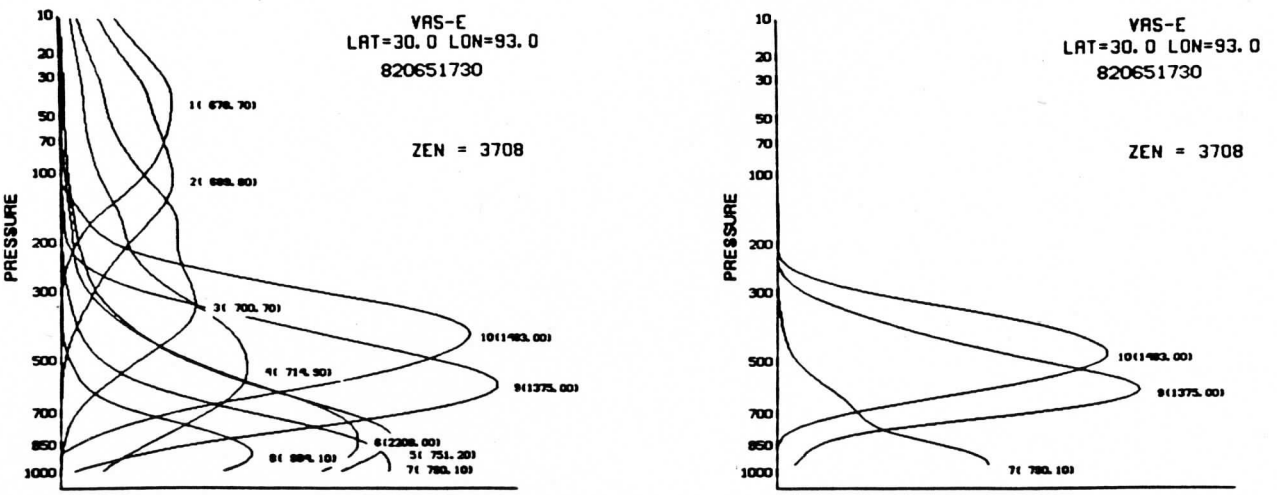

FIG. 12. As in Fig. 11, but for warm profile shown in Fig. 10 (right).

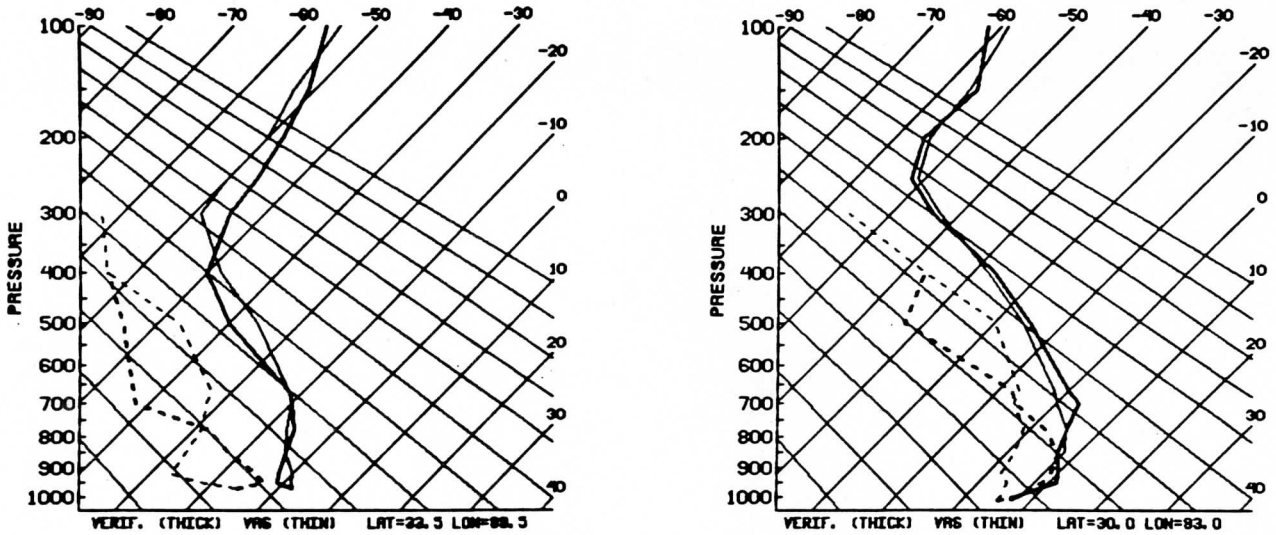

FIG. 13. Skew-T profiles for soundings shown in Fig. 10. Thick lines from best estimate; thin lines represent VDUC retrievals from LFM estimate.

necessary. For example, Fig. 14 presents the 1-pass results for the two situations of Fig. 13 (with the second pass "gamma" applied on the first pass). For these two cases, the 1-pass results are as good or better than the 2-pass. Note that the low-level oscillation of the moisture in the cold sounding has been improved, but a new questionable peak has appeared at 500 mb. Lacking firm evidence that the second pass is beneficial, VDUC operations will use the 1-pass approach since it is more economical.

c. Basis functions

The basis functions used with (4) are, as explained above, a limited set of the vertical derivatives of the transmittance functions. These are chosen to represent the physical information of the system and to be distributed relatively uniformly in the vertical. The set is limited so that the inversion is over-determined and therefore less likely to be unstable. The weakness in this argument is that the basis functions, like the weighting functions, are situation dependent. This can be seen in Fig. 15 which shows the basis functions corresponding to the soundings of Fig. 10. (Note that the basis functions are normalized.) For the VDUC choice of temperature functions (2, 3, 4, 5, 7), only function 4 has any representation in the middle troposphere for the cold sounding. This is at least partly responsible for the result shown in Figs. 13 and 14, where the first guess is unchanged in the middle troposphere. Figure 16 gives results obtained when the VDUC temperature

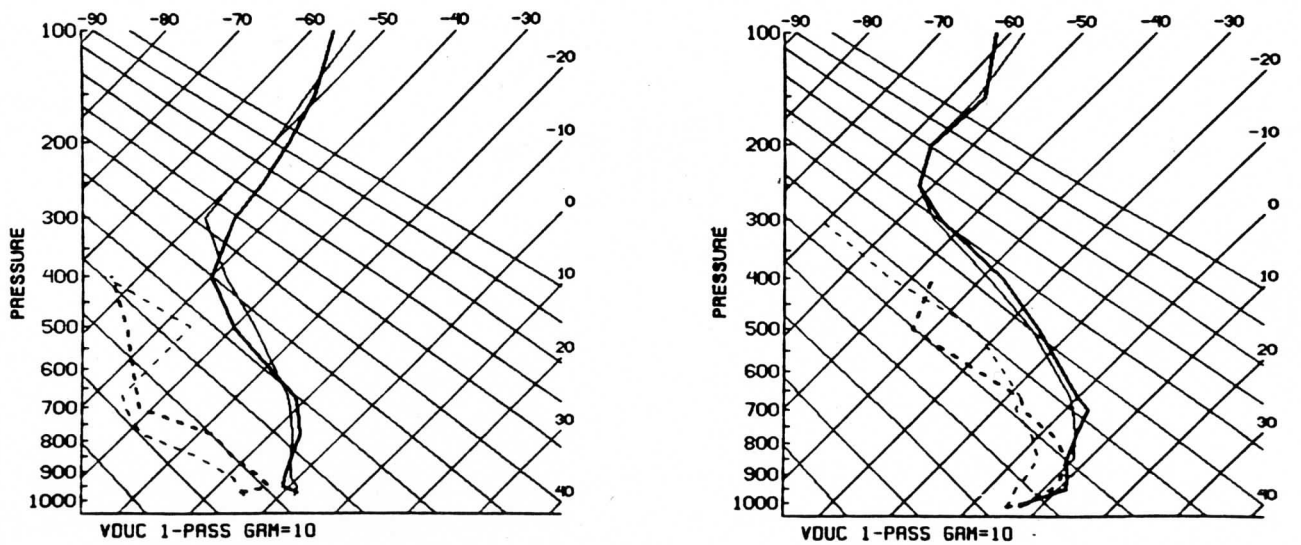

FIG. 14. As in Fig. 13, except thin lines represent VDUC retrievals using the single-pass option.

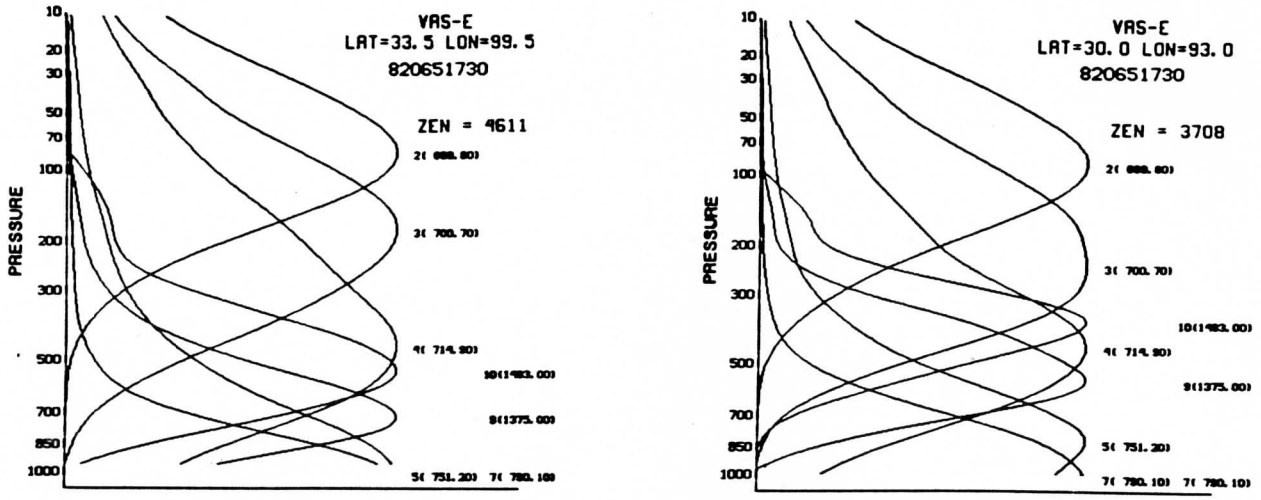

FIG. 15. Pressure basis functions computed from best estimate profiles shown in Fig. 10.

basis functions are replaced by (3, 4, 5, 9, 10). The conditions are otherwise the same as those for Fig. 14. The better representation in the middle troposphere gained by using 9 and 10 has improved the retrieval of the cold sounding. However, by not using the channel 2 basis function, the retrieval of the warm sounding is degraded.

The conclusion drawn from a number of experiments like the one just described is that the retrieval is fairly sensitive to the selection of basis functions for its vertical representation of the temperature and moisture structure. Some choices are better than others for a given situation, but no choice seems clearly superior for all. For this aspect of the retrieval problem, more channels should be beneficial.

d. Gamma

The most critical tuning factor in the algorithm is the choice of γ in (10), which controls how closely the observations are fit in the solution. Note that this does not mean that each channel will be fit to its prescribed error. The redundancy of the system leads to a solution which best fits the majority. However, decreasing gamma encourages independence which will eventually lead to instability. Figure 17 shows the retrievals for the two situations shown in Fig. 16, but with a gamma reduced by a factor of 10, other options being the same. Both soundings of Fig. 17 display signs of instability and are inferior to those obtained with the larger gamma.

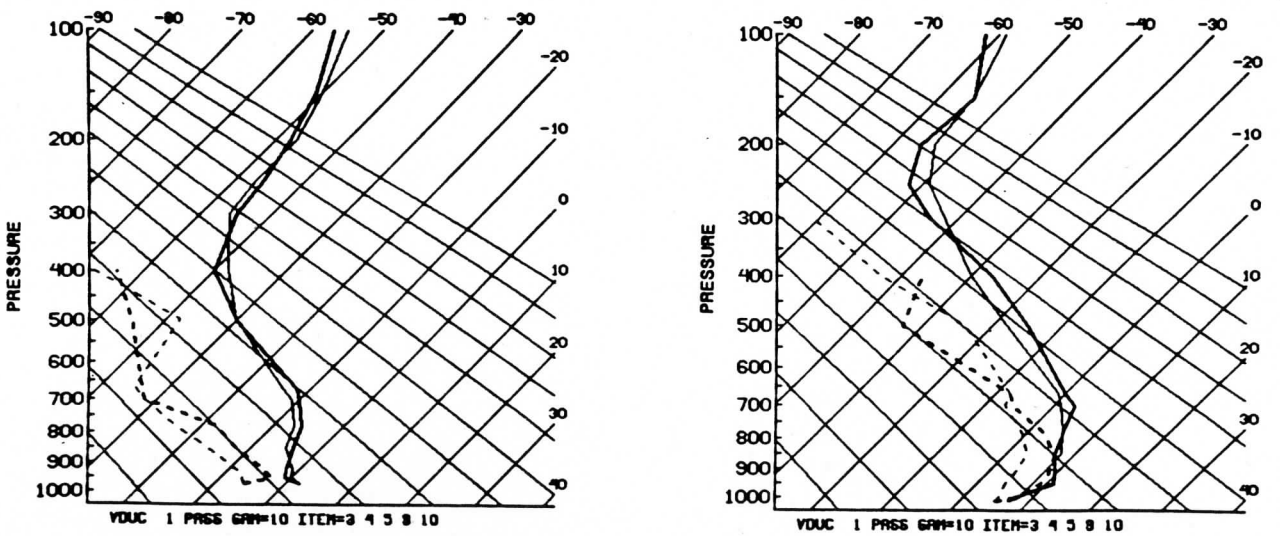

FIG. 16. As in Fig. 14, except retrieval pressure basis function changed from (2, 3, 4, 5, 7) to (3, 4, 5, 9, 10).

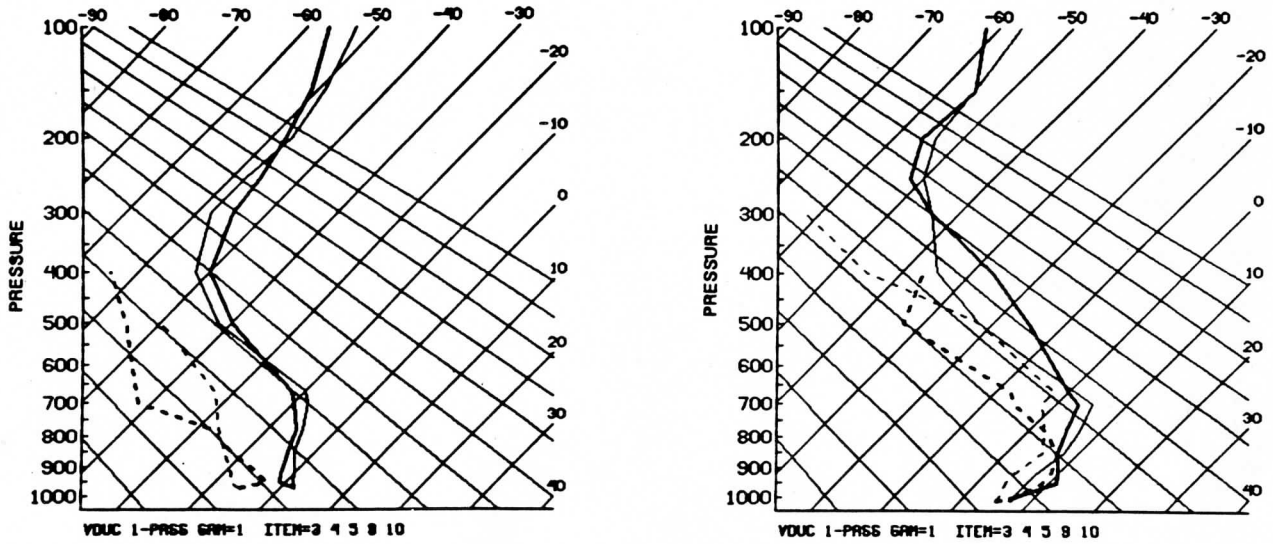

FIG. 17. As in Fig. 16, except retrieval sensitivity has been increased by a reducing "gamma" by a factor of 10.

e. Channel exclusion

The question of excluding channels from the retrieval is yet another area where the answer is not clear. Exclusion is easily accomplished in the VDUC algorithm by artificially inflating the error estimate of a given measurement to the point where it has no influence on the inverse solution. It was mentioned earlier that channel 8, the 11.2 μ window, is routinely excluded. This allows greater variance in the solution for skin temperature which seems to act as a sponge for errors caused by inconsistencies in the radiance measurements (from inaccurate cloud clearing). Undoubtedly, a poorer estimate of the skin temperature results, but as a trade-off, the greater sensitivity in the skin temperature retrieval can be used for quality control. Experience suggests that the exclusion of channel 8 is advantageous over land but detrimental over the ocean, possibly because in the latter case the skin temperature is less variable or because the lack of surface reports leads to a poorer specification of the first guess.

In early versions of the simultaneous algorithm, the shortwave channel (6) was excluded in the "cloudy path" and also when channels 5 and 6 seemed to be in conflict. However, failure to use the same complement of channels for all soundings has been shown to be detrimental, because the vertical bias characteristic of the retrieval is a function of the channels (and the basis functions, and the first estimate). A change in the vertical bias from one sounding to another results in an artificial horizontal gradient which is highly undesirable. (For this reason, we do not employ the option of using channel 8 over the ocean but not over land even though, based on the previous discussion, it might seem reasonable to do so.)

Another example of where it might seem desirable to exclude, or at least greatly reduce the influence of a channel is offered by the case study presented here. It is evident from the scatter shown in Fig. 7 for channels 1 and 2 that the first guess for temperature above 100 mb is poor. If one is interested only in the troposphere, it might be tempting to exclude these channels since in the inversion, they will attempt to make significant adjustments to the first guess in the stratosphere which, given the coarse vertical resolution of the system, might be smeared in the vertical to degrade the better first guess at lower levels. Figure 18 addresses this question, showing the retrievals of Fig. 16 repeated with the two top channels excluded. Changes are apparent, but not, perhaps, as anticipated. The warm sounding has been improved at high levels, but degraded near the surface. Also, the cold sounding is slightly degraded. Sensitivity is evident, but cause and effect are not clear. Since, in principal, channels 1 and 2 should improve the stratospheric guess, and therefore the small stratospheric contributions to the more transparent channels, they are retained in the VDUC algorithm. Also, it should be added that stratospheric analyses were not available for the first guess in this study, so Fig. 7 gives an atypical example for the stratospheric channels.

f. First guess

The shape of the initial profiles of temperature and moisture has a strong influence on the retrieval, just as does the choice of basis functions or channels. The first guess is one more ingredient in the ill-posed problem. An important question, from the standpoint of data assimilation, is whether or not the error of the first guess is correlated with the error of the retrieval. This matter cannot be settled by considering one or two profiles. For example, a comparison of Figs. 10 and 13 suggests strongly that error correlation exists, but a comparison of Figs. 10 and 16 suggests that it

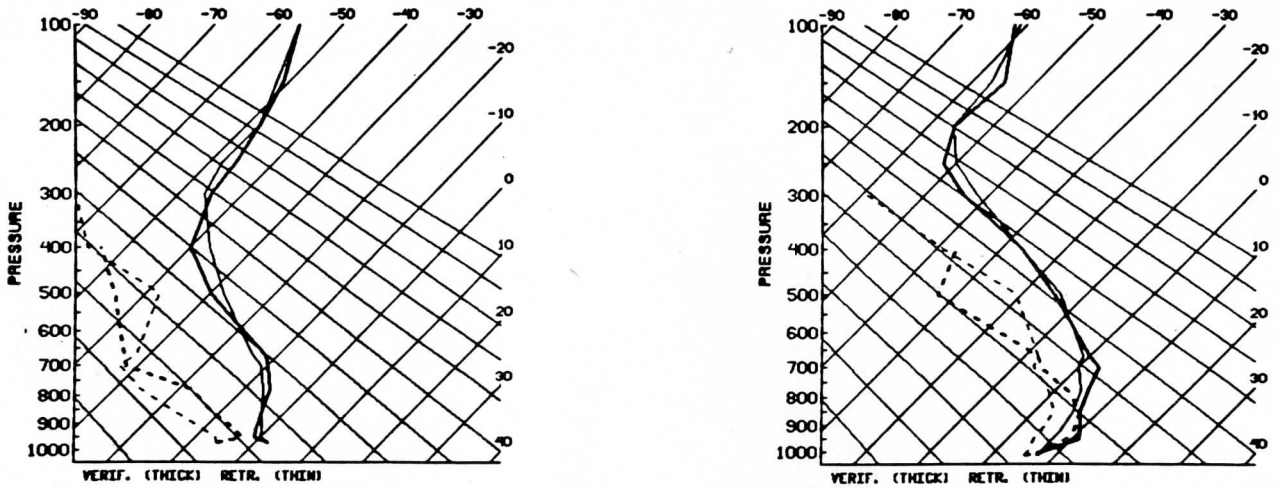

FIG. 18. As in Fig. 16, except VAS channels 1 and 2 have been excluded from the retrieval.

does not. More will be said on this topic in section 6 when the retrievals are considered in terms of the three-dimensional representation of the atmosphere.

A major reason for exploring the sensitivity of the VDUC retrieval algorithm to various configurations is to stress that the simultaneous solution contains no cure for the basic nonuniqueness of the problem. Different constraints yield different solutions. However, it should be emphasized that in all cases, excepting that where the gamma was overconstrained, the retrievals have not degraded and usually improved the first estimate.

Up to this point, the retrievals have been considered individually in terms of their vertical structure. To scrutinize this aspect is to attack the retrieval question at its weakest point. Radiosondes depict vertical structure; radiometer measurements can only nudge a first estimate in the right direction. The strength of the VAS has been touted as its capability to define horizontal structure where it measures with higher resolution than the radiosonde. The case study of section 6 addresses this claim.

6. Case study, 6 March 1982

Fields corresponding to Figs. 1–4 are presented for the first estimates generated from the LFM (Figs. 19–22) and from the SSM (Figs. 23–26). Fields analyzed from the retrievals using these first estimates are given in Figs. 27–30 and Figs. 31–34. Salient features of these figures are given in the following subsections.

a. 850 mb temperature

Figure 1 shows the cold trough at this level moderating with time as it moves to the southeast. The strong frontal gradient over eastern Texas moves ahead of the trough with the temperature along the Gulf coast cooling approximately 4°C over the 6 h. Strong ridging takes place behind the trough with temperatures increasing by 8°C over New Mexico. In the LFM forecast (Fig. 19), the trough is slightly too cold, the frontal gradient is too weak (a 6 h change of only 2°C over the Gulf coast), and the ridging over New Mexico is initially too strong and finally too weak giving a temperature increase of only 2°C. Addition of the retrievals (Fig. 27) has improved these features, especially the last two with the Gulf coast temperature change restored to 3°C and the New Mexico one increased to perhaps 5°C. (The latter improvement is partly an artifact of the objective analysis; as much of New Mexico is above the 850 mb surface as indicated by the absence of retrievals.) The SSM forecast (Fig. 23) is initially somewhat better than the LFM but does not hold the advantage, especially in terms of the shape of the trough at 2030 UTC. The VAS retrievals have helped considerably in restoring the shape (Fig. 31). In general, the VAS appears to have significantly improved the first estimates in both cases, and yet there are considerable differences between the two VAS products (Figs. 27 and 31) which reflect properties of their respective first estimates.

b. 500 mb temperature

The situation at 500 mb is qualitatively similar to that at 850 mb except that the cold air is represented by a closed −30°C contour and the tight gradient leading the trough is confined inland over the special network in Texas (Fig. 2). Ridging is again observed behind the trough over the 6 h period. The principal deficiency of the LFM forecast (Fig. 20) is that the trough is too warm and diffuse, especially with respect to the gradient over eastern Texas. The retrievals based on the LFM (Fig. 28) do not capture the cutoff (although there is a hint of it at the last time period), but they do reshape the contours more correctly and significantly improve

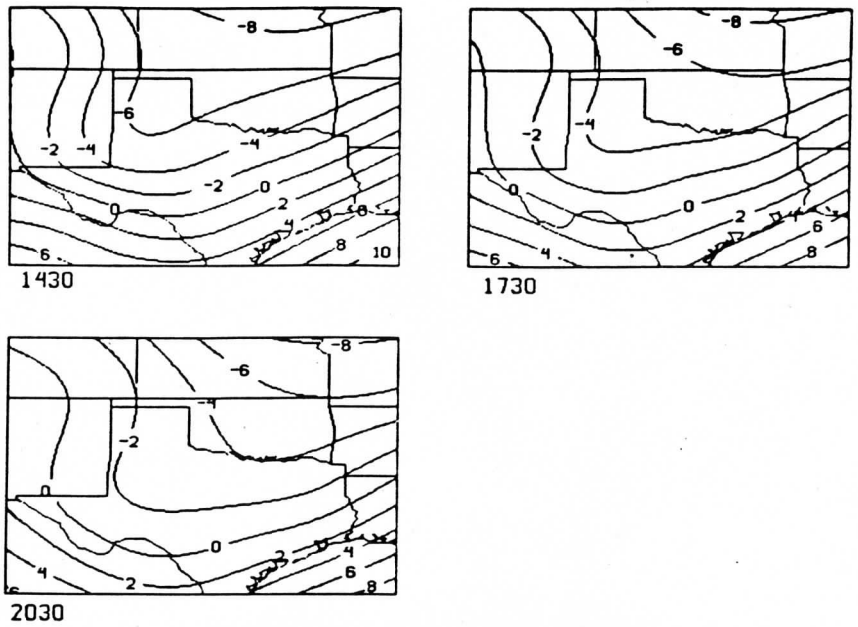

FIG. 19. The 850 mb temperature analyses (degrees Celsius) derived from the LFM estimate for 1430, 1730, and 2030 UTC 6 March 1982.

the gradients across eastern and southern Texas. Gradients are also tightened over the gulf, perhaps erroneously, but there are no data to provide verification. This SSM forecast (Fig. 24) is clearly better than that of the LFM, but is still too warm in the center of the trough and underestimates the gradient, particularly on the eastern side. Retrievals based on the SSM again improve the first guess (Fig. 32), especially with regard to the gradient ahead of the trough.

c. 300 mb temperature

The pattern at 300 mb is very different from that at lower levels. Figure 3 shows an abrupt splitting of the north–south temperature gradient over central Texas at 1430 UTC, which moves rapidly eastward in phase with the front. The LFM forecast (Fig. 21) has only a weak indication of this feature and significantly underestimates the gradient in the western portion. Retrievals

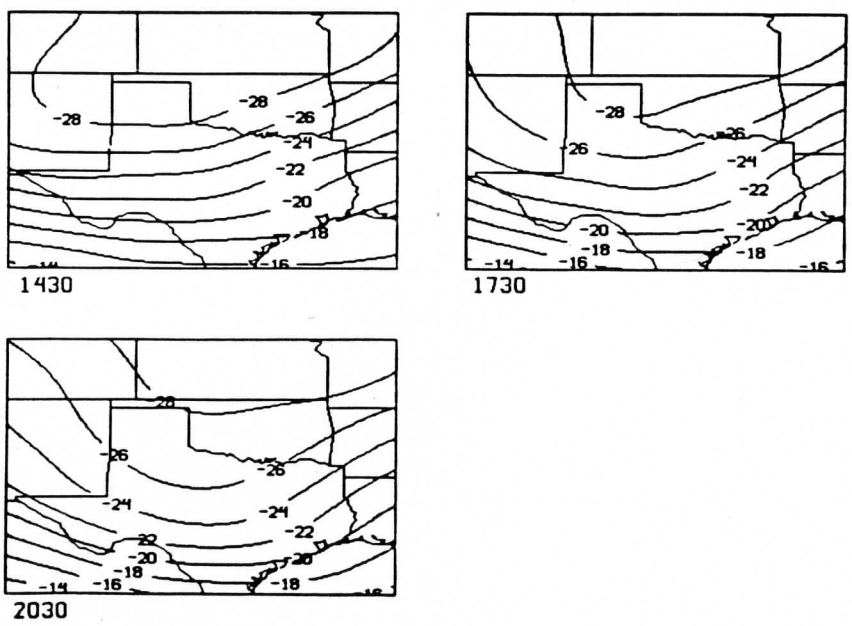

FIG. 20. As in Fig. 19, but for 500 mb temperature.

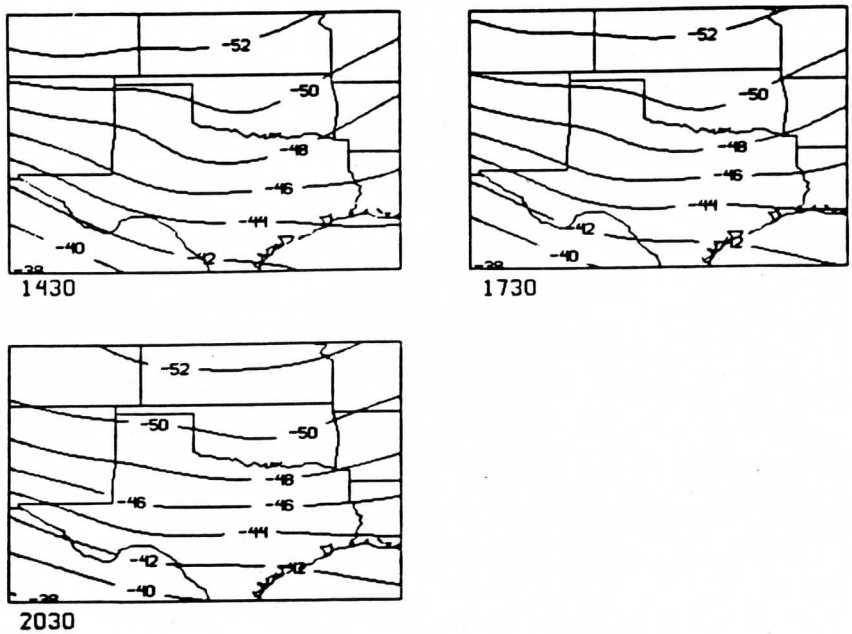

FIG. 21. As in Fig. 19, but for 300 mb temperature.

based on the forecast (Fig. 29) do not appear to correct these errors. However, if one looks closely at the orientation of the −46 Celsius contour relative to the −48 Celsius contour, it is possible to see that even at this level there is some improvement of the first estimate. The SSM forecast (Fig. 25) captures the main features at this level, and the retrievals from this forecast (Fig. 33) generally maintain the shape. However, the fields from the retrievals seem erroneously to increase the gradient, especially at the later time periods.

d. 700 mb dewpoint

Figure 4 presents the best estimate 700 mb dewpoint fields. There is considerably more uncertainty here as compared to temperature because the data are quite noisy and the moisture is highly variable. For example, the objective analysis has reversed the gradient in the gulf at the first two time periods, which seems unreasonable. However, there is good continuity in the movement of the dry tongue and the associated leading

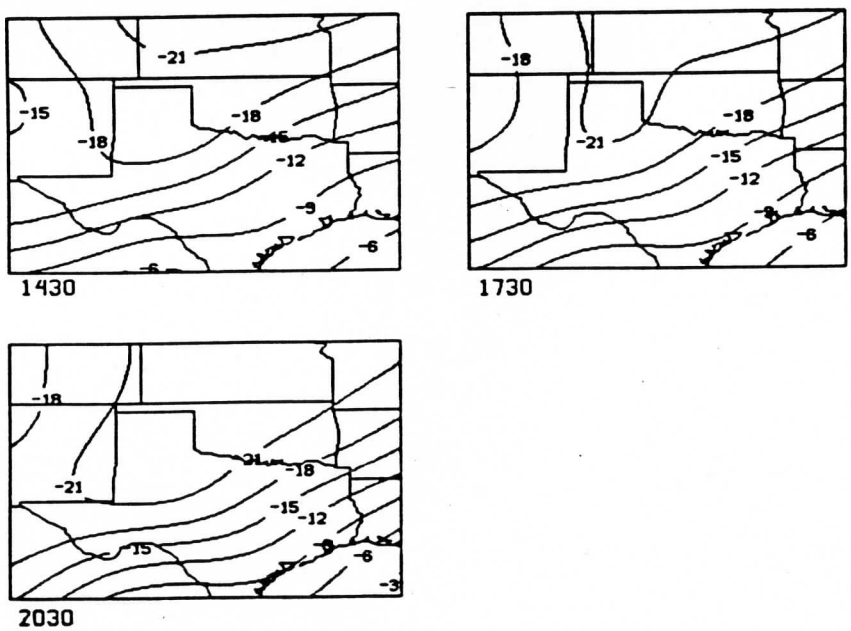

FIG. 22. As in Fig. 19, but for 700 mb dewpoint.

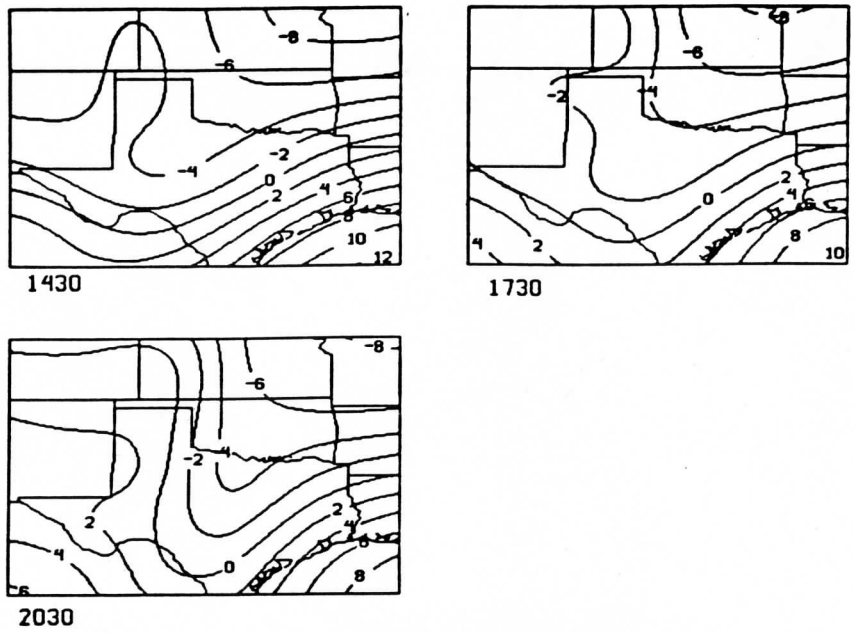

FIG. 23. The 850 mb temperature analyses (degrees Celsius) derived from the SSM estimate for 1430, 1730 and 2030 UTC 6 March 1982.

front over Oklahoma and eastern Texas. The LFM forecast (Fig. 22) positions the major features fairly well, but the gradient is greatly relaxed and continuous over southern Texas and Mexico contrary to the best estimate. The SSM forecast (Fig. 26) is similar to the LFM except that it does a better job in the southern portion. The retrievals from the two first estimates (Figs. 30 and 34), apart from a large bias difference, are quite similar, and qualitatively appear to be a significant improvement on either first guess. They also show good time continuity in the way they have changed the first estimates. Of particular interest is the moist pocket which migrates from New Mexico into south central Texas during the 6 h. There is some support for this feature in the best estimate but the radiosonde reports are too sparse to define it.

e. Statistical comparisons

Scatter diagram comparisons for the analyses of 500 mb temperature and 700 mb dewpoint are given in

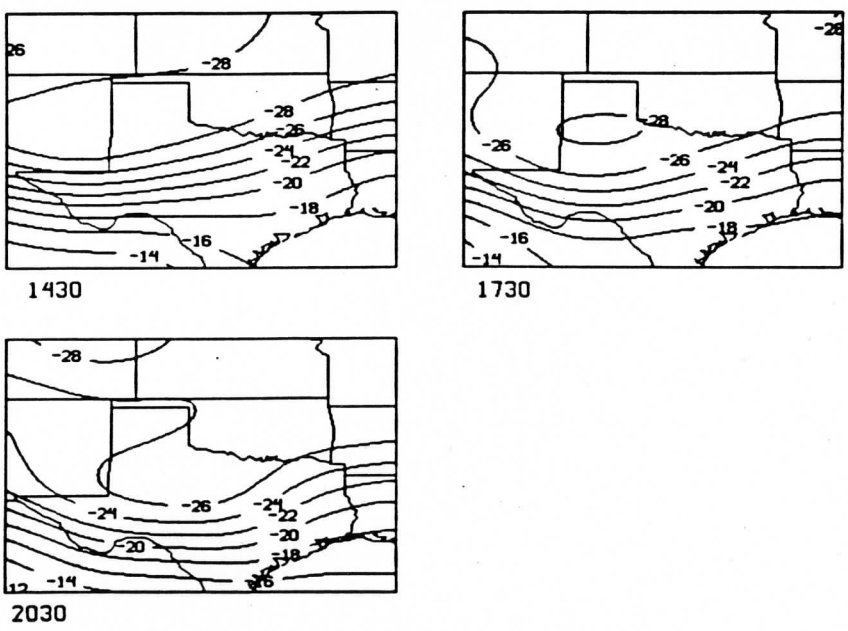

FIG. 24. As in Fig. 23, but for 500 mb temperature.

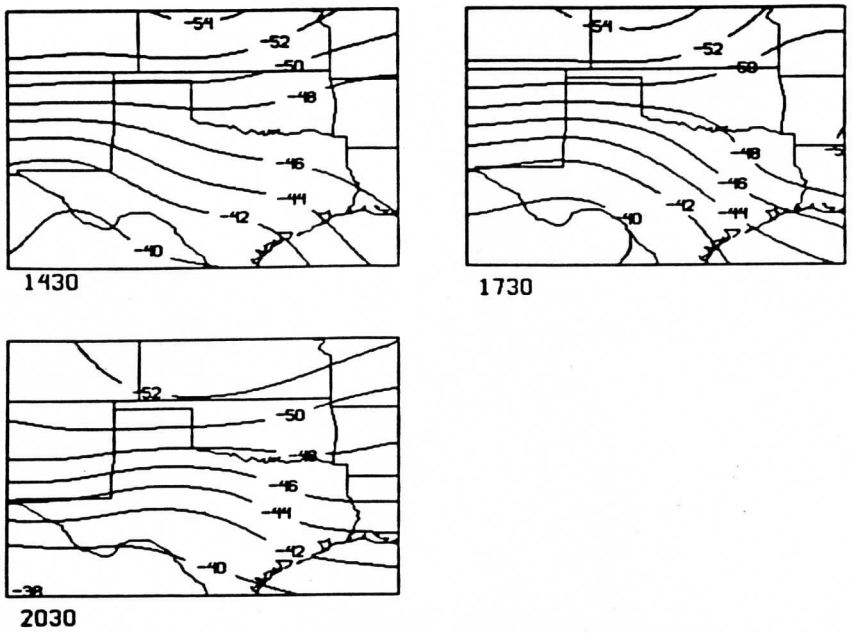

FIG. 25. As in Fig. 23, but for 300 mb temperature.

Figs. 35 and 36. Values taken at grid points are combined for all three time periods. In each figure the top panels compare first estimate values from the SSM and LFM forecasts to the "best estimate". The middle panels compare retrievals from these estimates, using the observed radiances, to the "best estimate". The lower panels compare retrievals from these estimates, using the simulated radiances (Fig. 7), to the "best estimate". Statistics relating to the comparisons are included in each panel. Highlights are

- Subsection 6d brought up the question of correlation between the error of the first guess and the error of the final retrieval. This error is evident for both fields for both observed and simulated radiances. The pattern of the scatter in the first guess (top panel) is preserved in the lower panels. This feature in the simulated results is particularly significant since many sources of uncertainty associated with real measurements have been eliminated.
- In general the better the first guess the better the

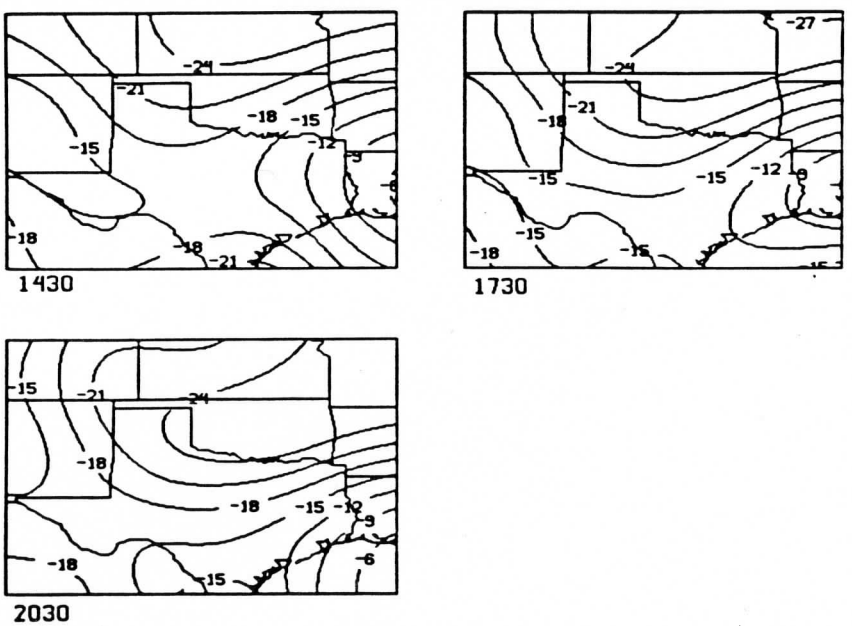

FIG. 26. As in Fig. 23, but for 700 mb dewpoint.

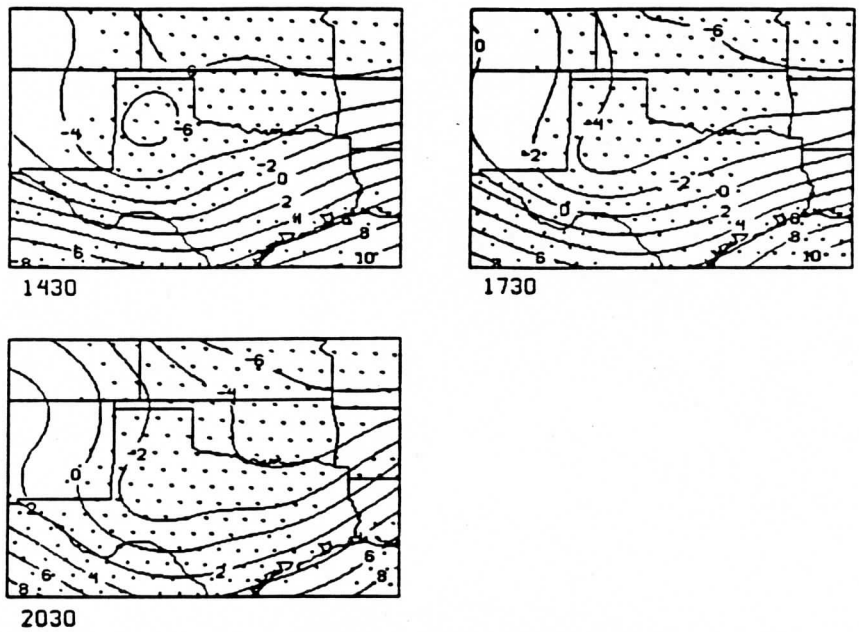

FIG. 27. The 850 mb temperature analyses (degrees Celsius) derived from the VAS retrievals initiated with the LFM estimate for 1430, 1730 and 2030 UTC 6 March 1982. Locations of retrievals are indicated.

retrieval. This is most easily seen in the simulated radiances, comparing the top and bottom panels. For example, the standard deviation of the 500 mb temperature error of the LFM estimate is reduced from 1.9 to 1.3 K, whereas that of the SSM guess is reduced from 1.1 to 0.9 K.

• There is some fundamental inconsistency between the best estimate temperature and the observed radiances. For the 500 mb temperature, the observed radiances (middle panels) have produced a strikingly similar pattern from both first estimates, and the regression line equations are almost identical. In the case of the SSM, the retrieval has significantly degraded the first estimate. A part of the similarity is caused by a systematic change in the error pattern for both retrievals over the three time periods. Relative to the best

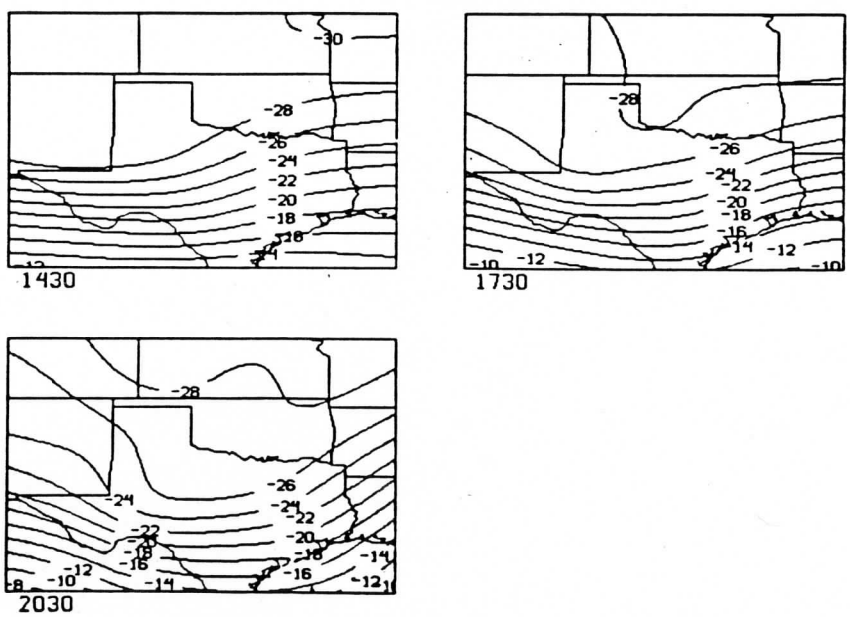

FIG. 28. As in Fig. 27, but for 500 mb temperature.

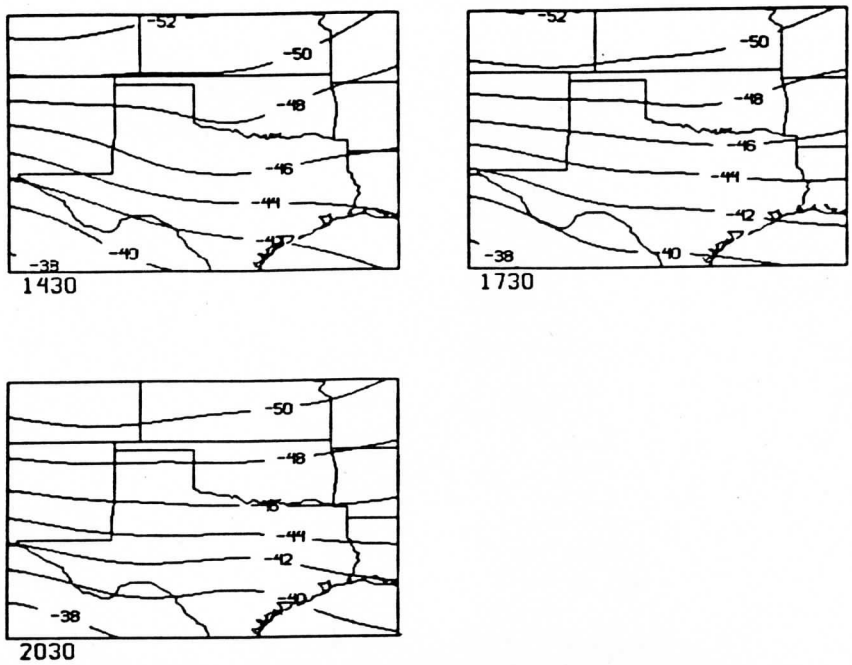

FIG. 29. As in Fig. 27, but for 300 mb temperature.

estimate temperatures the retrievals become warmer with time. This suggests an error in the physics of the retrieval algorithm. The "curvature" feature is common to all time periods and may reflect an error in either the physics or the best estimate.

• Bias introduced by the retrieval appears to be more significant in the case of moisture. For both first estimates, the mean error is changed by 3 K, but in opposite directions, and the final biases (bottom panels of Fig. 36) are different by 5 K.

• As documented by other research (Jedlovec 1985), the horizontal gradient is underestimated in the retrievals. The correct gradient would be represented by a slope of 1 in the regression equation given on each panel. In every case the slope is less than 1. However, with the exception of the 500 mb temperature retrievals

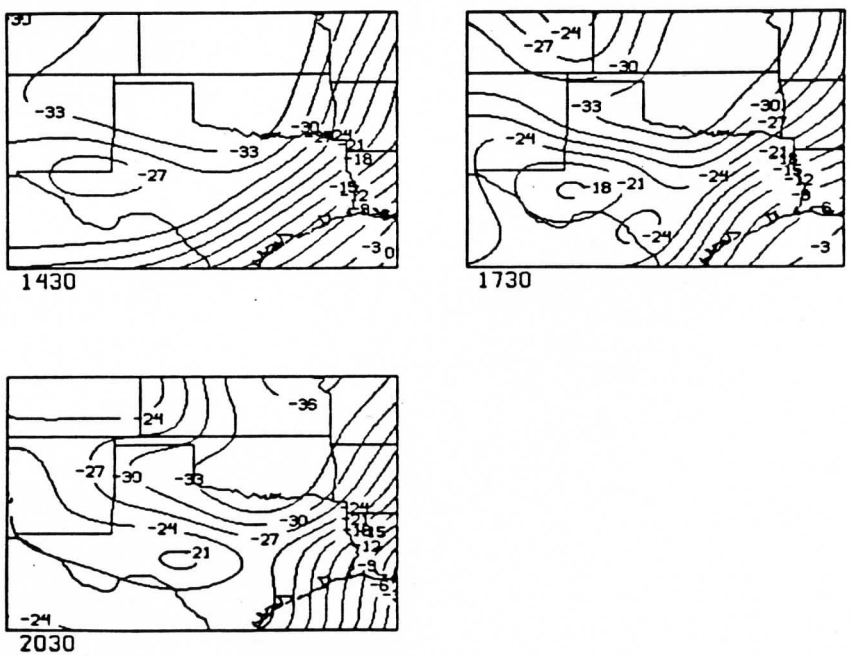

FIG. 30. As in Fig. 27, but for 700 mb dewpoint.

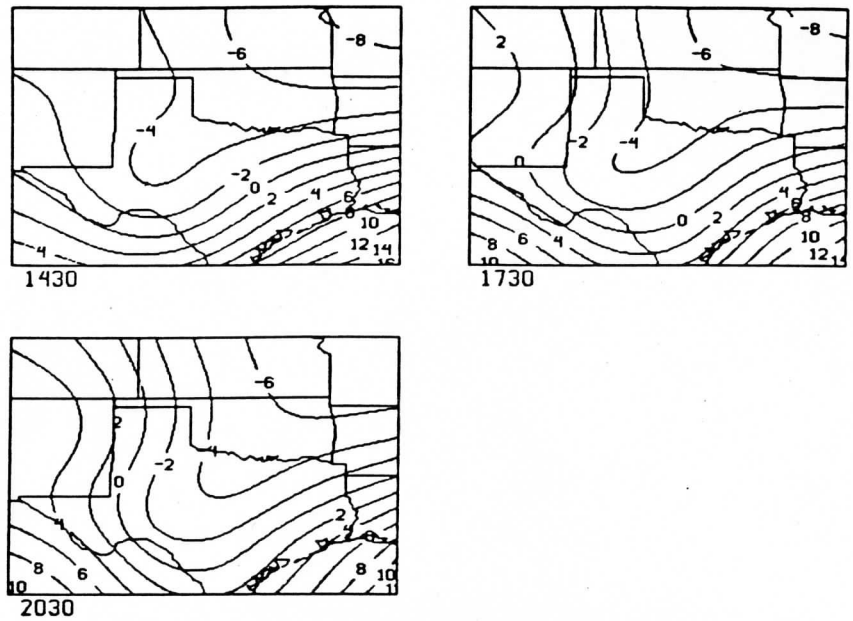

FIG. 31. The 850 mb temperature analyses (degrees Celsius) derived from the VAS retrievals initiated with the SSM estimate for 1430, 1730 and 2030 UTC 6 March 1982.

using the SSM and observed radiances, the slopes of the first estimates are significantly improved by the retrievals.

Table 3 contains the mean difference, rms difference, and the correlation between the fields just discussed. Statistics are presented comparing the first estimates (SG–LG), the retrievals (SR–LR), the retrievals versus their first estimates (SR–SG and LR–LG), and all four versus the best estimate (SG–V, LG–V, SR–V, LR–V). The numbers generally support the previous qualitative evaluation, but not very dramatically. Differences of a few tenths of a degree or 4–5 points in correlation represent what appear to the eye to be significant changes in the analyzed fields. For example, compare the LFM first estimate and the associated retrieval at 500 mb with the best estimate. The respective rms and correlation comparisons are 1.87 to 1.60 and

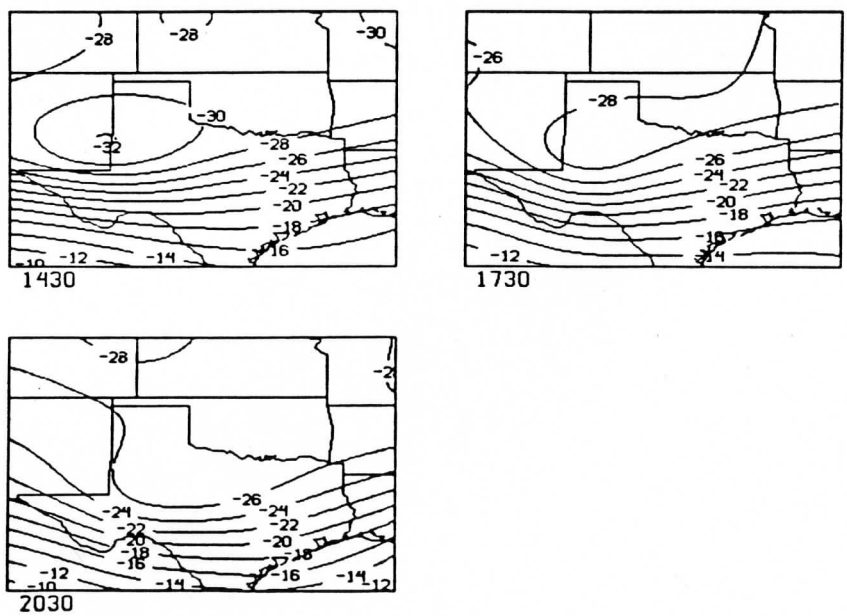

FIG. 32. As in Fig. 31, but for 500 mb temperature.

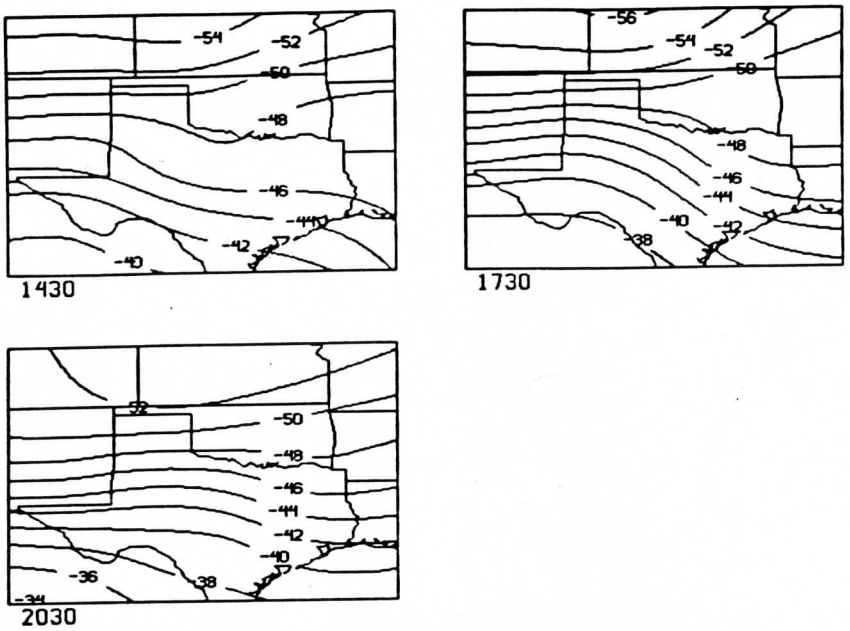

FIG. 33. As in Fig. 31, but for 300 mb temperature.

0.93 to 0.93. Yet the retrievals have qualitatively improved both the position and strength of the gradient leading the trough (Figs. 2, 20 and 28). Also at 500 mb, the statistics suggest that the retrievals have significantly degraded the SSM first estimate, yet this seems debatable (Figs. 2, 24, and 32). Some points to be drawn from Table 3 are

- The retrieved fields are more closely correlated than their respective first estimates, especially in the case of 700 mb dewpoint. It would be disquieting if this were not the case since that would suggest that the retrieval was adding a random component.
- The retrieved fields are highly correlated with their first estimates; again, less so in the case of 700 mb dewpoint.
- The retrievals generally improve on the first estimates. This is untrue for the SSM temperature at 300

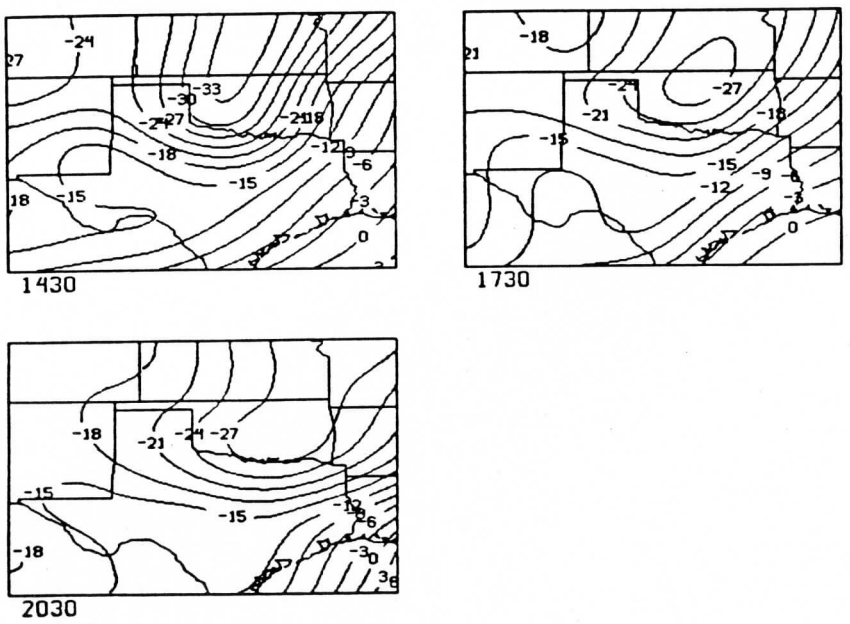

FIG. 34. As in Fig. 31, but for 700 mb dewpoint.

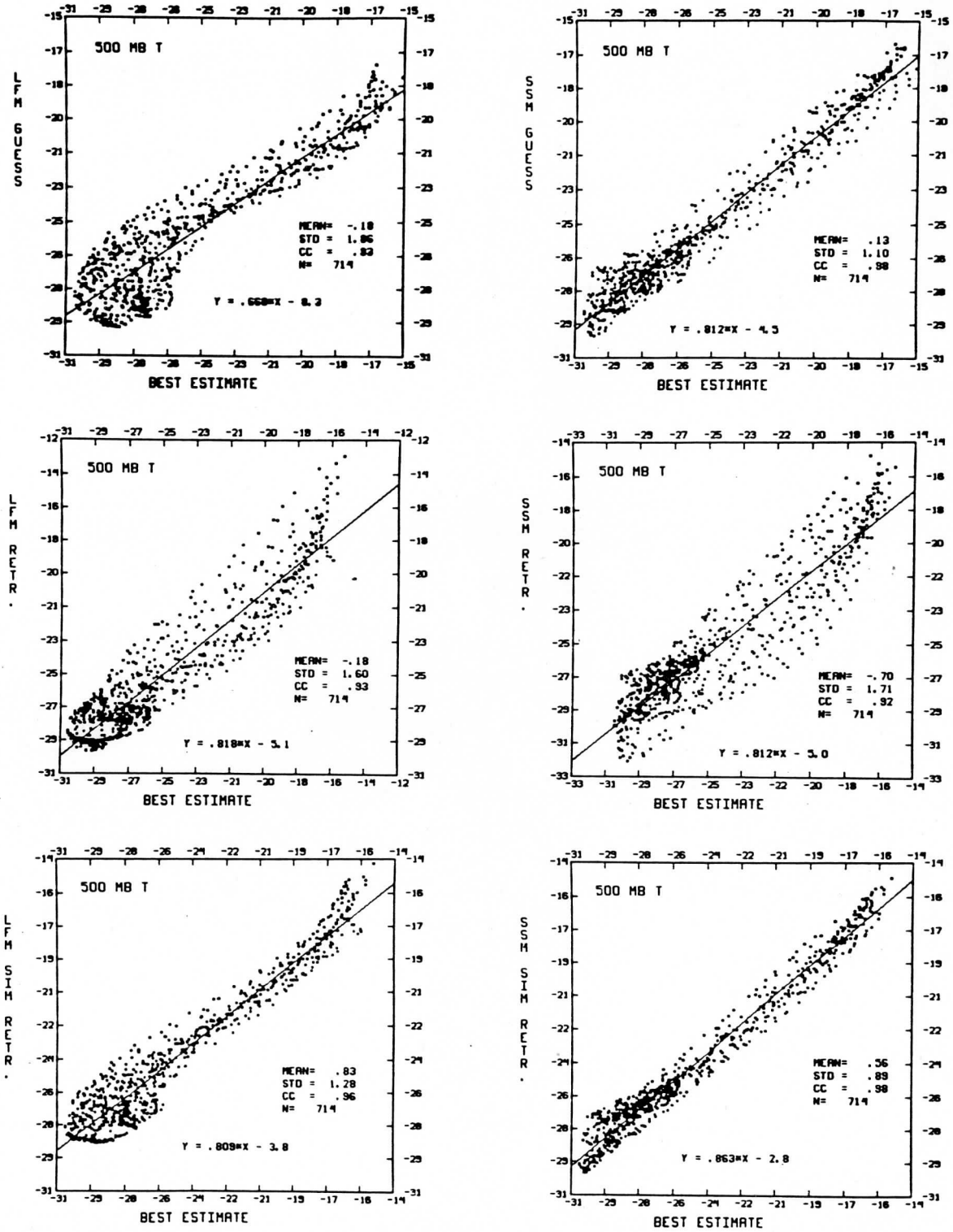

FIG. 35. Scatter diagrams of (top) LFM and SSM first estimates versus best estimates of 500 mb temperature (degrees Celeius) for 1430, 1730 and 2030 UTC 6 March 1982; (middle) retrievals from observed radiances versus best estimates; and (bottom) retrievals from simulated radiances versus best estimates. Statistics and "best-fit" regression line are shown.

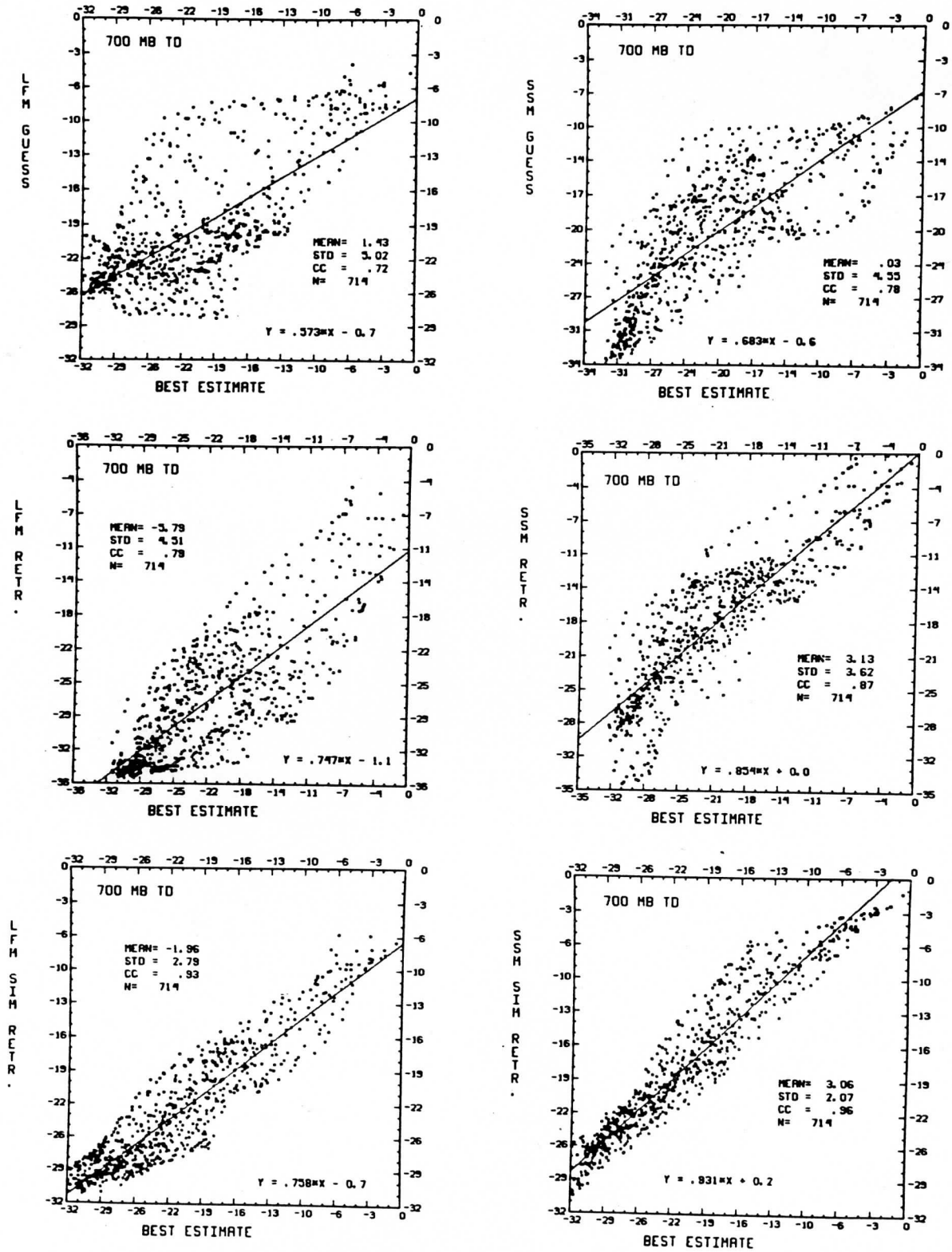

FIG. 36. As in Fig. 35, but for 700 mb dewpoint.

TABLE 3. Statistical comparisons of LFM first guess (LG), SSM first guess (SG), LFM retrieval (LR), SSM retrieval (SR), and best estimate (V). Mean and rms statistics are degrees Kelvin. The correlation of the fields is given by cc.

	850 *T*			500 *T*		
	Mean	rms	cc	Mean	rms	cc
SG–LG	0.7	1.5	.91	0.3	1.3	.94
SR–LR	0.4	1.5	.91	−0.5	1.2	.96
SG–V	0.1	1.2	.93	0.1	1.1	.98
LG–V	−0.6	1.9	.84	−0.2	1.9	.93
SR–V	0.3	1.0	.95	−0.7	1.9	.92
LR–V	−0.4	1.7	.86	−0.2	1.6	.93
LR–LG	0.2	0.6	.98	−0.0	1.3	.95
SR–SG	−0.4	1.1	.95	−0.8	1.4	.95
	300 *T*			700 *Td*		
SG–LG	1.1	1.9	.92	−1.4	4.7	.73
SR–LR	−0.6	1.6	.95	8.9	9.5	.92
SG–V	−0.1	0.9	.97	0.0	4.6	.78
LG–V	−1.2	1.9	.88	1.4	5.2	.72
SR–V	−0.1	1.1	.97	3.1	4.8	.87
LR–V	0.5	1.4	.92	−5.8	7.3	.79
LR–LG	1.7	1.8	.98	−7.2	8.8	.70
SR–SG	0.0	0.9	.98	3.1	4.6	.88

and 500 mb, but the best estimate is biased to the SSM such that the error of the SSM first estimate is unrealistically small.

- The retrievals appear statistically to have as much influence at 300 mb as at other levels. This is somewhat surprising since this part of the atmosphere is only poorly represented in the weighting functions of the "temperature" channels. This apparently reflects the importance of channel 10 for defining temperature, at least in the warmer areas (see Fig. 12).

7. Discussion

This paper has two main purposes. The first is to describe in detail the VAS retrieval algorithm on the VDUC and to investigate its sensitivity to various tuning mechanisms. The intent is to give specific examples of cause and effect so that the reader can better understand the properties of the algorithm. The second purpose is to evaluate the algorithm in a case study which has been thoroughly examined previously in order to permit comparison of the new techniques with older ones.

The principal conclusion is that the VDUC algorithm shares most of the characteristics of other retrieval methods. Results here corroborate the conclusions of Jedlovec (1985). Notably, it is not possible to systematically and significantly improve the vertical structure contained in the first guess. The horizontal structure can be enhanced, although it will retain features of the first guess. Also, large-scale biases exist which are related to the algorithm, the first guess, and the atmospheric structure. These features exist in the simultaneous algorithm just as they did in the algorithms examined by Jedlovec. There is good indication that the simultaneous algorithm provides better information on the moisture, as has been reported for retrievals obtained from the polar orbiting satellites (Smith et al. 1985b) but statistics obtained for temperature retrievals are very similar.

Since 6 yr of experience and algorithm development have not significantly changed the characteristics of VAS retrievals, questions linger as to their utility. Suspicion is likely heightened by results presented here demonstrating that solutions are sensitive to rather subtle changes in the method. However, an understanding of the limitations is the first step to useful application of the satellite data. In the case of the VAS and the VDUC, it is important to emphasize that the principal products are quasi-continuous descriptions of the evolution of the meteorology, both as gridded fields and as images. A body of literature attests to this role (e.g., Chesters et al. 1983; Smith et al. 1985a; Robinson et al. 1986; and Mostek et al. 1986; among others). In this application, the important factors are to process the soundings in as consistent a manner as possible and to use the best first guess available. A significant feature shown in the present study is that the satellite retrievals will improve the initial estimate even though they retain a part of the error of the estimate.

If the VAS data are to be used to initialize forecast models (e.g., O'Lenic et al. 1986), other processing considerations may apply. For this application, the practice of using a numerical forecast for a first guess is quite controversial, because the error of the sounding is correlated with the errors of the numerical models. Such correlated error is difficult to treat in the statistical analysis schemes which are in wide use at forecasting centers. The desire to avoid correlated error has been the driving force behind the continued use of statistical algorithms for operational retrievals. Statistical retrievals do not have the correlated error and there is as yet no convincing evidence that they are less accurate than physical retrievals, especially if the dependent datasets are carefully selected (Lee et al. 1983). Physical methods will eventually prevail since the capability of improving the first estimate is bounded only by limitations in the measurements and errors in the physics; the latter can, in principle, be corrected. The statistical approach suffers the same limitation of measurement, and also the inherent problem that the statistics will always be unrepresentative to some degree. Ultimately, the physical retrieval which "nudges" the model will emerge as part of a complete data assimilation system. Until that day, however, we must live with the correlated error of the VDUC algorithm, or change that algorithm to generate truly independent soundings for numerical weather prediction.

The characteristic of satellite retrievals which historically has most damaged their credibility is the "bias" problem. The underlying cause is not well understood,

but certainly the low vertical resolution of the measurement is a prime contributor. The problem is especially grievous with the VAS because of the limited number of channels and the difficulties in calibration. The bias problem will be with us at least until high spectral resolution measurements can be achieved from space. GOES-NEXT, scheduled for late 1989, has additional channels which will help, but the fundamental deficiency will remain. For VDUC, the bias will be alleviated by introducing empirical factors to tune the algorithm for a given situation. This approach is satisfactory for the primary application of the data, but it increases first guess dependence and is unattractive for the production of soundings for model input. For the near future, the modelers will have to devise techniques to compensate. Progress is being made in this area as exhibited by the work of Gal-Chen et al. (1986). They have shown good success in marrying the model with VAS retrievals, paying attention to the known limitations of the latter. Also, Cram and Kaplan (1985), and Diak (1986) have used the horizontal gradients instead of the absolute magnitudes of the retrievals to minimize bias effects.

Acknowledgments. A large number of people have been involved in the evolution of the VAS temperature and moisture retrievals. CIMSS members deserving of special note are Bill Smith for the major share of algorithm development; Hal Woolf for algorithm implementation; Paul Menzel for watchdogging the instrument and the schedules; Tony Siebers, Roney Sorensen, Gary Wade, Chris Velden and Tony Schreiner for exercising the system and contributing to improvements. Scientists too numerous to name individually at other institutions—Goddard Space Flight Center, Marshall Space Flight Center, PROFS, CIRA, and the National Weather Service Centers in Suitland, Kansas City, and Miami—have also contributed significantly. The support staff for the McIDAS merit recognition for keeping the system relatively amicable during the VAS assessment. Finally, a number of critical reviewers have contributed substantially, as has Laura Beckett in preparing this manuscript many times.

REFERENCES

Chesters, D., L. W. Uccellini and W. D. Robinson, 1983: Low-level water vapor fields from the VISSR Atmospheric Sounder (VAS) "split window" channels. *J. Clim. Appl. Meteor.*, **22**, 725–743.

Cram, J. M., and M. L. Kaplan, 1985: Variational assimilation of VAS data into a mesoscale model: assimilation method and sensitivity experiments. *Mon. Wea. Rev.*, **113**, 467–484.

Diak, G., 1986: Assimilation of scalar versus horizontal gradient information from the VAS into a mesoscale model. *J. Clim. Appl. Meteor.*, **26**, 738–748.

Dodge, J., J. R. Greaves and H. E. Montgomery, 1985: AVE/VAS ground truth experiment. VAS Demonstration (VISSR Atmospheric Sounder) Description and Final Report. H. E. Montgomery and L. W. Uccellini, Eds. NASA RP-1151 [NTIS 86N1386], 50–54.

Fleming, H. E., D. S. Crosby and A. C. Neuendorffer, 1986: Correction of satellite temperature retrieval errors due to errors in atmospheric transmittances. *J. Clim. Appl. Meteor.*, **25**, 869–882.

Fuelberg, H. E., and P. J. Meyer, 1986: An analysis of mesoscale VAS retrievals using statistical structure functions. *J. Clim. Appl. Meteor.*, **25**, 59–76.

Gal-Chen, T., B. D. Schmidt and L. W. Uccellini, 1986: Simulation experiments for testing the assimilation of geostationary satellite temperature retrievals into a numerical prediction model. *Mon. Wea. Rev.*, **114**, 1213–1230.

Hayden, C. M., and R. J. Purser, 1986: Applications of a recursive filter, objective analysis in the processing and presentation of VAS data. Preprint 6th Conference on Atmospheric Radiation, Williamsburg, American Meteorological Society, 82–87.

Hill, C. K., and R. E. Turner, 1983: NASA's AVE/VAS Program. *Bull. Amer. Meteor. Soc.*, **64**, 796–797.

Jedlovec, G. J., 1985: An evaluation and comparison of vertical profile data from the VISSR Atmospheric Sounder (VAS). *J. Atmos. Oceanic Tech.*, **2**, 559–581.

Lee, T., D. Chesters and A. Mostek, 1983: The impact of conventional surface data upon VAS regression retrievals in the lower troposphere. *J. Clim. Appl. Meteor.*, **22**, 1853–1874.

McMillin, L. M., and D. S. Crosby, 1984: Theory and validation of the multiple window sea surface temperature technique. *J. Geophys. Res.*, **89**(C3), 3655–3661.

Menzel, W. P., T. A. Achtor, C. M. Hayden and W. L. Smith, 1984: The advantages of sounding with the smaller detectors of the VISSR Atmospheric Sounder. NOAA Technical Memorandum NESDIS 6, U.S. Department of Commerce, Washington, DC, 22 pp.

Mostek, A., L. W. Uccellini and D. Chesters, 1986: Assessment of VAS soundings in the analysis of a preconvective environment. *Mon. Wea. Rev.*, **114**, 62–87.

O'Lenic, E., 1986: The effect of VISSR Atmospheric Sounder (VAS) data on some LFM analyses and forecasts. *Mon. Wea. Rev.*, **114**, 62–87.

Robinson, W. D., D. Chesters and L. W. Uccellini, 1986: Optimized retrievals of precipitable water fields from combinations of VAS and conventional surface observations. *J. Geophys. Res.*, **91**(D4), 5305–5318.

Schlatter, T. W., 1981: An assessment of operational TIROS-N temperature retrievals over the United States. *Mon. Wea. Rev.*, **109**, 110–119.

Smith, W. L., V. E. Suomi, W. P. Menzel, H. M. Woolf, L. A. Sromovsky, H. E. Revercomb, C. M. Hayden, D. N. Erickson and F. R. Mosher, 1981: First sounding results from VAS-D. *Bull. Amer. Meteor. Soc.*, **62**, 232–236.

——, G. S. Wade and H. M. Woolf, 1985a: Combined atmospheric sounding/cloud imagery—a new forecasting tool. *Bull. Amer. Meteor. Soc.*, **66**, 138–141.

——, H. M. Woolf and A. J. Schreiner, 1985b: Simultaneous retrieval of surface atmospheric parameters: a physical and analytically direct approach. *Advances in Remote Sensing*, A. Deepak, H. E. Fleming and M. T. Chahine (Eds.), A. Deepak Pub. ISBN 0-937194-07-7, 221–232.

Susskind, J., J. Rosenfield, D. Reuter and M. T. Chahine, 1984: Remote sensing of weather and climate parameters for HIRS2/MSU on TIROS-N. *J. Geophys. Res.*, **89**, 4677–4697.

Weinreb, M. P., H. E. Fleming, L. M. McMillin and A. C. Neuendorffer, 1981: Transmittances for the TIROS Operational Vertical Sounder. NOAA Tech. Rpt. NESS 85, Washington, DC, 60 pp.

SATELLITE CLOUD COMPOSITE CLIMATOLOGIES:

A NEW HIGH-RESOLUTION TOOL IN ATMOSPHERIC RESEARCH AND FORECASTING

Donald L. Reinke
Cynthia L. Combs[1]
Stanley Q. Kidder[1]
Thomas H. Vonder Haar[2]

METSAT, Inc.
Fort Collins, CO 80521

---

[1] Present affiliation, University of Alabama - Huntsville

[2] Principal affiliation, Colorado State University

ABSTRACT

GOES digital imagery has been collected and processed using new techniques over portions of the U.S. since March, 1988. High spatial and temporal resolution satellite cloud composite climatologies (SCCCs) have been produced which represent cloud freqiuency maps for each season. For each month studied, the cloud composite products represent the cloud occurrence frequency for each GOES pixel location and depict the overall spatial distribution of cloud cover over large portions of the United States.

The satellite composites present a new cloud climatology at a greater spatial and temporal resolution than previously available. Composites with ground resolutions of 2.5 km at hourly time intervals show striking patterns of cloud cover that are not detected in pre-existing cloud climatologies.

A comparison between the SCCCs and climatologies produced from conventional surface observations is presented. The comparison is quite good for most stations yet some significant differences are noted and discussed. Cloud occurrence in the vast areas between surface observing sites can now be analyzed using the new SCCC tool.

1. Introduction

> I've looked at clouds from both sides now,
> From up and down, and still, somehow,
> It's clouds' illusions I recall;
> I really don't know clouds ... at all.
>
> --Lyrics from "Both Sides Now"

Unfortunately, true. We have observed clouds from the surface for hundreds of years and from space for thirty years. Yet we still do not know exactly how many clouds there are, how big they are, how long they last, what their radiative properties are, the interannual variability of these cloud parameters, or requisite quantitative details on how they affect the earth's weather and climate. Fortunately, in the last decade or so, a great deal of effort has been expended to begin answering these questions using satellite data. The purpose of this paper is to describe a new high-resolution space/time satellite cloud composite climatology (SCCC) designed to address the small-scale variation of clouds.

Hughes (1984) presents a good historical background on the production of cloud climatologies. At large scales, two projects stand out. The International Satellite Cloud Climatology Project (ISCCP) (Paltridge and Vonder Haar, 1979; Schiffer, 1982; Schiffer and Rossow, 1983/1985; Rossow and Schiffer, 1991) is determining cloud cover, cloud height and other cloud properties using visible and infrared satellite data at a resolution of approximately 250 x 250 km. The project, involving a system of 5 to 7 satellites, began in 1983 and is planned to continue through 1995. The Earth Radiation Budget Experiment (ERBE), onboard the Earth Radiation Budget Satellite (ERBS) and on NOAA 9 and 10 satellites, determines mean radiative parameters in cloudy conditions as well as clear-sky parameters.

Since clouds are the single most important difference between mean and clear conditions, the cloud forcing, or the change in net radiation due to clouds, can be determined. For example, Ramanathan et al. (1989) have concluded that, globally averaged, clouds cooled the earth in April, 1985. ERBE, together with various cloud climatologies, and local area process studies will eventually reveal much information on large-scale cloud forcing.

At medium spatial scales, the U.S. Air Force has constructed and used a nephanalysis, currently the Real-Time Nephanalysis or RTNEPH (Kiess and Cox, 1988), for operational purposes. Satellite and surface observations are used in forming the data base, and its grid resolution is 43 km. Cloud climatologies have been constructed from these data (Hughes and Henderson-Sellers, 1985). Satellite data have considerably finer resolution than 43 km, however, and clouds also vary on finer scales. We believe that this very fine scale space/time domain is crucial to understanding clouds, their forcing by terrain, their effect on mesoscale processes, and their relationship to larger scales.

The highest resolution cloud climatologies presented and described in this paper are constructed by compositing hourly GOES images. The spatial resolution of the satellite data, up to 1 km for GOES visible imagery (Clark, 1983), determines the resulting resolution of the composite. For the climatologies presented here, image data was remapped into a mercator projection with dimensions of 860 rows by 1000 columns. This size was chosen to enable us to display the images at full image resolution (one pixel per data point) on our display device. We can then view a little

more than one-third of the continental U.S. at a resolution of 2.5 km. For comparison, this is two orders of magnitude higher linear resolution than the nominal ISCCP resolution of 280 km (four orders higher in areal resolution).

2. Project Background

The first cloud composites for research were constructed by sequentially superimposing satellite images on the same piece of photographic paper (Kornfield et al., 1967). These first "multiple exposure" cloud composites provided considerable information about large-scale cloud systems in the general circulation of the atmosphere. They were not used extensively for studies of small-scale clouds.

Klitch (1982), Kelly (1983) and Weaver and Kelly (1982) improved the photo-averaging techniques by digitizing hardcopy photographs and then producing a digital composite image. Their studies concentrated on mesoscale cloud systems and medium scale topographic effects.

The greatest advance in cloud compositing in the last 10 years was introduced by Klitch et al. (1985). They constructed cloud composites entirely in the digital domain. Digital GOES images collected at the Colorado State University Satellite Earthstation were processed to remove registration (navigation) problems and digitally composited by selecting a threshold brightness to discriminate cloudy from cloud-free areas. Data for Colorado and surrounding states for several summer months were examined. They found a close coupling between terrain, particularly terrain slope, and cloud formation, and interesting details in the diurnal

convection cycle were revealed. Gibson and Vonder Haar (1990) recently completed a similar study of the southeastern states using cloud compositing which revealed intricate patterns of cloud development near the coasts. Weaver et al. (1987) and Kelly (1983) and Kelly et al. (1989) refined the cloud compositing technique to that used in this study and applied the results to short-range forecasting.

3. Cloud Compositing Procedure

Producing a cloud composite climatology is conceptually simple but operationally time consuming. Each pixel in each image to be composited is classified as either clear or cloudy; then the frequency of occurrence of cloud at the pixel location is calculated as the fraction of the pixels which were classified as cloudy during the composite period. Figures 1-4 illustrate this process.

Figure 1 shows a typical GOES visible image of the western U.S. This image was taken by GOES-7 from geostationary altitude (35,790 km) over the equator at 98 degrees W longitude. We used visible radiance data to achieve the highest possible resolution.

Using such high resolution data poses some problems which can be overlooked at global scales (>200 km). Because the navigation parameters for each GOES image can be in error, each image must be checked by comparison with landmarks to see whether it was properly navigated. We have found that errors of only a few km will produce over or underestimates of cloud cover by as much as 80% over areas with a sharp contrast gradient such as land/water boundaries. Those images that are found to be

mis-navigated are adjusted until the landmarks match as closely as possible. (We are currently evaluating an automated alignment routine which will eliminate much of the time consumed in this step.) The images are mapped into a standard map projection prior to being aligned (Mercator in the present study).

A "background" image is constructed for each time period being composited. The background image represents the cloud-free brightness count detected by the satellite, i.e. the cloud-free scene of the Earth's surface. Because variations in sun angle and surface composition produce changes in background brightness, (Minnus and Harrison, 1984) a different background image must be constructed for each observing time and is used only for a fraction of a year. We constructed a background image for each hour of the day and for a one month period. Figure 2 is a background image for 2100 UTC, September, 1989, representing the cloud-free scene for that specific hour and month. A minimum-value analysis was used to construct the background image, based on the assumption that the darkest (warmest) pixel during the month will represent the cloud-free radiance at that location.

Next, each pixel must be classified as either clear or cloudy. This is done by comparing the pixel brightness of each raw image with the background brightness image for that same time. Those pixels which are more than a specified number of counts brighter than the background are classified as cloudy. Figure 3 shows the resultant cloudy/clear image produced from Figure 1. We selected nine GOES visible brightness counts as the optimum threshold based on work done by Rossow et al. (1985). That is,

pixels that are nine counts higher than the background are classified as cloudy. The cloud discrimination technique has difficulty with thin clouds and with clouds over very bright backgrounds, as do virtually all cloud discrimination algorithms.

Finally, the monthly satellite cloud composite climatology (SCCC) is constructed from the daily cloud/clear images. This process involves a simple computation of the number of days during the month that each pixel was classified as cloudy. Figure 4 shows a completed cloud frequency composite. The colors represent the frequency of occurrence of cloud (0-100%) at that time (2100 UTC) during the month of September, 1989. To date, cloud composite climatologies have been produced over the U.S. west of the Mississippi for the months of March (1988-1990), July (1988-1990), September (1988-1990) and December (1989). In addition, a full U.S. composite was produced during April, 1989. Figures 8-11 show a sequence of composites from July, 1988 at 1500 UTC, 1800 UTC, 2100 UTC and 0000 UTC. Note the diurnal "explosion" of cloudiness over the mountains in the west.

4. Intercomparison With Surface-Based Observations

The new satellite cloud composite climatologies were compared with ground-based cloud observations. To our knowledge, this is the first time a comparison between satellite and surface cloud observations has been made in this manner. Data from over 250 surface stations were obtained from the National Center for Atmospheric Research (NCAR) and were composited for the months of July, 1988, September, 1988 and March, 1989. Images shown in Figures 5-7 were used in the comparison for July, 1988 for the hour of 1500 UTC. The figures contain: (5) the satellite cloud composite climatology,

(6) the frequency of occurrence from surface observations (the circles are 50 km in radius plotted on the satellite image projection), and (7) the absolute difference between the satellite-derived frequency and the surface observation-derived frequency.

The frequency of occurrence of cloud from surface observations was determined by assigning a cloud/no cloud value for a specific hour of each day. If a station reported 5/8 or more of opaque cloud it was considered cloudy. The satellite frequency was computed by averaging all of the composite pixels (from Figure 5) within a 50 km diameter circle about the geographic locations of the surface observation site. This distance was selected to approximate the surface observer's "sky dome," which is the imaginary hemisphere that the observer reports to be obscured by cloud.

Several observations may be made from the comparison between SCCCs and surface observation-based cloud frequencies:

a) The satellite data are vastly superior to the surface data in revealing spatial details. The relative minimum cloudiness in the Snake River Valley of Idaho and the relative maximum over the central and southern Rocky Mountains are only suggested by the surface data (Figure 5); they are dramatically portrayed in the satellite composite (Figure 6). The general pattern of cloudiness is certainly evident in the composite made from surface reports, but not to the detail shown in the satellite composites (note the "empty spaces" in the surface composite shown in Figure 6).

The increased resolution allows us to depict the striking effects of topography on the diurnal cycle of cloudiness, and the sharp gradients in frequency of occurrence of cloud that are associated with topographic boundaries such as mountains and coastlines. Figures 8-11 show a sequence of SCCCs from July, 1988 at 1500, 1800, 2100 and 0000 UTC. Note the diurnal explosion of cloudiness over the southern Rocky Mountains in contrast with a general decrease in cloudiness over the Pacific Northwest. The stratus/stratocumulus clouds over western Washington and Oregon are dissipated by the same heating that generates cloud cover over the Rocky Mountains. The 1500 UTC image (Figure 8) shows how the atmosphere has stabilized during the nighttime hours with frequencies generally less than 30% over the central and southern Rockies. Contrast that with the dramatic increase in cloud cover at 1800 and 2100 UTC (Figures 9 and 10), and the large expanse of cloudiness (most likely due to the tops of cumulonimbus spreading over large geographic areas) by 0000 UTC (Figure 11). Note also the sharp gradient in frequency that exists along the California coast and between the mountains and southwestern deserts in Arizona.

b) Some of the largest differences between the satellite and surface observation-derived frequencies occur in areas of high cloud cover gradient, such as the coastal area of southern California. Figure 12 shows a blow-up of two 50 km circles taken from the July, 1988 UTC satellite cloud composite climatologies (extracted from the image in Figure 5). Note the

strong gradient across both circles, with values ranging from a frequency of <10% (blue) to >90% (red). The left circle represents the SCCC centered on San Diego, California, and the right circle is centered on Oceanside, California. The surface observations from San Diego produce a frequency of occurrence of cloud of 96% while the SCCC frequency was 71%. This is most likely due to the fact that low stratiform overcast conditions are common over the observation site, and the view of clear skies several miles inland was obscured by cloud cover. These blow-ups highlight the increased spatial resolution that can be obtained from the satellite cloud observations. The mean cloud frequency from surface observations will not identify the sharp boundaries between cloudy or clear conditions occurring within the station circle. Elimination of these areas of sharp gradient from our sample set produces even better agreement between the satellite and surface observation-derived composites.

c) The satellite cloud frequencies generally compare well with surface observations on a site basis. Figure 13 is a scatter plot of the satellite vs. surface frequencies. Note that the surface observations consistently show a somewhat higher frequency of occurrence of cloud than do satellite observations. This same feature, discussed by Henderson-Sellers and McGuffie (1990), is due, in part, to the tendency for overestimation of cloud amounts by ground-based observers when looking at the sky dome at increasingly large angles from

local zenith. Figure 13 includes all surface stations that reported at least 15 days during the month.

Table 1 shows comparison statistics between the surface-observed and satellite-observed frequency of occurrence of cloud. The mean absolute difference between surface and satellite-derived frequencies was consistently less than 20% (except for March, 1989) and during the months of July and September, was less than 10%. The mean frequency, shown in Table 1, is the mean of all reporting sites. The mean difference is based on absolute differences, and the correlation coefficient is based on the first order regression line shown in Figure 13 (solid line). The statistics shown in Table 1 are based on the comparison of only those synoptic stations for which reports were available to match each satellite image used in the composite.

An item of interest is the mean frequency of occurrence of cloud. The values shown in Table 1 are taken from synoptic observation sites only, and represent the mean frequency of occurrence that would be determined from historical surface observations of cloud. Table 1 values indicate that the mean frequency of occurrence of cloud in July, 1988 decreased between 1500 UTC and 0000 UTC (from 30.0 to 27.5 for surface-based frequencies and from 24.1 to 23.2 for satellite). One would conclude from these numbers (taken from samples at synoptic reporting sites only) that there is a net decrease in cloud occurrence from 1500 to 0000 UTC. The satellite image shows clearly that there is in fact a dramatic overall increase (see Figures 8 and 11). When we produce the mean frequency of occurrence of cloud from the satellite composites, by averaging each 2.5 km

resolution data point, we obtain a mean of 23.3 at 1500 UTC and a mean of 28.9 at 0000 UTC. We believe this to be more representative of the diurnal change in cloudiness than the historical surface reports would indicate.

To test our comparison we included a composite image that was known to be unreliable. Because of the low sun angle, the 1500 UTC satellite images from March are dark over the western third of the image. We constructed a composite for March, 1989 of 1500 UTC and compared it with the surface observation-derived frequencies. As can be seen from Table 1 the comparison was very poor, and additionally the "difference" image (not shown here) identified the regions of unreliable data.

5. Applications of High-Resolution Composites

We envision a number of applications of the digital cloud composites. One is the relationship between cloud occurrence and the terrain (see also Gibson and Vonder Haar, 1990). The primary areas of interest are land/water boundaries and mountainous terrain. A second question involves the joint correlation between two or more station locations or geographic regions. For example, four stations may have a frequency of occurrence of cloud of 50%. What is the probability that at a given time all stations will be cloudy or conversely clear.

Another application is in "conditional" cloud climatologies (Reinke et al., 1990a). For example, suppose that it is cloudy at 1500 UTC. What is the probability that it will be cloudy at that location at 1800 or 2100 UTC? What is the probability that it will be cloudy if it is initially clear? These questions can be answered with high-resolution cloud

composite data.

Still another area of interest is to examine how the cloud frequencies vary in time. This comparison can be done on a daily basis (derived variation as shown in Figures 8-11) to study cloud or cloud system "life cycles" or by looking at the interannual or seasonal variation of cloudiness (Reinke et al., 1990b).

Finally, we suggest that regional and local cloud climatologies will complement global-scale satellite-derived cloud frequencies such as ISSCP. Both cloud data sets are needed for application to initialization/validation of numerical models. Climate diagnostic and cloud/radiation process studies definitely present questions which demand the highest resolution climatologies.

6. Conclusions

Satellite cloud composite climatologies (SCCC) provide information on high space and time variation of clouds that is not presently available by other means. Satellite composites can be used in applications which have previously relied on cloud information derived from surface observations. The new satellite composites provide a higher spatial resolution adequate temporal coverage and are more representative of the distribution of cloud cover.

High-resolution satellite cloud composite climatologies will greatly improve our overall knowledge of clouds and their effect on the earth's climate. This is a primary objective of the U.S. Global Change Research Program. Research lines of inquiry which couple this new information on

high frequency cloud occurrence with our new knowledge of small-scale dynamics and thermodynamic processes will allow better overall understanding of the complex linkage between persistently cloudy (and cloud-free) regions and local weather features.

7. Acknowledgments

We would like to acknowledge Dr. Frank Kelly and Mr. C.F. Shih for their invaluable assistance in the development of the algorithms required to process the images used in construction of the composites and Dr. Ed Tomlinson for his imagination and technical assistance throughout the initial phases of the high-resolution cloud climatology project. Also thanks to Julie Smith for her expert preparation of this manuscript. Data collection and processing for the initial phase of this project were sponsored by the Office of Naval Research (Contract #N00014-86-C-0463) with the most recent work being sponsored by the Air Force Geophysics Laboratory (Contract #F19628-89-C-0083).

8. References

Clark, J.D., 1983: The GOES User's Guide. U.S. Department of Comm., 90 pps.

Gibson, H.M. and T.H. Vonder Haar, 1990: Cloud and convection frequency over the S.E. U.S. as related to small-scale geographic features. Monthly Wea. Review, 118, 2215-2227.

Henderson-Sellers, A. and K. McGuffie, 1990: Are cloud amounts estimated from satellite sensor and conventional surface-based observations related? Remote sensing letters, Int. J. of Remote Sensing, 1990, Vol. 11, No. 3, 543-550.

Hughes, N.A., 1984: Global cloud climatologies: A historical review. J. Climate Appl. Meteor., 23, 724-751.

Hughes, N.A. and A. Henderson-Sellers, 1985: Global 3D-Nephanalysis of Total Cloud Amount: Climatology for 1979. Climate Appl. Meteor., 24, 669-686.

Kelly, F.P., 1983: An extreme event forecast guidance method using satellite cumulus cloud climatologies. MS thesis, Colorado State University, Department of Atmospheric Science, Fort Collins, CO.

Kelly, F.P., T.H. Vonder Haar and P.W. Mielke, Jr., 1989: Imagery randomized block analysis (IRBA) applied to the verification of cloud edge detectors, J. Atmos. Oceanic Tech., 6, 671-679.

Kiess, R.B. and W.M. Cox, 1988: The AFGWC automated real-time analysis model. AFGWC/TN-88/001, AFGWC, Air Weather Service (MAC), Offutt AFB, NE, 82 pp.

Klitch, M.A., 1982: Compositing digital satellite data to detect regions of orographically induced convection on the northern high plains. Colorado State University, M.S. thesis, Department of Atmospheric Science, Paper No. 351.

Klitch, M.A., J.F. Weaver, F.P. Kelly and T.H. Vonder Haar, 1985: Convective cloud climatologies constructed from satellite imagery. Mon. Wea. Rev., 113, 326-337.

Kornfield, J., A. Hasler, K. Hanson and V. Suomi, 1967: Photographic cloud climatology from ESSA III and V computer produced mosaics. Bull. Amer. Meteor. Soc., 48, 878-883.

Minnis, P. and E.F. Harrison, 1984: Diurnal variability of regional cloud and surface radiative parameters derived from GOES data. Part I: Analysis method, Part II: Cloud results. J. Climate Appl. Meteor., 23, 993-1031.

Paltridge, G. and T.H. Vonder Haar, 1979: Plan for implementation of a real-time satellite observed cloud climatology project. Report for JOC for Climate Dynamics Sub-programme of GARP, ICSU/WMO, Geneva.

Ramanthan, V., B.R. Barkstrom and E.F. Harrison, 1989: Climate and the Earth's Radiation Budget. Physics Today, May 1989, 22-32.

Reinke, D.L., C.L. Combs, E.M. Tomlinson and T.H. Vonder Haar, 1990a: Persistence forecasts from high-resolution cloud composite climatologies. Poster presentation at the Cloud Impacts on DoD Systems Conference, Monterey, CA, January 9-11, 1990.

Reinke, D.L., C.L. Combs, E.M. Tomlinson and T.H. Vonder Haar, 1990b: Interannual variability in cloud frequency as determined from GOES satellite. Presented at the Cloud Impacts on DoD Systems Conference, Monterey, CA, January 9-11, 1990.

Rossow, W.B. et al., 1985: ISSCP cloud algorithm intercomparison. J. Climate Appl. Meteor., 24, 877-903.

Rossow, W.B. and R.A. Schiffer, 1991: ISCCP Cloud Data Products. Bull. Amer. Meteor. Soc., 72, 2-20.

Schiffer, R.A., 1982: The International Satellite Cloud Climatology Project (ISCCP), preliminary implementation plan. WCP-35, WMO, Geneva, 77 pp.

Schiffer, R.A. and W.B. Rossow, 1983: The International Satellite Cloud Climatology Project (ISCCP), the first project of the World Climate Research Program. Bull. Amer. Meteor. Soc., 64, 779-784.

Schiffer, R.A. and W.B. Rossow, 1985: ISCCP global radiance data set: A new resource for climate research. Bull. Amer. Meteor. Soc., 66, 1498-1505.

Weaver, J.F. and F.P. Kelly, 1982: A mesoscale, climatologically-based forecast technique for Colorado. Preprints: Ninth Conference on Weather Forecasting and Analysis, American Meteorological Society, Boston, 277-280.

Weaver, J.F., F.P. Kelly, M. Klitch and T.H. Vonder Haar, 1987: Cloud climatologies constructed from satellite imagery. Preprints: Third Systems for Meteorology, Oceanography and Hydrology, American Meteorological Society, Boston, 169-172.

LIST OF FIGURE CAPTIONS

Figure 1. GOES-East visible image for September 15, 1989, 2100 UTC.

Figure 2. Background image for 2100 UTC, September 1989.

Figure 3. Cloud/no cloud image for September 15, 1989, 2100 UTC.

Figure 4. Cloud frequency composite for 2100 UTC, September 1989.

Figure 5. Cloud frequency composite from the GOES satellite for July 1988, 1500 UTC. Image resolution is approximately 2.5 km per pixel.

Figure 6. Cloud frequency composite from surface observations for July 1988, 1500 UTC. Circles represent a 50 km diameter centered on the reporting station.

Figure 7. Difference image. Colors represent the ABSOLUTE difference (in percent cloud cover) between the satellite-derived cloud frequency and the frequency computed from surface observations (July 1988, 1500Z).

Figure 8. Cloud frequency composite from the GOES satellite for July 1988, 1500 UTC. Image resolution is approximately 2.5 km per pixel.

Figure 9. Cloud frequency composite from the GOES satellite for July 1988, 1800 UTC.

Figure 10. Cloud frequency composite from the GOES satellite for July 1988, 2100 UTC.

Figure 11. Cloud frequency composite from the GOES satellite for July 1988, 0000 UTC.

Figure 12. Blow-up of two 50 km diameter circles from the satellite cloud frequency composite for July 1988, 1500 UTC. Circles represent satellite-derived cloud frequencies for San Diego (left), and Oceanside (right), California.

Figure 13. Scatter plot of satellite-derived cloud frequencies vs. frequencies from surface observations for data from July 1988 at 1500 UTC. The dashed line represents the first order regression line. Only stations which reported every day of the month are plotted.

Figure 14. Scatter plot of satellite-derived cloud frequencies vs. frequencies from surface observations for data from July 1988 at 1500 UTC. This plot is for all stations which reported at least 15 days during the month.

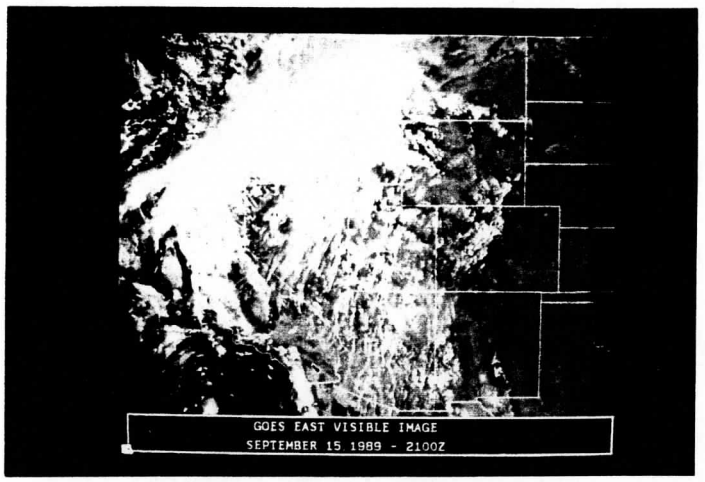

FIGURE 1

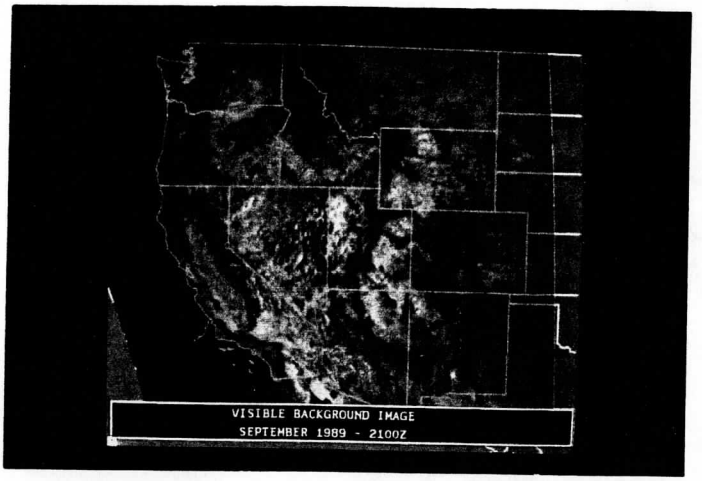

FIGURE 2

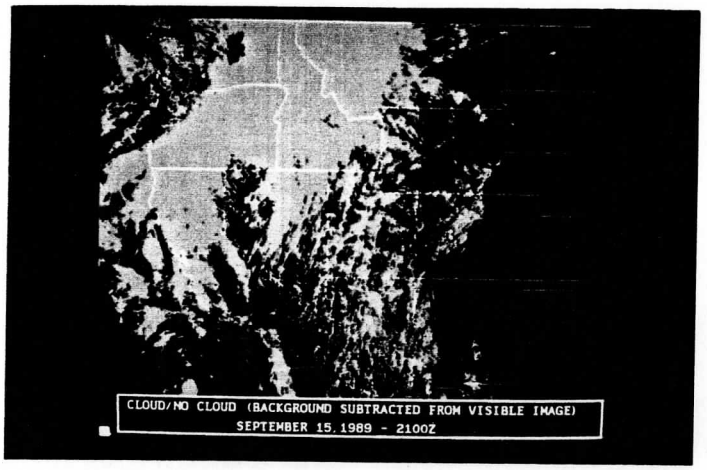

FIGURE 3

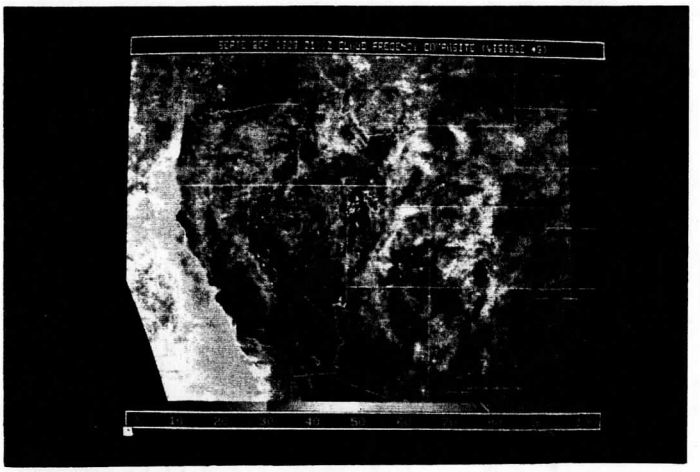

FIGURE 4

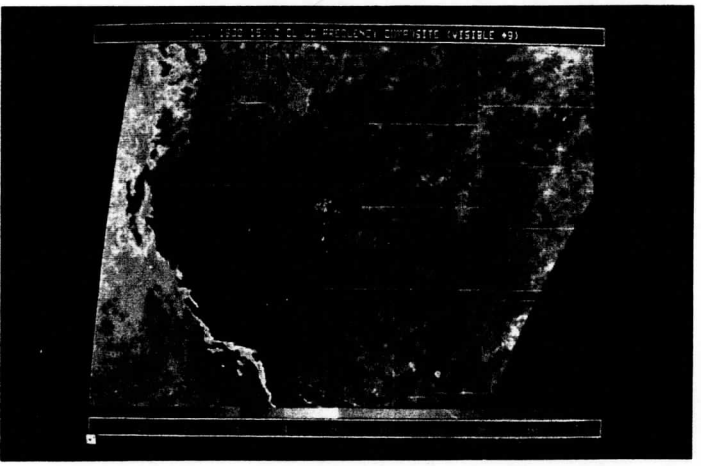

FIGURE 5

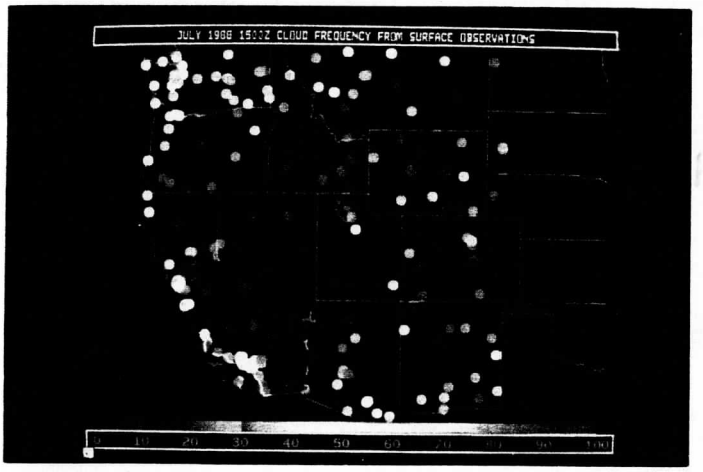

FIGURE 6

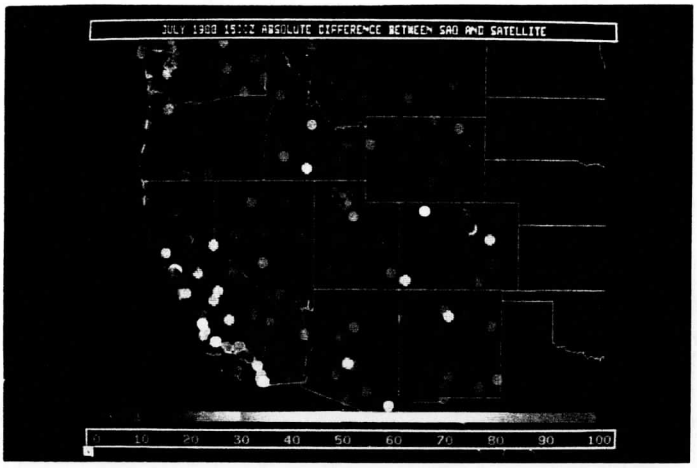

FIGURE 7

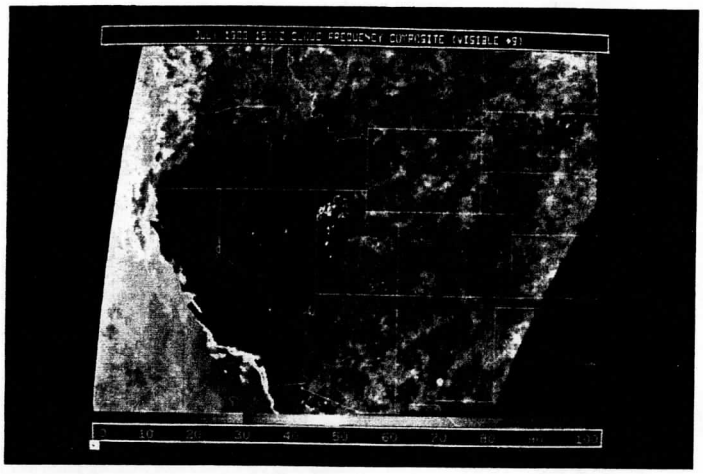

FIGURE 8

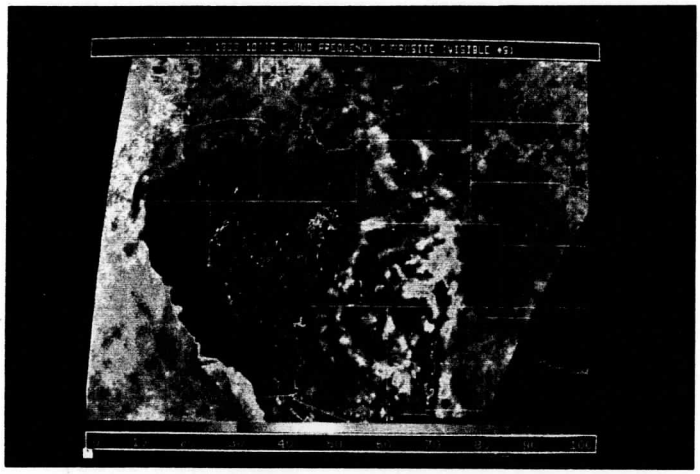

FIGURE 9

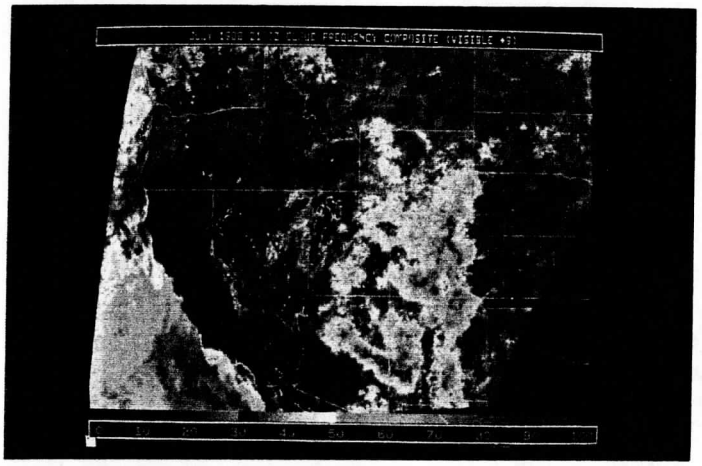

FIGURE 10

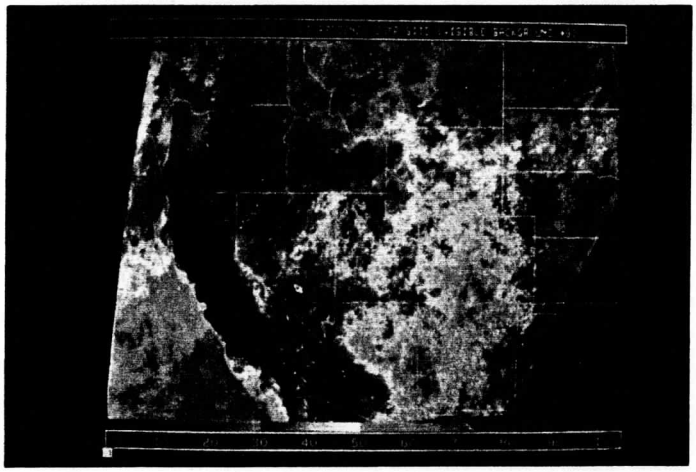

FIGURE 11

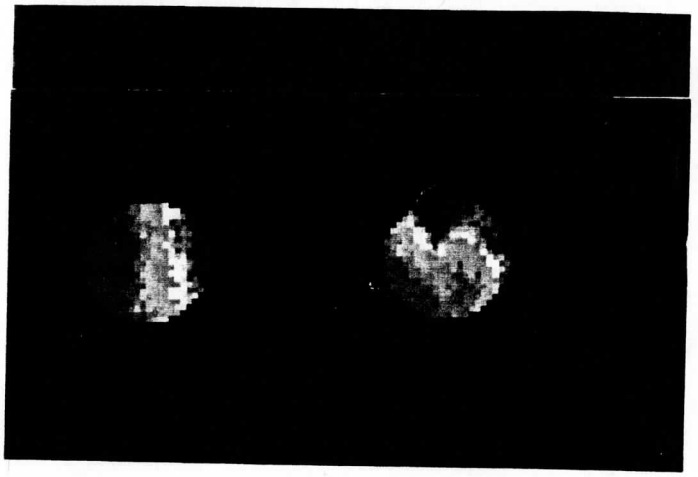

FIGURE 12

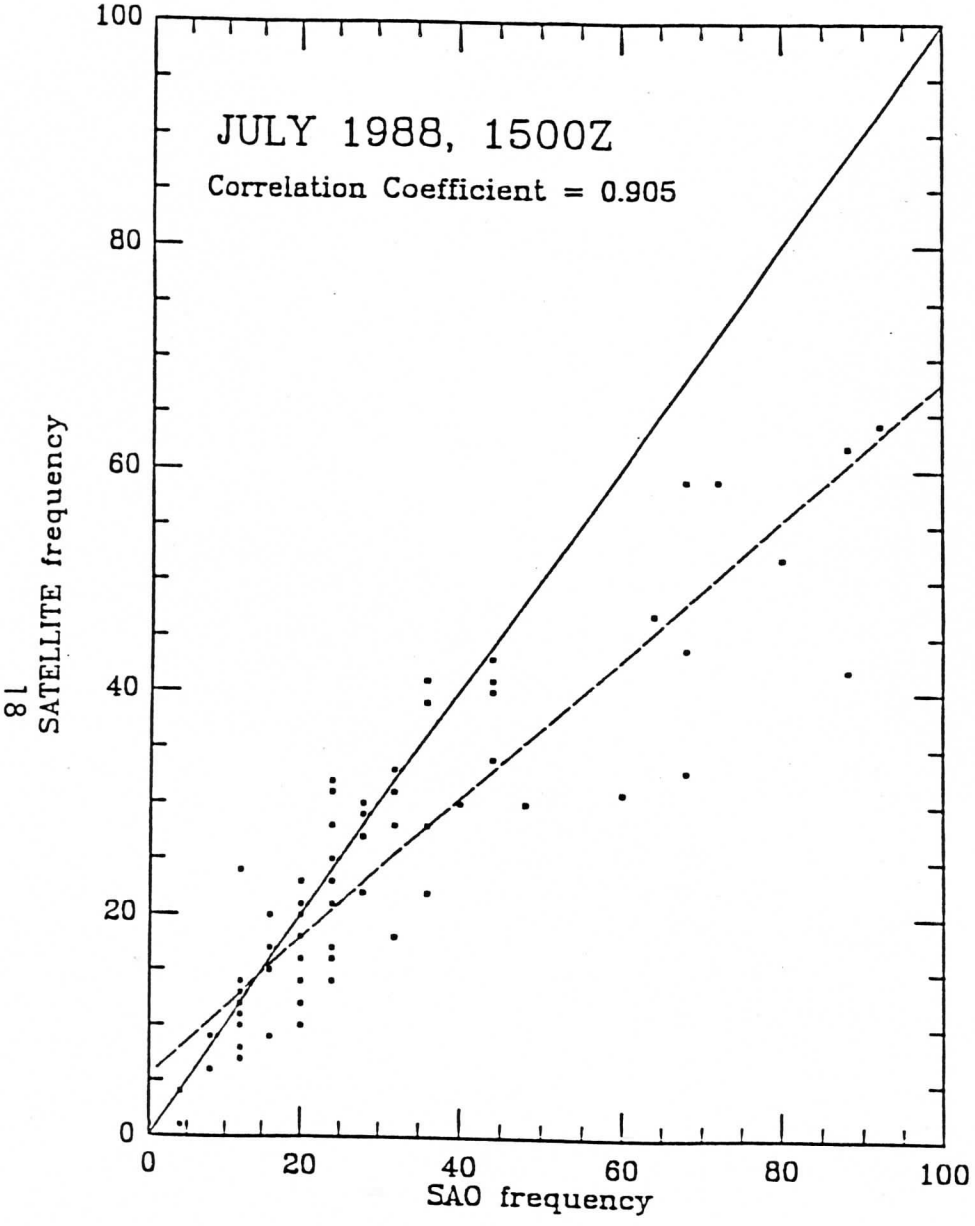

FIGURE 13

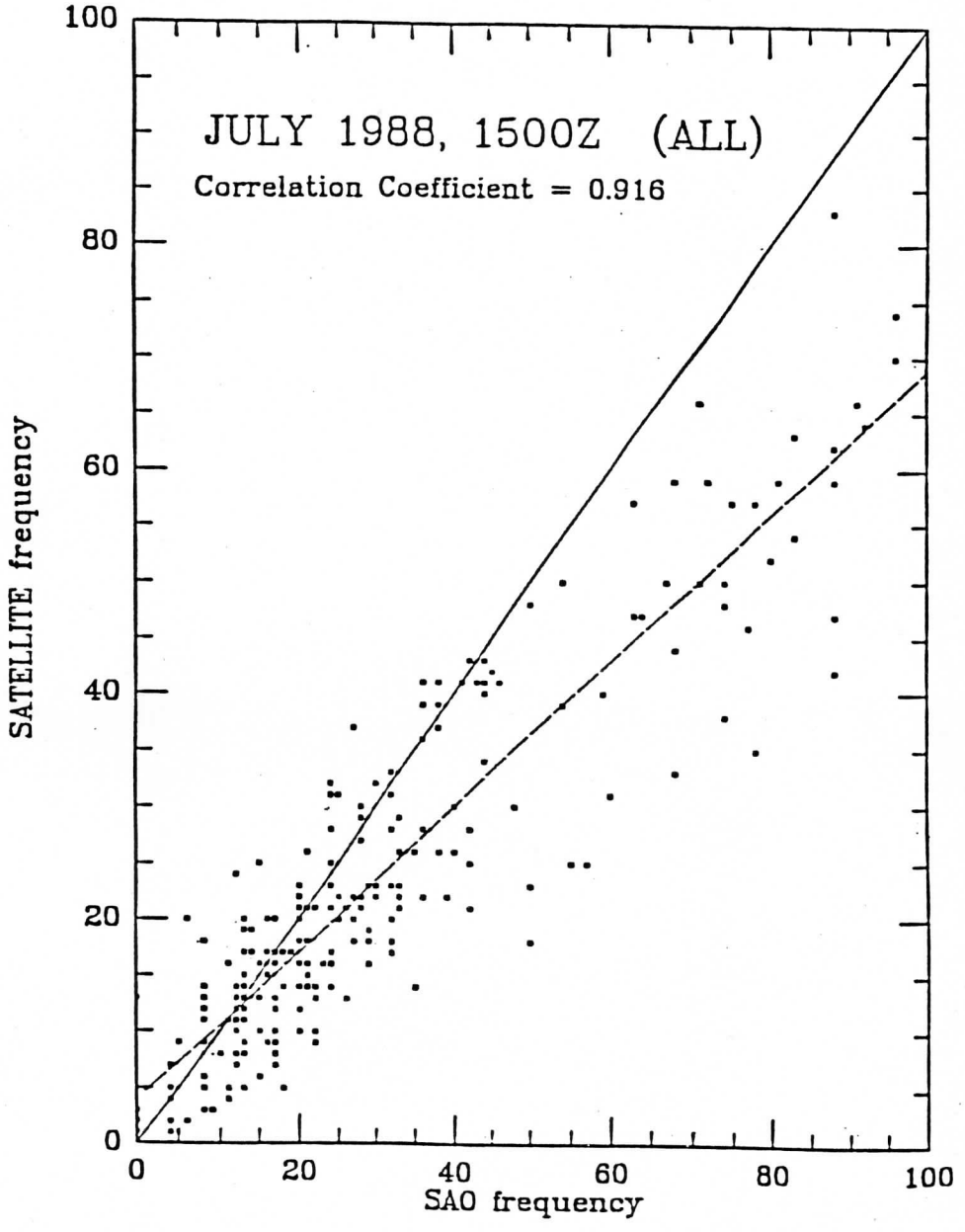

FIGURE 14

Month/Year/Time	No. of Pts	Mean Freq Obs / Sat	Mean Diff Obs - Sat	Corr Coef
July 1988 1500 UTC	69	30.0/24.1	7.5%	0.905
July 1988 1800 UTC	98	23.8/20.2	7.2%	0.829
July 1988 2100 UTC	68	23.8/22.6	6.5%	0.867
July 1988 0000 UTC	69	27.5/23.2	7.0%	0.894
Sept 1988 1500 UTC	60	32.9/27.3	7.4%	0.905
Sept 1988 1800 UTC	55	28.5/23.6	6.7%	0.915
Sept 1988 2100 UTC	44	21.4/18.4	4.9%	0.917
Sept 1988 0000 UTC	22	21.2/14.2	8.2%	0.876
Mar 1989 1500 UTC	79	54.0/ 7.3	46.7%	0.582
Mar 1989 1800 UTC	69	45.8/37.3	9.8%	0.930
Mar 1989 2100 UTC	65	51.5/44.3	11.1%	0.887
Mar 1989 0000 UTC	41	63.5/47.1	16.8%	0.891

Table 1. Comparison statistics for points with observations matching each day used for the satellite composite.

Month/Year/Time	No. of Pts	Mean Freq Obs / Sat	Mean Diff Obs - Sat	Corr Coef
July 1988 1500 UTC	226	30.5/23.8	8.7%	0.916
July 1988 1800 UTC	229	24.1/19.5	8.2%	0.764
July 1988 2100 UTC	215	25.5/23.3	7.2%	0.875
July 1988 0000 UTC	211	29.2/23.3	8.9%	0.894
Sept 1988 1500 UTC	208	31.0/24.9	8.6%	0.883
Sept 1988 1800 UTC	227	26.7/21.0	7.3%	0.893
Sept 1988 2100 UTC	213	23.7/19.4	6.3%	0.881
Sept 1988 0000 UTC	210	22.3/13.6	9.7%	0.831
Mar 1989 1500 UTC	188	55.4/ 7.6	48.1%	0.433
Mar 1989 1800 UTC	191	52.4/42.9	11.4%	0.927
Mar 1989 2100 UTC	191	54.1/44.8	11.7%	0.904
Mar 1989 0000 UTC	41	54.4/39.0	15.9%	0.875

Table 2. Comparison statistics for all points for which observations were available at least 15 days during the month.

[Reprinted from BULLETIN OF THE AMERICAN METEOROLOGICAL SOCIETY, Vol. 72, No. 3, March 1991]
Printed in U. S. A.

A Report on the Recent Demonstration of NOAA's Upgraded Capability to Derive Cloud Motion Satellite Winds

Robert T. Merrill+, W. Paul Menzel*, Wayman Baker**,
James Lynch***, and Eugene Legg****

1. Introduction

Cloud motions apparent in a sequence of geostationary satellite images represent an important source of meteorological information, especially over the oceans. However, improvements in data assimilation and numerical weather prediction (NWP) have outpaced improvements in satellite derived cloud motion vector (CMV) production over the past decade, and the reduced impact of CMV's has caused the National Meteorological Center (NMC) to restrict and the European Centre for Medium-range Weather Forecast (ECMWF) to discontinue the use of Northern Hemisphere upper level vectors from the U.S. GOES and the Japanese Himawari. The primary reason cited is a large slow bias, especially in and near jet cores.High level vectors from the European METEOSAT are still used.

Currently, the main problem of CMV production is assigning cloud tracked motions to the correct heights. Thin clouds which are most likely to be passive tracers of the flow at a single level are the best tracers, but assigning them to the correct height is especially difficult. Since the emissivity of the cloud is less than unity by an unknown and variable amount, its brightness temperature (Tb) in the infrared window is an overestimate of its actual temperature. Thus, heights for thin clouds inferred directly from the observed Tb and an available temperature profile are systematically low, and must be empirically or subjectively adjusted.

Height assignment errors carry a heavy penalty because of vertical wind shear, which is greatest near regions of active weather. For this reason, recent winds research at the Cooperative Institute for Meteorological Satellite Studies (CIMSS) has emphasized improved height assignments, and a physically based two-channel method using the "CO_2 slicing" approach (Menzel et al. 1983) has been incorporated into the CIMSS experimental winds algorithm (Merrill 1989).

Following encouraging tests in February and April 1989, a demonstration of the upgraded winds capability in a simulated operational setting was conducted in April of 1990. This report describes the upgrades and demonstration. Participating organizations are listed in Table 1.

2. Operational winds production at NESDIS

Low-level winds are currently produced automatically using a "picture-pair" correlation algorithm (Green et al. 1975) for the full disk from window channel imagery. Middle- and upper-level winds are produced interactively on the VAS Data Utilization Center (VDUC) computer. The operator examines three successive images at 30-min intervals and selects and tracks a feature using a joystick; then refines the feature's motion using an objective pattern matching technique (McIDAS Applications Guide 1988). A "single pixel" tracking mode is also available; the pattern match is bypassed and the tracer positions entered by the operator are converted directly to a velocity. Because of memory limitations, the full disk is processed in 10 sectors at 8-km resolution.

Height assignments are also made interactively. The operator estimates the cloud temperature from the window channel in opaque portions of a group of clouds and determines a pressure by comparison with a collocated temperature profile (using the 6-h or 12-h forecast from the most recent aviation model run). This height is then assigned to all consistent motions associated with the cloud group. In areas of thin cloud where observed window channel temperatures are all clearly too warm, the operator assigns an

+Cooperative Institute for Meteorological Satellite Studies, Madison, Wisconsin
*NOAA/NESDIS Advanced Satellite Products Project, Madison, Wisconsin
**NOAA/NWS National Meteorological Center, Washington, DC
***NOAA/NESDIS Synoptic Analysis Branch, Washington, DC

TABLE 1. Organizations participating in the NESDIS/NWS/CIMSS winds demonstration, April 1990.

Cooperative Institute for Meteorological Satellite Studies, University of Wisconsin-Madison:

- •Concept development
- •Software development
- •Transfer to VDUC
- •Real-time demonstration winds production on VDUC

NOAA/NESDIS Interactive Products Branch:

- • Demonstration software implementation on VDUC
- • Software to send winds to NMC

NOAA/NESDIS Synoptic Analysis Branch:

- • Demonstration winds editing on VDUC (in addition to operational duties).

NOAA/NWS/NMC Development Division:

- •Design and operation of parallel data assimilation cycle
- •Interpretation of model impact.

adjusted height based on the motion of the vector(s) relative to the overall synoptic situation and neighboring cloud groups with more reliable heights.

The operator also has the option to display the CMV's produced by the picture pair calculations and delete rogues. Manual quality control is implicit in the interactive winds production; the operator selects only those features with a definite motion signature and deletes any not representative vectors.

3. The improved winds algorithm

The long-range goal of NESDIS cloud motion winds research is to automate winds production as much as possible, freeing meteorologists to spend more time on the more complex processes and decisions. Winds processing involves tracer selection, tracking height assignment, and quality control. The current upgrade package largely automates tracer selection and height assignment. Tracking is already automated, and work continues on developing an algorithm which will perform most, but not all, of the quality control.

a. CO_2 ratio height assignment

The most important upgrade to the NESDIS winds capability is a two-channel "CO_2 ratio" height assignment (Menzel et al. 1983, Eyre and Menzel, 1989) using the 13.3 micron channel (VAS band 5) and the long-wave infrared window channel (VAS band 8). The details of implementation are described in Merrill (1989). The technique has been proven to be able to detect semitransparent thin clouds and to properly assign a cloud top pressure. Because of the use of a simple radiative transfer model and only two channels, difficulties still arise when multiple cloud layers are still present, especially very thin cirrus over a low-level marine cloud layer.

The algorithm also estimates a height directly from the window channel brightness temperatures from the colder portions of a tracer scene. The tracer is assigned to the higher of the two heights, but not higher than 150 hPa.

b. Automated winds algorithm

A flow chart of the automated winds algorithm is shown in Fig.1 and its operation is summarized below. A detailed description may be found in Merrill (1989).

A target selector divides the entire image into a number of cells (100 - 200 km on a side), and within each, selects a point associated with a maximum in brightness temperature and gradient, subject to some conditions on the overall brightness temperature and contrast of the scene. Heights are also computed at this stage.

The tracking algorithm is then applied for each target point. A tracking area about $(100\ km)^2$ is centered on the target in the first image. The algorithm then goes to the second image in the loop and searches for the area which best matches the radiances in the tracking area. The search is confined to a $(150\ km)^2$ region centered on the displacement indicated by the 12-h NMC global aviation model wind prognosis. If a successful match is found, the indicated displacement is used to position a new tracking area on the second image and a new search area on the third, and the process is repeated. The two vectors are then averaged to produce a final wind estimate.

Three forms of quality control are applied. Because of the limited search area, motions deviating from the guess by more than a finite amount cannot be matched (Merrill 1989), weakly constraining the winds to a guess. The pair of vectors produced from the three images are compared, and if they differ by 5 ms^{-1} or more in either component, the report is flagged as unusable. The remaining winds are then displayed on the VDUC and edited manually by checking for consistency and by comparing with the first guess and rawinsondes (if available).

4. Demonstration

The goals of the April 1990 demonstration were a) to demonstrate the capability of the upgraded system to produce regional winds coverage within the operational data cut-off times, and b) to test the impact of the winds with improved heights on the NMC global forecast system.

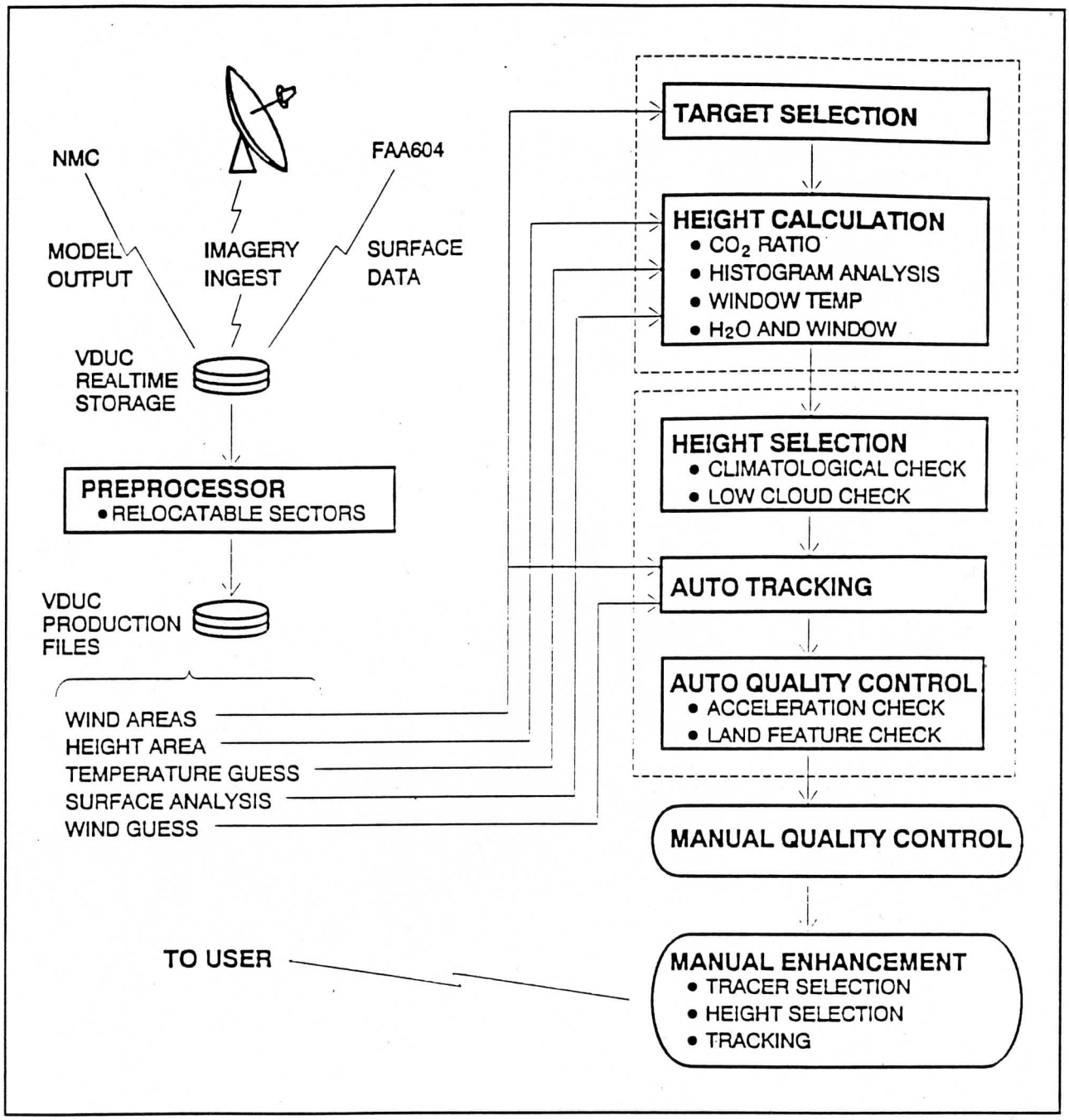

FIG. 1. Flow chart of the CIMSS experimental wind system. Boxes enclose processes, and dashed outlines define single job steps on the UW McIDAS.

The demonstration consisted of parallel production of winds using the operational and upgraded system. The domain for demonstration winds production was chosen to provide winds over the data sparse subtropical eastern Pacific Ocean in connection with the polar and subtropical jet stream and cut off lows (Fig. 2). Because the main impact of the CO_2 heights is felt for high level tracers, the demonstration winds were produced only above 600 hPa. Winds were produced from 15-min loops of imagery starting at 1046, 1646, and 2246 UTC each day beginning on 18 April and continuing through 27 April. Processing was usually completed between 10 and 20 min after nominal synoptic time, and manual editing typically took 1-2 h beyond that.

Figures 3-5 show an example of a demonstration wind set. Figure 3 shows the operational winds. The CMV's are faster than the analysis and provide better definition of the subtropical jet along the poleward edge of the cirrus band. Figure 4 shows how the more

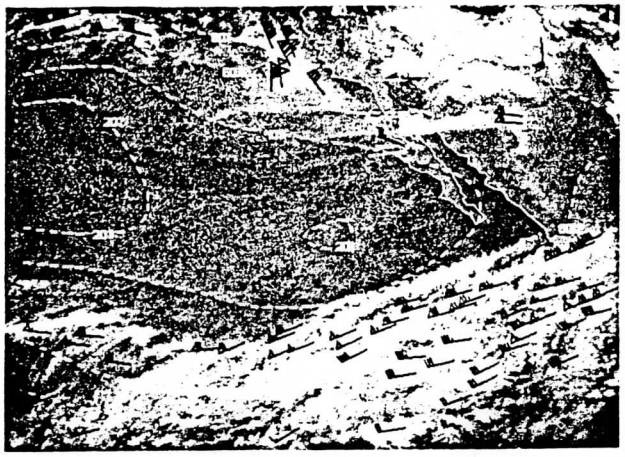

FIG. 5. Same as Fig. 3., but with demonstration winds (CO_2 heights and 15-min loops).

and gradient winds derived from VAS temperature retrievals were generated twice daily to supplement the operational winds in the vicinity of Atlantic basin tropical cyclones.

Based on the successes of the April 1990 demonstration and evaluation during the 1990 Atlantic hurricane season, operational implementation of the upgraded algorithm for full disk winds four times daily will come in 1991. At that time, low level winds will be produced using the picture-pair technique, and winds at all levels will be produced using an automated technique with CO_2 heights and the combined set will beedited manually. Further model impact tests will be conducted by the NMC Development Division as well.

Acknowledgements. The experimental winds were produced by Chris Velden, Tim Schmit, Kurt Brueske, Tony Schreiner, and Robert Merrill of CIMSS, and Cecil Paris from Systems Design and Applications Branch, NESDIS. The operational winds were produced by the Synoptic Analysis Branch, NESDIS where Mark Ruminski deserves special mention for his extra efforts to inspect both operational and experimental wind products in real time. Curtis Holland of the Interactive Processing Branch, NESDIS provided valuable on site support at the VDUC. Dennis Deaven, Geoff DiMego, and Dennis Keyser of the Regional and Mesoscale Modelling Branch, Development Division, NMC assisted with the model impact tests. The VAS schedules were adjusted by the Satellite Operations Control Center, where Gordon Moiles was instrumental in satisfying the data needs for the demonstration. This work was supported by NOAA contract 50-WCNE-8-06058.

References

Eyre, J. R., and W. P. Menzel, 1989: Retrieval of cloud parameters from satellite sounder data: A simulation study. *J. Appl. Meteor.*, **28**, 267-275.

Green, R., G. Hughes, C. Novack and R. Schreitz, 1975: The automatic extraction of wind estimates from VISSR data. NOAA Technical Memorandum NESS 64, 94-110.

McIDAS Applications Guide, 1988: Cloud drift winds. *A Space Science and Engineering Center Manual,* Chap. 11.

Menzel, W. P., W. L. Smith and T. R. Stewart, 1983: Improved cloud motion wind vector and altitude assignment using VAS. *J. Clim. Appl. Meteor.*, **22,** 377-384.

Merrill, R., 1989: Advances in the automated production of wind estimates from geostationary satellite imaging. *Fourth Conference on Satellite Meteorology,* 16-19 May, San Diego, Amer. Meteor. Soc., 246-249.

accurate objective height assignments possible with the CO_2 ratio method, especially in the translucent cirrus in the polar jet off of California, greatly increases the coverage possible in the demonstration wind set (Fig. 5) without subjective height reassignment.

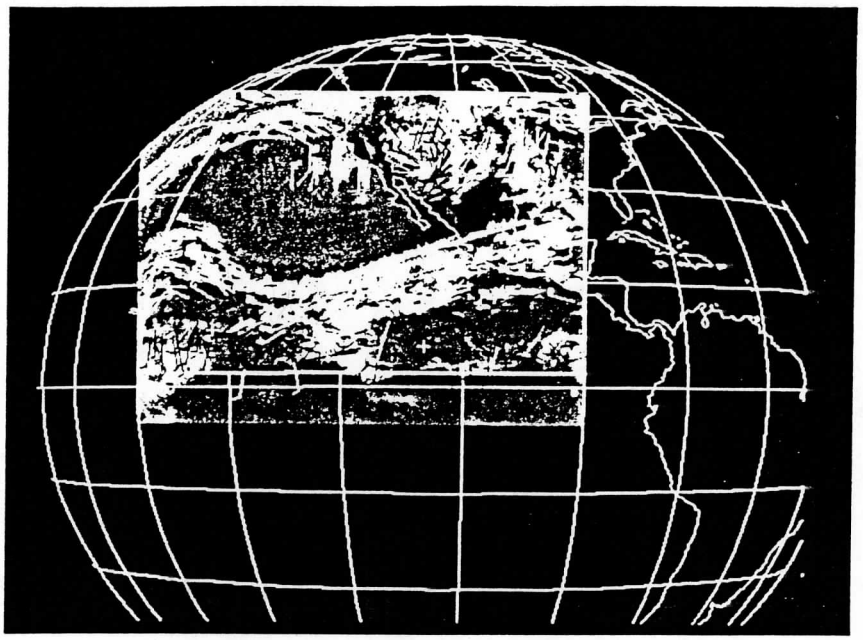

FIG. 2. The demonstration domain for winds production, and an example of a wind set. Final winds are shown in white, and winds deleted during the manual editing process are shown in gray.

5. Preliminary results of the GDAS Model impact test

The NMC Global Data Assimilation System (GDAS) was run in parallel in real time with a) the operational winds and b) the experimental winds covering the demonstration domain and operational winds elsewhere. The experimental, high-level (p< 600 hPA) CMV's were used in the NMC parallel GDAS at 0000, 1200, and 1800 UTC for the 10-day demonstration period. Low-level winds produced by the operational picture-pair technique were passed to the GDAS, even in the experimental area. Analyses produced during the assimilation were used as initial conditions for 5-day forecasts starting at 0000 UTC on April 19 through April 27.

Comparison of the parallel forecasts indicated a slight positive impact of the demonstration winds. The 5-day 500 hPa height forecast anomaly correlation scores for the10-day period over the northern hemisphere extratropics, a typical index of forecast accuracy, increased from 0.73 to 0.75 on average, with improvements on six of the 10 demonstration days. Though no formal significance tests are available, such a difference is equivalent to extending the limit of useful forecast time by about 2 h and is of the same scale as difference between the forecasts made by the different global forecast centers.

6. Operational implementation at NOAA/ NESDIS/SAB

The NESDIS Synoptic Analysis Branch (SAB) used this improved winds capability for operational support of the National Hurricane Center during the 1990 hurricane season. CO_2 automated winds, automated water vapor motion winds (6.7 and 7.3 micron bands),

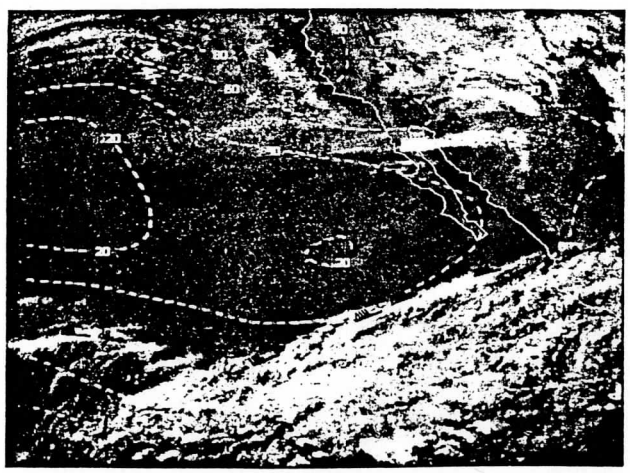

FIG. 3. Operational 200 – 300-mb winds for 0000 UTC 25 April 1990 with the NMC 250-mb isotach analysis superimposed on the GOES infrared window image.

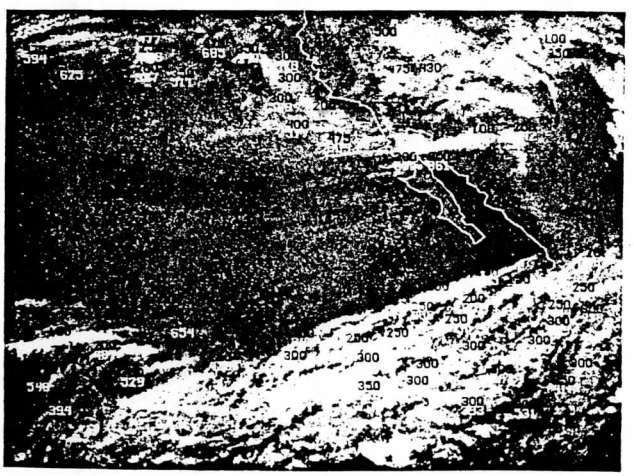

FIG. 4. CO_2 ratio heights (black) compared with heights empirically estimated from the window channel brightness temperatures (white) from the upgraded winds algorithm for 1200 UTC 24 April 1990.

GEOSTATIONARY SATELLITE DETECTION OF BIOMASS BURNING IN SOUTH AMERICA

E. M. Prins[1]
Cooperative Institute for Meteorological Satellite Studies
Madison, Wisconsin 53706

W. P. Menzel
NOAA/NESDIS
Madison, Wisconsin 53706

[1]Current address: Sonoma Technology Inc., Santa Rosa, CA 95403

1. INTRODUCTION

During the past decade there has been increased human intervention in the tropics and subtropics, specifically in the Amazon Basin of South America. Each year intense biomass burning is associated with tropical deforestation in the selva (forest) and agricultural burning in the cerrado (grassland) regions of Brazil (Nelson et al., 1987; Malingreau and Tucker, 1988; Setzer, 1988 (personal communication); Booth, 1989). The implications of these activities are unknown and possibly of global consequence. Some immediate concerns include loss of species, increased surface albedo and water run-off, decreased evapotranspiration, higher concentrations of several greenhouse gases and large aerosols, and effects on atmospheric chemistry (Greenberg et al, 1984; Henderson-Sellers et al, 1984; Crutzen et al 1985; Delany et al, 1985; Fishman et al, 1986; Matson and Holben, 1987; Andreae et al, 1988; Browell et al, 1988; Sasche et al, 1988; Simmons, 1988).

The most practical and economically feasible manner of monitoring the extent of burning associated with tropical deforestation and grassland management is through remote sensing. To date, many remote sensing methods have utilized multispectral data from the Multispectral Scanner (MSS) on Landsat-1, -2, . ., -5, the Thematic Mapper (TM) on Landsat-4 and -5, and the Advanced Very High Resolution Radiometer (AVHRR) on the NOAA polar orbiters (Tucker et al., 1984; Woodwell et al., 1986; Matson and Holben, 1987; Matson et al, 1987; Nelson et al, 1987; Malingreau and Tucker, 1988). A number of these techniques calculate vegetative indices in order to estimate deforestation areas (Justice et al, 1985; Malingreau et al, 1985; Townshend et al, 1987). However, the extent of deforestation is usually underestimated, mostly due to the inability to distinguish between primary and secondary growth (Fearnside, 1982; Tucker et al, 1984; Tucker et al, 1986; Nelson and Holben, 1986; Malingreau and Tucker, 1988).

This paper presents the results of using Geostationary Operational Environmental Satellite (GOES) Visible Infrared Spin Scan Radiometer Atmospheric Sounder (VAS) infrared window (3.9 and 11.2 microns) data to monitor biomass burning associated with deforestation and grassland management in South America. The technique of Matson and Dozier (1981) was adapted to GOES VAS infrared data to determine the size and temperature of fires associated with deforestation and grassland burning in selected regions of South America. Although VAS data do not offer the spatial resolution available with AVHRR data (7 km versus 1 km, respectively), this decreased resolution does not seem to hinder the ability of the VAS instrument to detect fires; in some cases it proves to be advantageous in that saturation does not occur as often. In addition, VAS visible data is helpful in verifying that the hot spots sensed in the infrared are actually related to fires. Furthermore, the fire plumes can be tracked in time to determine their motion and extent. In this way, the GOES satellite offers a unique ability to monitor diurnal variations in fire activity and transport of related aerosols.

Estimates are very uncertain regarding the amount of the Amazon rainforest that has already been cleared and the rate of that deforestation. In 1978 studies indicated 72,000 km^2 or 1.45% of the Brazilian Legal Amazonia had been cleared. In 1979 other studies estimated that 260,000 km^2 or 5.23% of the Amazon had been deforested (Tucker et al., 1984). In 1980 Brazil's National Institute for Space Research (INPE) released information showing that only 77,200 km^2 or 1.55% had been cleared (Tardin et al, 1980). Views on the rate of clearing are even more varied; estimates range from as low as 10,000 km^2 to as high as 100,000 km^2 per year (Tucker et al., 1984). Analyses done by Setzer utilizing AVHRR data to locate biomass burning reveal that many Brazilian provinces exhibit exponential clearing rates. Approximately 200,000 km^2 were burned in 1987; nearly 80,000 km^2 of this amount, representing 1.6% of the Legal Amazonia, corresponds to the clearing of virgin forest and the remaining 120,000 km^2 is burning in previously cleared areas (Setzer et al, 1988; Setzer and Pereira, 1989). This figure exceeds some worldwide deforestation estimates. The 1988 burning season exhibited a decrease in the burning of cleared virgin forest to 5 million hectares (50,000 km^2). Preliminary estimates for 1989 reveal continued reduction in deforestation as well (Brooke, 1989).

It has been suggested that the rate of deforestation is best estimated by monitoring biomass burning. Matson and Dozier (1981) developed a technique utilizing the AVHRR 3.7 micron and 10.8 micron channels to detect subpixel resolution forest fires. The technique provides reasonable estimates of temperature and area of fires in those pixels that are not saturated (Matson et al., 1984; Matson and Holben, 1987). Unfortunately, many of the pixels are saturated. In addition, it is difficult to monitor plume activity associated with these subpixel fires, since the NOAA polar orbiting satellite has only one day time pass over a given area.

2. TECHNIQUE DESCRIPTION

As described in more detail in Matson and Dozier (1981), the different brightness temperature responses in the two infrared window channels can be used to estimate the temperature of the target fire as well as the subpixel area it covers. Typically, the difference in brightness temperatures between the two infrared windows at 3.9 and 11.2 microns is due to reflected solar radiation, surface emissivity differences, and water vapor attenuation. This normally results in brightness temperature differences of 2-4 K. Larger differences occur when one part of a pixel is substantially warmer than the rest of the pixel. The hotter portion will contribute more radiance in shorter wavelengths than in the longer wavelengths. This can be seen in Figure 1 which depicts a portion of a line of VAS data over South America at 1831 UTC on 24 August 1988. Pixels a, b, and c represent areas where subpixel fires are burning. The largest temperature difference occurs at location b where the 11 micron brightness temperature value is 306.2 K and the 4 micron brightness temperature is 321.4 K. Warm areas surrounding these pixels are previously burned regions.

The fire extent and temperature within a field of view can be determined by considering the upwelling thermal radiance values obtained by both channels (Matson and Dozier, 1981; Dozier, 1981). For a given channel, j, the upwelling radiance sensed by a downward looking radiometric instrument is obtained by integrating the product of the Planck function and the spectral response function of the channel

$$L_j(T) = \frac{10^{-6}}{\pi} \frac{\int_0^\infty \epsilon(\lambda)\, B(\lambda,T)\, \Phi_j(\lambda)\, d\lambda}{\int_0^\infty \Phi_j(\lambda)\, d\lambda} \qquad (1)$$

where the Planck function is

$$B(\lambda,T) = \frac{c_1 \lambda^{-5}}{\exp[c_2/(\lambda T)]-1} .$$

The following notation and constants are used in this work; for the most part they are identical to those given in radiation texts.

$L_j(T)$	Integrated upwelling thermal radiance ($W/m^2/ster/\mu m$) in channel j as a function of temperature T
p	Portion of pixel covered by the target temperature
T	Temperature (K)
T_j	Brightness temperature (K) measured by channel j
T_b	Background temperature (K)
T_t	Target temperature (K)
$B(\lambda,T)$	Planck function ($W/m^2/ster/m$)
ϵ	Emissivity
λ	Wavelength (m)
$\Phi j(\lambda)$	Spectral response function for channel j
c_1	3.741832×10^{-16} W m^2
c_2	1.43876×10^{-2} K m

Equation (1) does not take into consideration the intervening atmospheric radiance contribution or attenuation. Generally, variations of emissivity with wavelength for a given channel are assumed to be negligible for most earth

surfaces being sensed. In addition, variations of emissivity with respect to the instrument's nadir angle are ignored. These assumptions make it possible to consider emissivity as a constant for a given channel allowing it to be moved outside the integral in Eq. (1).

When the GOES VAS radiometer senses radiance from a pixel containing a target of blackbody temperature T_t occupying a portion p (between zero and one) of the pixel and a background of blackbody temperature T_b occupying the remainder of the pixel (1-p), the following equations represent the radiance sensed by the instrument at 4 and 11 micron, respectively (provided there is no atmospheric contribution or attenuation).

$$L_4(T_4) = p\ L_4(T_t) + (1-p)\ L_4(T_b)$$

$$L_{11}(T_{11}) = p\ L_{11}(T_t) + (1-p)\ L_{11}(T_b) \qquad (2)$$

If T_b is known, these two nonlinear equations can be solved for T_t and p. In this study, the solution to the set of equations is found by applying a globally convergent bisection technique followed by Newton's method.

Since the radiance sensed by the GOES VAS instrument is not emitted from blackbodies and it passes through the intervening atmosphere, corrections must be introduced to T_b, T_4, and T_{11}. Burning or smoldering fires are usually covered by clouds and smoke containing organic particles of varying sizes and shapes, necessitating a correction to the transmittance. Most of the smoke is composed of water vapor, but there are other constituents as well (Andreae et al, 1988; Browell et al., 1988). The 11 micron channel is more affected by atmospheric water vapor than the 4 micron channel. With Nimbus-2 data, it was found that the water vapor correction for a moist atmosphere is approximately 4 K at 300 K for

the 11 micron window and 2 K at 300 K for the 4 micron window (Smith et al, 1970). By calculating a linear regression relationship between the VAS visible brightness counts and VAS infrared window brightness temperature in a variety of haze conditions (approximately 50) and extrapolating to clear sky conditions, the Nimbus corrections were found to be appropriate for the VAS data studied here (Prins, 1989).

In the absence of clouds and smoke, the remaining two major considerations are the effects of surface emissivity in the 4 and 11 micron window channels and solar reflectivity in the 4 micron channel. Emissivity investigations for vegetation similiar to that found in the selva and cerrado suggest an emissivity for tropical rainforest of .96 in the 4 micron region and .97 in the 11 micron region, while the emissivity of dry grassland is .82 and .88 respectively (American Society of Photogrammetry, 1983). The observed short wave window radiance also contains contributions due to solar reflection that must be distinguished from the ground emitted radiances. Incorporating emissivity and solar reflectivity corrections produces the following form of equations 2;

$$L_4(T_4) = e_4\ p\ L_4(T_t) + e_4\ (1\text{-}p)\ L_4(T_{b11}) + (1\text{-}e_4)\ L_{4refl}$$

$$L_{11}(T_{11}) = e_{11}\ p\ L_{11}(T_t) + e_{11}\ (1\text{-}p)\ L_{11}\ (T_{b11}) \qquad (3)$$

where e_4 and e_{11} represent emissivity in the shortwave and longwave infrared windows respectively and L_{4refl} is the reflected solar radiance in the 4 micron channel. Grey body characteristics are assumed over the spectrum covered by the shortwave infrared window.

The algorithm used in this study proceeds as follows. A fire is identified and a nearby fire free area is located. All observed brightness temperatures

over the fire are adjusted for smoke attenuation; 2 K is added to the 4 micron brightness temperatures and 4 K is added to the 11 micron brightness temperatures. T_4 and T_{11} represent the smoke corrected brightness temperatures over the fire for the two spectral bands. The background temperature, T_{b11}, is determined from the 11 micron brightness temperature in a nearby fire-free pixel (p=0) that is adjusted for surface emissivity. Subsequently, the shortwave window reflected radiance for this same fire-free pixel, L_{4refl}, is solved. The input parameters T_{b11}, T_4, T_{11}, and L_{4refl} are now all in place; thus equations 3 can be solved for p and T_t.

3. ADDITIONAL CONSIDERATIONS

A. Identifying Fires in the Satellite Image

The process of fire identification is strongly dependent on image interpretation. In this work, a fire was suspected if the haze corrected 3.9 micron observed brightness temperature showed a 4 K increase over the 3.9 micron background temperature and the haze corrected 11.2 micron observed temperature displayed a 1 K increase above the 11.2 micron background temperature. Hot spots were not considered fires unless they were accompanied by some indication of a fire in the visible channel, such as a smoke plume. The temporal resolution of the GOES VAS data proved to be extremely useful in two ways. First, a hot spot was often evident in the infrared channels at a certain time period, but the corresponding visible channel showed little or no indication of a fire, possibly due to obscuration by a plume produced by a fire located upwind. A visible image a half hour earlier usually clarified whether a fire was located there. Second, it is difficult to distinguish regular clouds from plumes in a single image. By looping a series of half hourly visible images it becomes quite easy to identify the point sources of fires, since they remain at a constant location over time.

B. Spatial Resolution of the Satellite Sensor

The spatial resolution of GOES data is a limiting factor in this work; at nadir it is .9 km by .9 km in the visible, 6.9 km by 6.9 km in the 11.2 micron channel, and 13.8 km by 13.8 km in the 3.9 micron channel. With the noise limitations of the sensor in a typical scene (approximately .2 K for both infrared windows (Menzel et al., 1983)), GOES VAS data can resolve a fire with a target temperature of 450 K and area of .03 km^2 (for AVHRR the resolvable area is .00015 km^2). However, as mentioned earlier, the lack of horizontal resolution of

the VAS also serves as an advantage in that the sensor does not saturate as often as the AVHRR does over fires. VAS saturates when a fire of 450 K occupies 5 km^2 of the field of view, for AVHRR this shrinks to .02 km^2. While the VAS misses small fires that AVHRR senses, it can measure the radiances of large fires that saturate the AVHRR.

The effects of sensor resolution were investigated for five cases of biomass burning observed at the same location at approximately the same time (within one hour) in NOAA AVHRR and GOES VAS images on 24 August 1988. The target temperature and area burned were calculated for the five fire areas in both images. Fires A-C are isolated fires; fires D-E are in the middle of more intensive burning affecting a considerable area. Intercomparison was hindered by saturation in the AVHRR for large fires and poor detection by VAS for small fires; also the time difference of one hour can reveal considerably different actual burning areas. Better comparison is achieved for the areas of intensive burning. The AVHRR estimate of burning within a given VAS fov ranges from several tenths of km^2 (using the algorithm of section 2 on each individual AVHRR fov and summing those areas where T_t is greater than 400K) to several km^2 (assuming the saturated pixels are totally on fire). VAS falls between these extremes. Table 1 summarizes the intercomparison and Figure 2 shows the AVHRR and VAS short wave window images. It is evident from the AVHRR 1 km data that the area covered by a VAS fov includes a number of fires which act collectively to produce an average temperature and total area burned. The summation of the AVHRR estimates covering the area of one VAS field of view yields burned area estimates up to 5 times smaller than those determined from VAS.

C. Cloud and Haze Contamination

The algorithm presented in the previous section is very sensitive to corrections for cloud and haze conditions. Figure 3 shows fire temperature and area as a function of smoke correction for VAS observations from a typical fire; as the correction ranges from 0 to 6 K, the area of the fire ranges from 1.1 to 2.9 km^2 while the temperature of the fire ranges from 503 to 460 K respectively. Clearly accurate determination of the smoke correction is essential; the procedure outlined in section 2 offers confidence within 1 K which results in a relative error of 33% in the area estimate.

To avoid the uncertainty associated with the smoke correction, a simplified algorithm has also been tested. It proceeds as follows. After identification of a fire, assume a fire temperature of 450 K. Determine the background temperature T_{b11} from a water vapor corrected 11 micron brightness temperature in a nearby fire free (and smoke free) pixel that is also adjusted for surface emissivity. Solve for L_{4refl} for this same fire free pixel. Use T_4 and L_{4refl} to solve for p (assuming T_t= 450 K). The fire area now represents the area that a 450 K fire would occupy for the observed radiances; it is a relative measure of the fire area for a representative fire temperature and much less sensitive to the difficult smoke correction. The last column of Table 1 shows these results for the AVHRR comparison; the fires are all hotter than 450 K on the average and thus the area is overestimated. More typical areas of burning fare better in the simplified algorithm.

D. Noise, Emissivity, and Diffraction

The algorithm to calculate the target temperature and area burned for a specific fire depends on the accuracy of the background and observed temperatures at 3.9 and 11.2 microns. Assuming these can be determined within 1 K of the true value, a numerical error analysis reveals the error possible under typical

conditions. The relative error in the burned area estimate is less than 1% when the background and observed temperatures are affected by an offset of 1 K in the same direction (they are both greater than or less than the true values). If the background temperatures for both channels are underestimated and the observed temperatures are overestimated by 1 K for both channels or vice versa, a relative error of approximately 25% is obtained.

If the corrections for emissivity and solar reflectivity are omitted for typical conditions, a relative error of 4% in p is produced. Errors in the correction probably do not exceed the size of the correction itself.

Diffraction is a concern because the surface brightness temperature recorded for a specific pixel is effected by the area outside of that pixel. If the pixels adjacent to one containing a fire do not contain a fire, this will reduce the brightness temperature used to calculate the target temperature and area burned. Adjacent pixels containing fires of different magnitudes will also influence each other. Diffraction acts to degrade the detector response to radiances within the instantaneous ground field of view (IGFOV) (Menzel, 1980). Numerical simulations for a typical fire indicated that diffraction introduces a relative error of aproximately 15%.

Although none of these errors are small, the GOES VAS data can offer viable burned area estimates, considering that results produced in other studies can vary by an order of magnitude.

4. RESULTS

The algorithm outlined in Section 2 has been implemented on GOES VAS data for 1231 UTC, 1531 UTC, 1831 UTC, and 2131 UTC on 14 August 1983. and 1831 UTC on 15 and 16 August 1983. The area considered is centered at 8 S latitude and 50 W longitude along the Araguaia River in the Brazilian states of Para and Goias (see

Figure 4). The analysis provides a unique view of the diurnal variability of fire detection, the lifetime of individual fires, and burned area estimates for this region of the Amazon in 1983. In addition, VAS data in the selva (11 S latitude, 62 W longitude) and cerrado (22 S latitude, 56 W longitude) regions on 24 August 1988 are analyzed to determine the extent of burning in the tropical forest of Rondonia and Mato Grosso, Brazil, and the grasslands in Mato Grosso, Brazil, and Paraguay (see Figure 4). Visible satellite images for 24, 25, and 29 August 1988 are considered in conjunction with infrared images for the South American continent in an attempt to determine the prevailing circulation and transport of constituents associated with biomass burning by tracking smoke plumes and clouds. Past studies with NOAA polar orbiting data have not been able to accurately ascertain the transport of aerosols associated with biomass burning, but the half hourly multispectral GOES VAS data provide a unique opportunity to monitor this transport.

A. Diurnal Variability

In 1983, GOES VAS data for the two infrared window channels were available hourly, making it possible to investigate the diurnal cycle of individual fires. Fires detected on 14 August 1983 at 1231 UTC, 1531 UTC, 1831 UTC and 2131 UTC reveal a diurnal cycle in the number of fires observed, with the maximum number detected at 1531 UTC (noon) and a minimum at 2131 UTC (evening). Mostly likely the reduction in the number of fires sensed in the evening is due to an actual reduction in burning at the end of the day, however there are accounts of intense burning at night in the selva and the cerrado (Sauck, 1988).

Twenty fire fovs (fields of view where burning was detected) were identified and tracked in time in an effort to determine what happens to an individual fire fov over a span of 54 hours (in addition to the data on 14 August

1983, 1800 UTC on 15 August 1983 and 1831 UTC on 16 August 1983 were also processed). The results are presented in Figure 5. The average time that a given fov indicates the presence of fires is approximately 36 hours. Of the 20 fire fovs identified at 1531 or 1831 UTC on 14 August 1983, 19 of them were detected on one or both of the successive days, but only five of these fire fovs were identified at 2131 UTC on 14 August 1983. It is likely that burning occured in adjacent areas within the fov for several days in a row. However the actual burning only lasts a few hours so the fires disappear regularily in the GOES VAS image at 2131 UTC. This strong diurnal variation in detectability of fires was noted on most of the roughly 100 days inspected.

These results indicate that many of the same fire fovs are seen on successive days (an individual fov shows fires for 36 hours on the average), but the optimum time to monitor biomass burning is between 1530 UTC and 1830 UTC (noon to early afternoon local time).

B. Burned Area Estimates

A summary of the fire statistics calculated from GOES VAS data for portions of the Amazon Basin and the Cerrado region (depicted in Figure 4) are presented in Table 2. Days of very intense burning were selected. Not all fires detected were processed due to a variety of problems; on the average, temperature and area estimates were made for 88% of the detected fires. The mean fire temperatures are representative of low temperature or smoldering fires. The area burned is presented in large detector field of view pixels (corrected for viewing angle) and km^2. The largest burned area was detected at 1531 UTC on 14 August in the 1983 data and is estimated at 552.0 km^2. It is significant to note that this value is nearly twice as large as those obtained at 1231 UTC and 1831 UTC and 17 times as large as the estimate obtained at 2131 UTC. For those satellites which

only offer one view of this region per day, it is imperative that these diurnal variations are considered.

Area estimates for the selva region on 24 August 1988 indicate that the burning in the western portion of the Amazon Basin is as large as that detected in the eastern portion in 1983. At 1831 UTC approximately 361.7 km^2 were burning in the western selva. Setzer et al (1988) report roughly 200,000 km^2 of vegetation were burned in the Brazilian portion of the Amazon Basin in 1987. The VAS estimate for one section of the basin on 24 August 1988 represents approximately .2% of the value obtained by Setzer for an entire year. 24 August 1988 was one of the most intensive burning days observed with the VAS instrument in the 1988 burning season. The burning in the cerrado region for this day was also very extensive.

The results from the simplified algorithm which assumes a fire temperature of 450 K are presented in the last column. Reasonable agreement is apparent; the same trends stand out and the area of burning is usually within a factor of two. The simplified algorithm shows potential for routine application.

A visible image of South America for 24 August 1988 is presented in Figure 6. Many fires can be seen in the state of Para, and there is considerable burning in the western portion of the Amazon. Smoke plumes associated with deforestation can be seen across the entire Amazon Basin from 50 W to 70 W. Biomass burning in the cerrado region of South America is also clearly visible.

Reports from Brazil indicate that the average size of a fire is less than 0.5 km^2 (Sauck, 1988). The results obtained for p in this study indicate that a given VAS pixel probably contains many individual fires, which act collectively to produce an average target temperature (T_t) and total area (p) covered by the fires. Most of the pixels that were processed produced burned area estimates

greater than .3 km^2 and less than 5 km^2. This indicates that one VAS pixel (188 km^2) may contain several fires.

C. Aerosol Transport

Haze is evident throughout the western portion of the Amazon Basin and in the cerrado on 24 August 1988 (see Figure 6). Additional natural forest fires can be seen west of the cerrado in the foothills of the Andes Mountains. Over a period of five days the entire region from 50 W to the Andes Mountains was covered with smoke and haze. Surface weather observations in this region reported intense haze with very low visibilities.

By tracking the smoke and haze in time, it is possible to infer the prevailing circulation and transport of aerosols. Winds at 1801 UTC on 24 August 1988 (not shown), 1301 UTC on 25 August 1988 (Figure 7a), 1301 UTC on 29 August 1988 (Figure 7b), and 1801 UTC on 29 August 1988 (not shown) were estimated from a half hourly sequence of three visible and infrared (11 micron channel) images. These wind sets depict an anticyclonic flow throughout the Amazon Basin. The easterly winds in the northern portion of the Amazon Basin transport the aerosols westward. The Andes Mountains act to deflect the material south where westerlies transport the material over the Atlantic Ocean. Here they can be channeled by weather systems to such distant regions as Antarctica (Andreae et al., 1988).

The visible images at 1301 UTC on 25 and 29 August 1988 clearly show the transport of smoke and haze over the Atlantic Ocean at approximately 30 to 35 S latitude. The haze contrasts very well with the stratus and cirrus clouds over the Atlantic Ocean. In some instances, the smoke appears to blur the underlying cirrus and stratus clouds. This serves as an indication of the height of the aerosols. Cloud statistics derived from multispectral VAS data over Amazonia indicate that transmissive cirrus clouds are usually located at 200 to 300 mb

(~10 km) while clouds opaque to infrared radiation are located from 700 to 800 mb (~3 km) (Menzel et al, 1989). Collectively, these cloud heights suggest a lower bound to the height of the aerosol in the midlatitudes of the southern hemisphere. These statistics indicate that the aerosol extends above 3 km and possibly as high as 10 km. At this height, convective activity can transfer the material into the stratosphere and thus act to influence global atmospheric chemistry and weather.

5. CONCLUSIONS

The GOES VAS is very useful for monitoring biomass burning. Comparison with AVHRR data reveals that the reduced spatial resolution of the GOES VAS does not severely hinder its ability to detect subpixel burning. The high temporal resolution of GOES VAS proves to be extremely useful in locating plumes associated with small fires. It also offers the unique opportunity to determine diurnal variability in the detection of biomass burning and the transport of related aerosols. Results indicate that the optimum time to monitor biomass burning is around 1530 UTC (1230 local time) while the fires are still burning. Burned area estimates determined from satellite measurements three to six hours later are a factor of two to 20 times less, respectively. The motion and extent of aerosols associated with biomass burning suggest that these materials are capable of being transported to such distant areas as Antarctica and may be located as high as 10 km. At this height, convective activity can transfer the material into the stratosphere and act to influence global atmospheric chemistry and climate.

The GOES VAS has demonstrated the capability to estimate the transport of biomass burning aerosols. However, the technique of Matson and Dozier applied to VAS data to estimate fire area and temperature is currently too cumbersome and

time consuming to be used operationally; a reliable smoke correction must be determined for each fire. However a simplified algorithm which assumes a fire temperature of 450 K shows some promise for routine application. Further work is suggested. With the improved thermal imaging capability anticipated with the next generation GOES, modifications of these procedures in conjunction with data received from other remote sensing instruments offer unique opportunities to investigate the effects of biomass burning on the global habitat.

6. REFERENCES

American Society of Photogrammetry, 1983: Manual of Remote Sensing, 2nd ed., Falls Church, VA: 94-98.

Andreae, M. O., E. V. Browell, M. Garstang, G. L. Gregory, R. C. Harriss, G. F. Hill, D. J. Jacob, M. C. Pereira, G. W. Sachse, A. W. Setzer, P. L. Silva Dias, R. W. Talbot, A. L. Torres, and S. C. Wofsy, 1988: Biomass-burning emissions and associated haze layers over Amazonia. J. Geophysical Res., 93, 1509-1527.

Booth, W., 1989: Monitoring the fate of the forests from space. Science, 243, 1428-1429.

Brooke, J., 1989: Rain, fines slow Amazon burning. Wisconsin State Journal, 17 September, pp. 1A, 8A.

Browell, E. V., G. L. Gregory, and R. C. Harriss, 1988: Tropospheric ozone and aerosol distributions across the Amazon Basin. J. Geophysical Res., 93, 1431-1451.

Crutzen, P. J., A. C. Delany, J. Greenberg, P. Haagensen, L. Heidt, R. Lueb, W. Pollock, W. Seilor, A. Wartburg, and P. Zimmerman, 1985: Tropospheric chemical composition measurements in Brazil during the dry season. J. of Atmos. Chemistry, 2, 233-256.

Delany, A. C., P. J. Crutzen, P. Haagensen, S. Walters, and A. F. Wartburg, 1985: Photochemically produced ozone in the emission from large-scale tropical vegetation fires. J. Geophysical Res., 90, 2425-2429.

Dozier, J., 1981: A method for satellite identification of surface temperature fields of subpixel resolution. Remote Sens. of Envir., 11, 221-229.

Fearnside, P. M., 1982: Deforestation in the Brazilian Amazon: how fast is it occurring? Interciencia, 7, 82-88.

Fishman, J., P. Minnis, and H. G. Reichle Jr., 1986: Use of satellite data to study tropospheric ozone in the tropics. J. Geophysical Res., 91, 14451-14465.

Greenberg, J. P., P. R. Zimmerman, L. Heidt, and W. Pollock, 1984: Hydrocarbon and carbon monoxide emissions from biomass burning in Brazil. J. Geophysical Res., 89, 1350-1354.

Henderson-Sellers, A., and V. Gornitz, 1984: Possible climatic impacts of land cover transformations, with particular emphasis on tropical deforestation. Climatic Change, 6, 231-257.

Justice, C. O., J. R. G. Townshend, B. N. Holben, and C. J. Tucker, 1985: Analysis of the phenology of global vegetation using meteorological satellite data. Int. J. of Remote Sensing, 6, 1271-1318.

Malingreau, J. P., G. Stephens, and L. Fellows, 1985: Remote sensing of forest fires: Kalimantan and North Borneo in 1982-83. Ambio, 14, 314-321.

Malingreau, J. P., and C. J. Tucker, 1988: Large-scale deforestation in the southeastern Amazon Basin of Brazil. Ambio, 17, 49-55.

Matson, M., and J. Dozier, 1981: Identification of subresolution high temperature sources using a thermal IR sensor. Photogrammetric Engineering and Remote Sensing, 47, 1311-1318.

Matson, M., and B. Holben, 1987: Satellite detection of tropical burning in Brazil. Int. J. of Remote Sensing, 8, 509-546.

Matson, M., S. R. Schneider, B. Aldridge, and B. Satchwell, 1984: Fire detection using the NOAA-series satellites. NOAA Technical Report NESDIS 7, Washington, DC: Department of Commerce, 34 pp.

Matson, M., G. Stephens and J. Robinson, 1987: Fire detection using data from the NOAA-N satellites. Int. J. of Remote Sensing, 8, 961-970.

Menzel, W. P., 1980: Prelaunch study report of VAS-D performance. Report to NASA under contract NAS5-21965 from Space Science and Engineering Center, University of Wisconsin, Madison, Wisconsin, 65 pp.

Menzel, W. P., W. L. Smith, G. S. Wade, L. D. Herman, and C. M. Hayden, 1983: Atmospheric soundings from a geostationary satellite. Appl. Optics, Vol 22, 2686-2689.

Menzel, W. P., T. J. Schmit, and D. P. Wylie, 1989: Cloud characteristics over Central Amazonia during GTE/ABLE 2B Derived from multispectral VAS observations. Submitted to J. of Geophysical Research.

Nelson, R., and B. N. Holben, 1986: Identifying deforestation in Brazil using multi-resolution satellite data. Int. J. of Remote Sensing, 7, 429.

Nelson, R., N. Horning, and T. A. Stone, 1987: Determining the rate of forest conversion in Mato Grosso, Brazil, using Landsat MSS and AVHRR data. Int. J. of Remote Sensing, 8, 1767-1784.

Newell, R. E., 1971: The Amazon forest and atmospheric general circulation. In Man's Impact On Climate. W. J. Matthew, W. H. Kellogg, and C. D. Robinson (Ed.). Cambridge, MA, MIT Press, 594 pp.

Prins, E. M., 1989: Geostationary Satellite Detection of Biomass Burning in South America. M.S. Thesis. University of Wisconsin, Madison. 141 pp.

Sachse, G. W., R. C. Harriss, J. Fishman, G. F. Hill, and D. R. Cahoon, 1988: Carbon monoxide over the Amazon Basin during the 1985 dry season. J. Geophysical Res., 93, 1422-1430.

Sauck, B., 1988: Personal communication. Madison, Wisconsin.

Setzer, A., 1988: Personal communication. Madison, Wisconsin.

Setzer, A.W., M.C.P. Perevia, A.C.P. Perevia, and S.O. Almeida, 1988: Relatoria de atividades do projeto IBDF-INPE "SEQE" -ANO 1987, INPE publication INPE-4534-RPE/565.

Setzer, A.W. and M.C. Pereira, 1989: Amazon biomass burning in 1987 and their tropospheric emissions, accepted for publication by Ambio.

Simmons, M., 1988: Man-made Amazon fires tied to global warming. The New York Times, 12 August, pp 1, 4.

Smith, W. L., P. K. Rao, R. Koffler, and W. R. Curtis, 1970: The determination of sea surface temperature from satellite high-resolution infrared window radiation measurements. Mon. Wea. Rev., 98, 604-611.

Tardin, A. T., D. C. L. Lee, R. J. R. Santos, O. R. de Assis, M. P. dos Santos Barbosa, M. de Lourdes Moreira, M. T. Pereira, D. Silva, and C. P. dos Santos Filho, 1980: Subprojeto desmatamento, convenio IBDF/CNPq-INPE 1979. Instituto Nacional de Pesquisas Espaciais (INPE) Relatorio No. INPE-1649-RPE/103. Sao Jose dos Campos, Sao Paulo, INPE, 44 pp.

Townshend, J. R. G., C. O. Justice, and V. Kalb, 1987: Characterization and classification of South American land cover types using satellite data. Int. J. of Remote Sensing, 8, 1189-1207.

Tucker, C. J., B. N. Holben, and T. E. Goff, 1984: Intensive forest clearing in Rondonia, Brazil, as detected by satellite remote sensing. Remote Sensing of Environment, 15, 255-261.

Tucker, C. J., I. Y. Fung, C. D. Keeling, and R. H. Gammon, 1986: Relationship between atmospheric CO_2 variations and a satellite-derived vegetation index. Nature, 319, 195-199.

Tucker, C. J., J. R. G. Townshend, T. E. Goff, and B. N. Holben, 1986: Continental and global scale remote sensing of land cover. In Changing Carbon Cycle, A Global Analysis, J. R. Trabalka and D. E. Reichle (Ed.). New York: Springer-Verlag.

Woodwell, G. M., R. A. Houghton, T. A. Stone, and A. B. Park, 1986: Changes in the areas of forests in Rondonia, Amazon Basin, measured by satellite imagery. In Changing Carbon Cycle, A Global Analysis, J. R. Trabalka and D. E. Reichle (Ed.). New York: Springer-Verlag.

Figure Captions

Figure 1. GOES VAS brightness temperatures at 3.9 and 11.2 microns plotted for one scan line over the cerrado region of South America (22 S) for 24 August 1988.

Figure 2. (a) AVHRR 1 km infrared image observed at 3.7 microns at 1942 UTC on 24 August 1988. The black pixels indicate the hot spots. (b) VAS 7 km infrared image observed at 3.9 microns at 1830 UTC for 24 August 1988.

Figure 3. (a) Fire area for a typical fire as a function of smoke correction. (b) Fire temperature as a function of smoke correction.

Figure 4. Regions in South America that were analyzed for the burned area estimate calculations for 14, 15, 16 August 1983 and 24 August 1988.

Figure 5. Representation of diurnal variability in GOES VAS biomass burning detection for 14, 15, 16 August 1983. Field of view (fov) identification number is listed along the y axis and the times at which a fire is detected in each fov is depicted along the x axis.

Figure 6. GOES visible image of South America for 1801 UTC on 24 August 1988 centered on latitude 17 S and longitude 55 W. Note the biomass burning in the selva extending from 50 to 70 W. Additional biomass burning is evident in the cerrado. Plumes emanating from the Andes represent natural forest fires.

Figure 7. (a) Haze at 1301 UTC 25 August 1988 on the morning after the extensive burning. The smoke over the Atlantic Ocean is blurring the underlying clouds. Prevailing circulation is inferred from looping satellite images and tracking cloud or smoke tracers. Winds display anti-cyclonic flow east of the Andes. (b) Five days later, the haze still persists in the western portion of the selva at 1301 29 August 1988. The Andes funnel the haze to

the south. A smoke plume is clearly evident over the Atlantic Ocean as it contrasts with adjacent clouds.

TABLE 1

COMPARISON OF VAS AND AVHRR
FOR SELECTED FIRES IN 1988

FIRE			AVHRR	Burning Area (km2)	VAS	Burning Area (km2)
	LAT	LON	Saturated Pixels	Pixels with Tt>400K	Tt vary	Tt=450
A	-110149	605433	7	.30	1.27	1.94
B	-113852	631514	6	.19	.89	1.56
C	-102010	602020	11	.27	.69	1.78
D	-101003	625246	2	.51	.44	2.32
E	-110051	621328	7	1.02	.94	2.33

AVHRR estimate from pixels with Tt > 400K uses the technique of Matson and Dozier on all hot pixels within the VAS fov and sums the area of those with fire temperatures greater than 400K

The first VAS estimate is calculated using the technique of Matson and Dozier

The second VAS estimate is calculated from the simplified algorithm which assumes a fire temperature of 450 K

TABLE 2

Fire Temperature and Burned Area Statistics

Date	Time	Region	# of Fires Processed/ Detected	Mean Fire Temp (K)	Total Area Burned (# of pixels)	Total Area Burned[+] (km^2)
8/14/83	1231	Selva	121/121	424	1.15	244.2/108.3
	1531	Selva	262/265	464	2.60	552.0/628.4
	1831	Selva	218/234	486	1.41	299.3/481.9
	2131	Selva	31/36	468	.15	31.8/46.7
8/15/83	1801	Selva	254/264	465	2.45	520.2/431.0
8/16/83	1831	Selva	172/241	470	1.35	286.6/405.5
8/24/88	1831	Selva	250/266	469	1.79	361.7/400.1
	1831	Cerrado	166/267	515	1.03	227.0/506.8

[+] the second estimate is calculated from the simplified algorithm which assumes a fire temperature of 450 K

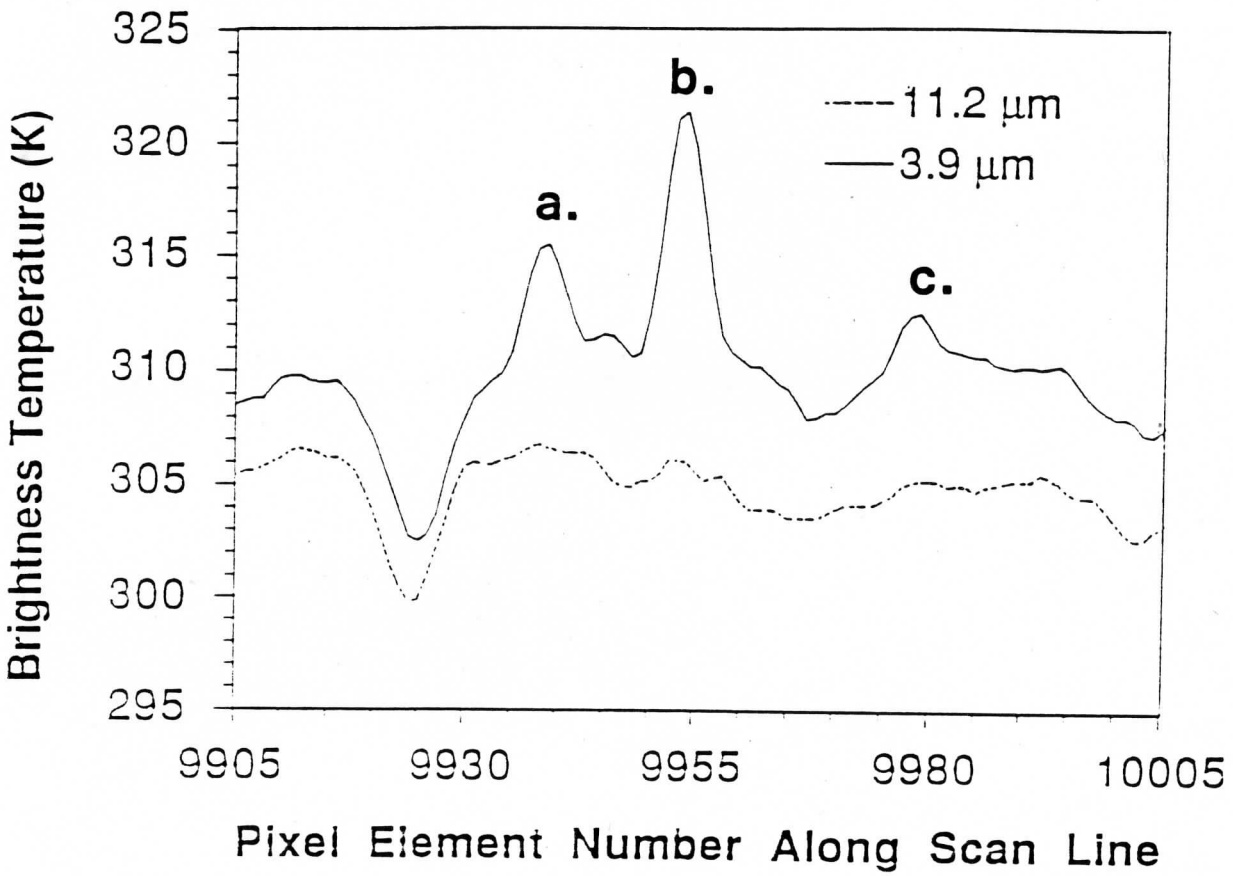

Figure 1. GOES VAS brightness temperatures at 3.9 and 11.2 microns plotted for one scan line over the cerrado region of South America (22 S) for 24 August 1988.

Figure 2a. AVHRR 1 km infrared image observed at 3.7 microns at 1942 UTC on 24 August 1988. The black pixels indicate the hot spots.

Figure 2b. VAS 7 km infrared image observed at 3.9 microns at 1830 UTC for 24 August 1988.

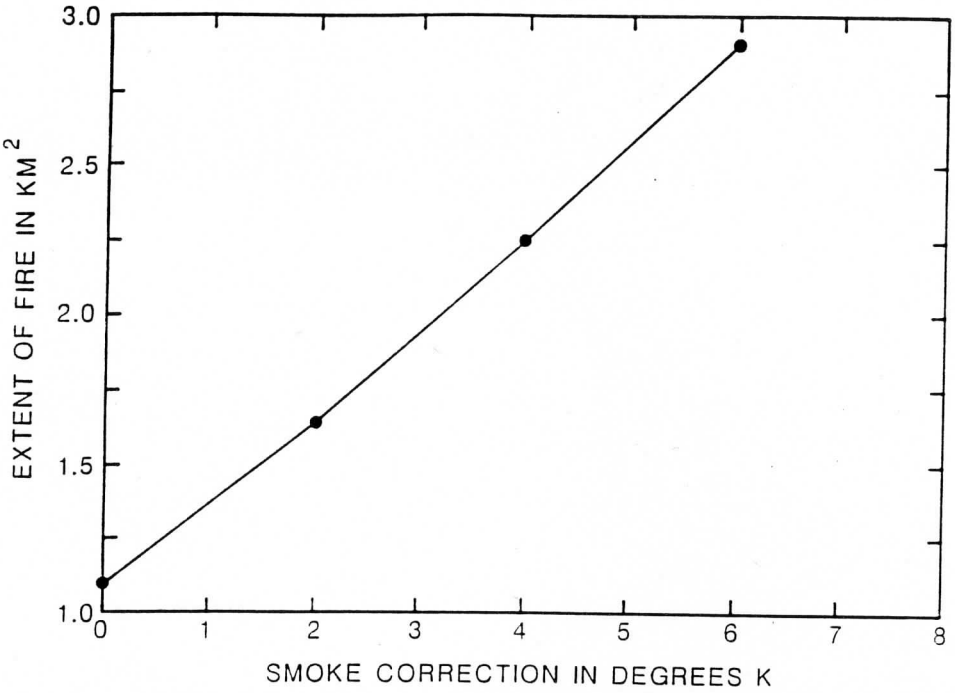

Figure 3a. Fire area for a typical fire as a function of smoke correction.

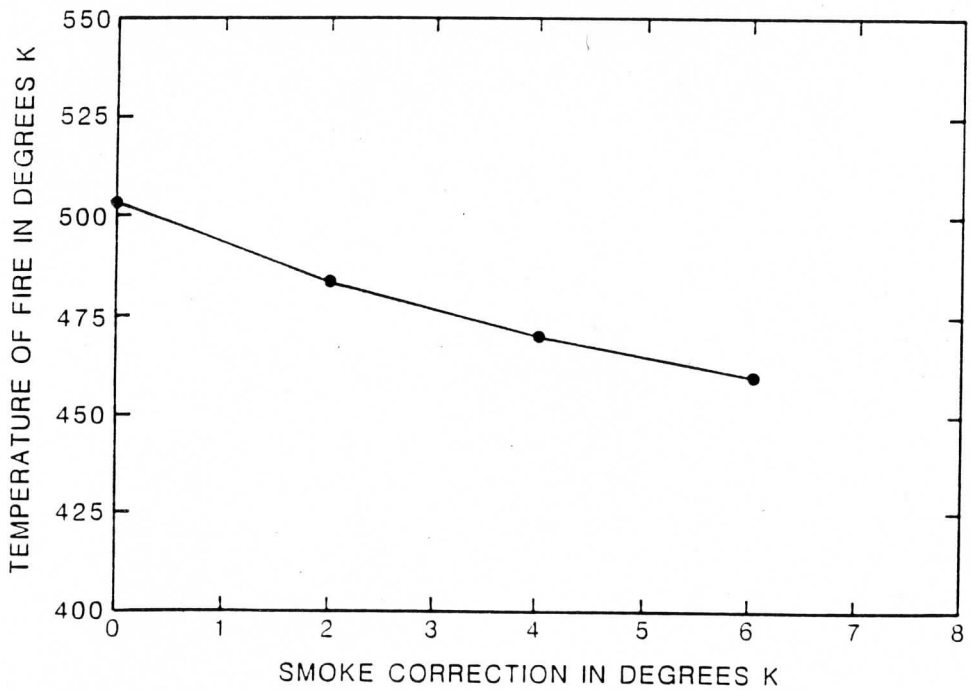

Figure 3b. Fire temperature as a function of smoke correction.

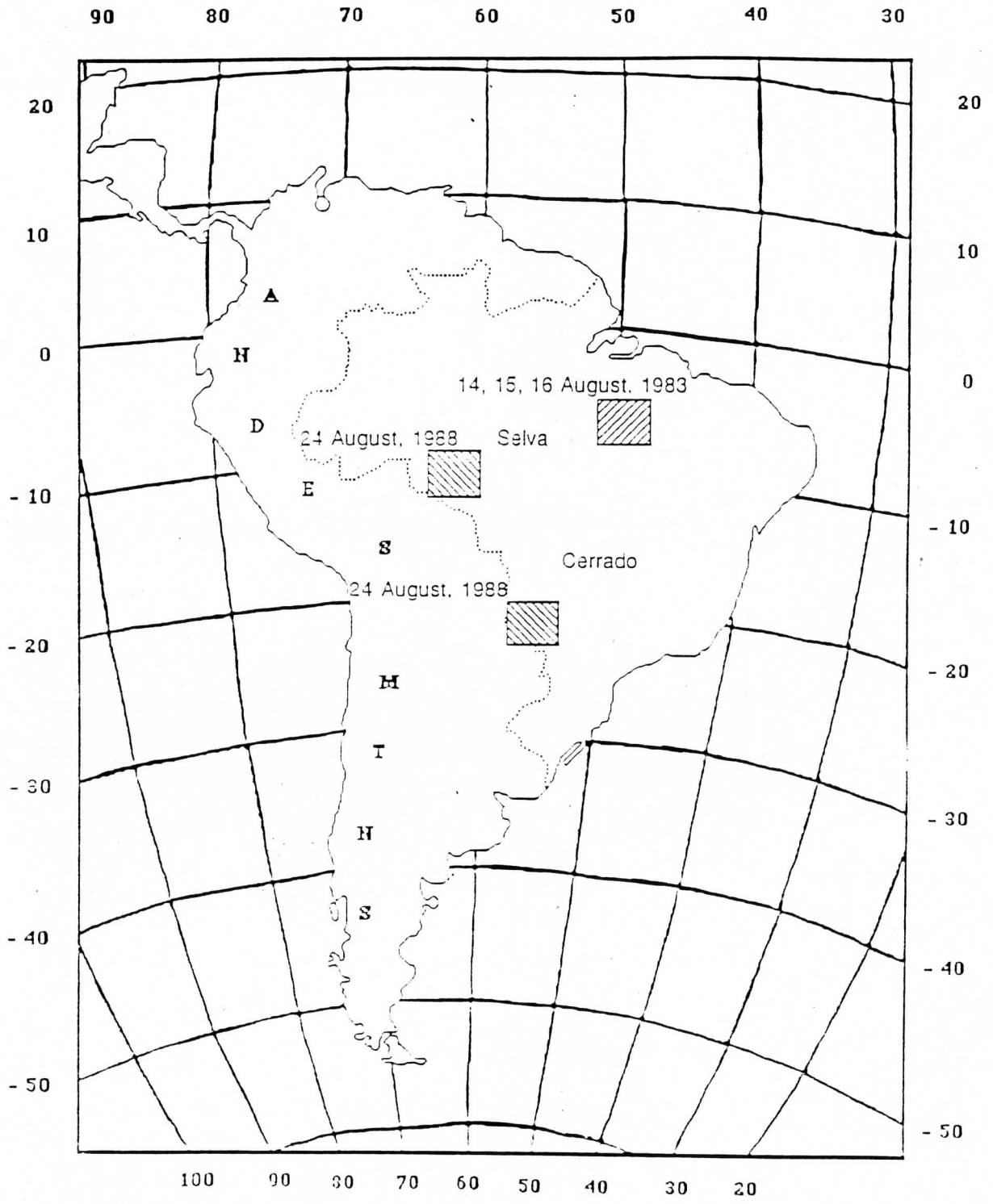

Figure 4. Regions in South America that were analyzed for the burned area estimate calculations for 14, 15, 16 August 1983 and 24 August 1988.

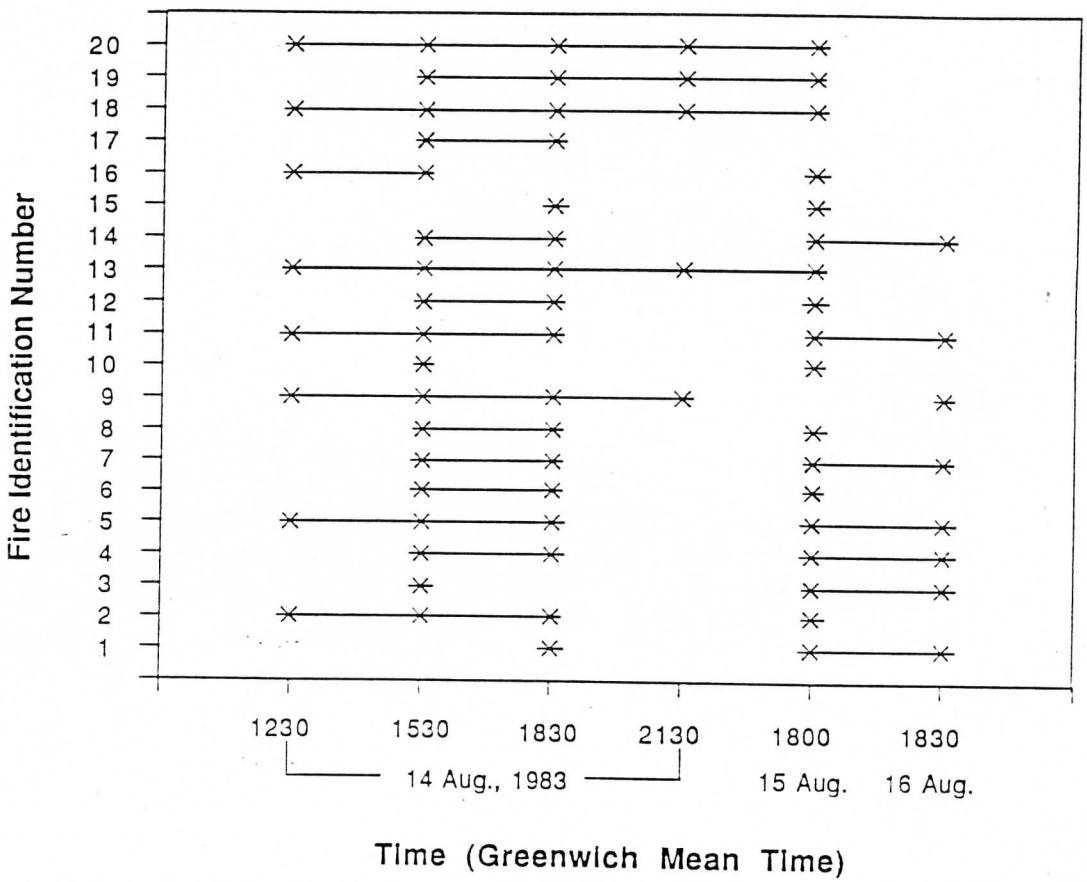

Figure 5. Representation of diurnal variability in GOES VAS biomass burning detection for 14, 15, 16 August 1983. Field of view (fov) identification number is listed along the y axis and the times at which a fire is detected in each fov is depicted along the x axis.

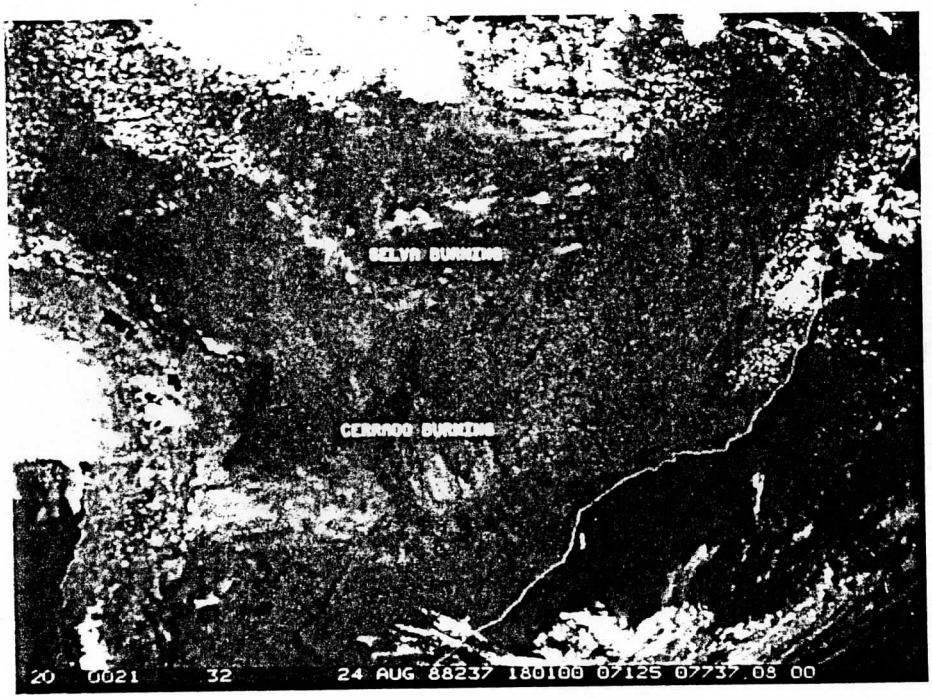

Figure 6. GOES visible image of South America for 1801 UTC on 24 August 1988 centered on latitude 17 S and longitude 55 W. Note the biomass burning in the selva extending from 50 to 70 W. Additional biomass burning is evident in the cerrado. Plumes emanating from the Andes represent natural forest fires.

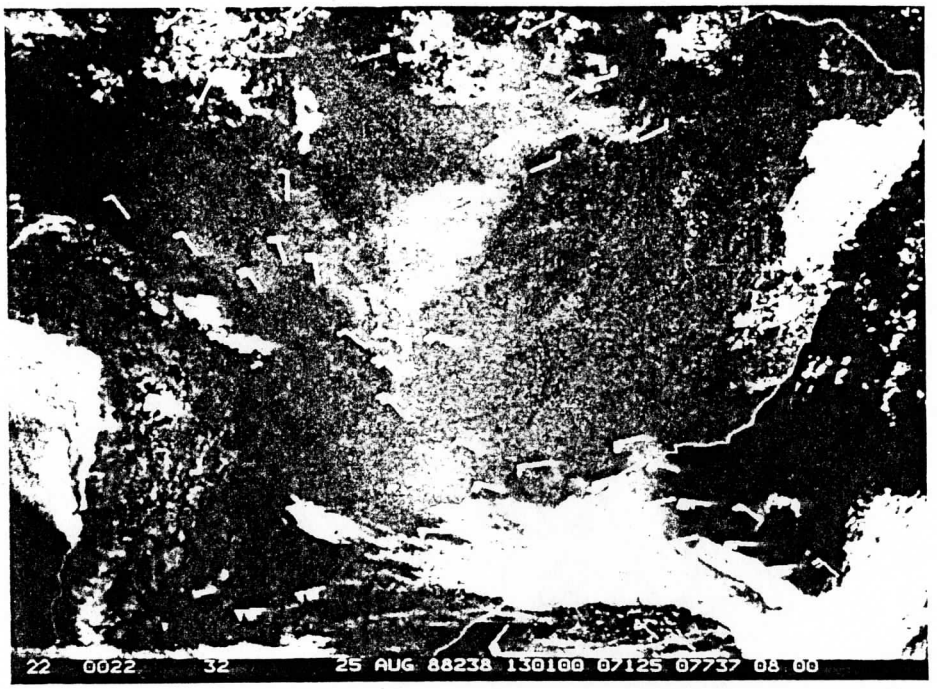

Figure 7a. Haze at 1301 UTC 25 August 1988 on the morning after the extensive burning. The smoke over the Atlantic Ocean is blurring the underlying clouds. Prevailing circulation is inferred from looping satellite images and tracking cloud or smoke tracers. Winds display anti-cyclonic flow east of the Andes.

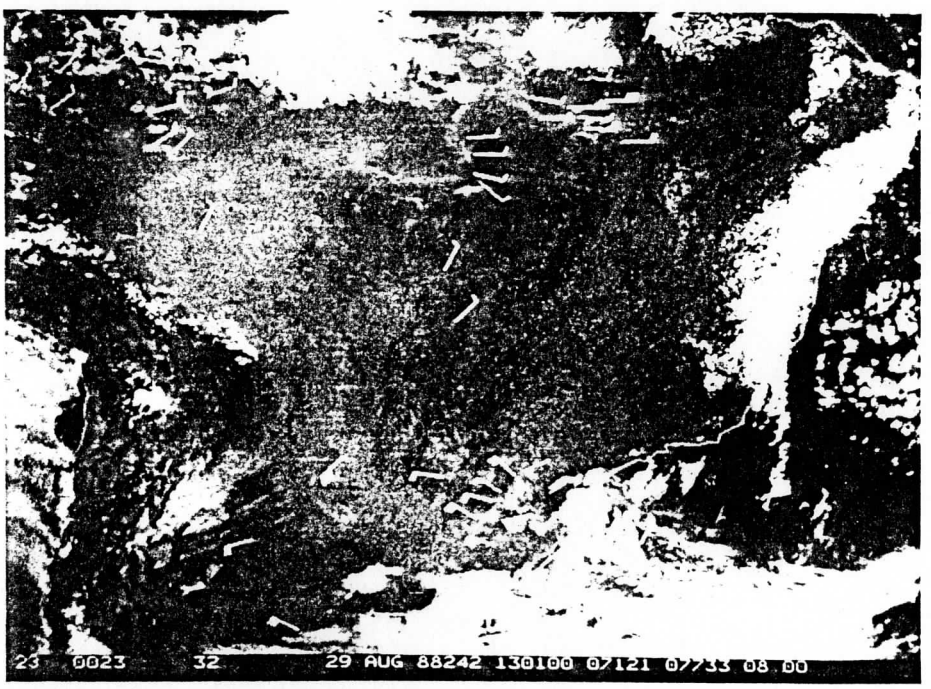

Figure 7b. ~~Five~~ Four days later, the haze still persists in the western portion of the selva at 1301 29 August 1988. The Andes funnel the haze to the south. A smoke plume is clearly evident over the Atlantic Ocean as it contrasts with adjacent clouds.